

Interfacial Charge Transfer Dynamics in Solid-State Hybrid Organic-Inorganic Solar Cells

THÈSE N° 6221 (2014)

PRÉSENTÉE LE 26 JUIN 2014

À LA FACULTÉ DES SCIENCES DE BASE
LABORATOIRE DE PHOTONIQUE ET INTERFACES
PROGRAMME DOCTORAL EN PHOTONIQUE

ÉCOLE POLYTECHNIQUE FÉDÉRALE DE LAUSANNE

POUR L'OBTENTION DU GRADE DE DOCTEUR ÈS SCIENCES

PAR

Arianna MARCHIORO

acceptée sur proposition du jury:

Prof. O. Martin, président du jury
Prof. J.-E. Moser, Prof. M. Graetzel, directeurs de thèse
Prof. M. Chergui, rapporteur
Prof. J. Durrant, rapporteur
Prof. A. Hagfeldt, rapporteur



ÉCOLE POLYTECHNIQUE
FÉDÉRALE DE LAUSANNE

Suisse
2014

Abstract

Our generation must face the scarcity of natural resources and the threat of climate change. A drastic turn should be made in our models of energy production and consumption. Photovoltaic power generation can be one of the ways to solve these issues; thus, the development of inexpensive and efficient solar cells is a key objective of photovoltaic research. At the heart of this thesis is the understanding of the mechanisms governing the operation of solid-state hybrid organic-inorganic solar cells. These cells, built using a mesoporous TiO_2 electron-extracting layer, covered with a light absorber such as a dye or an organic-inorganic perovskite semiconductor, and impregnated with an organic hole transport material, are based on the principle of separation of light absorption and charge transport. The whole system works due to the kinetic competition between the various processes of charge separation and charge recombination. The knowledge on the timescales of these processes is then of fundamental importance and accessible by time-resolved spectroscopic techniques such as transient absorption spectroscopy.

In the first chapter, some fundamental aspects of photochemistry are presented, together with a review of the main working principles of dye-sensitized solar cells and perovskite-based cells. Chapter 2 describes the experimental optical techniques used to study these systems. The main achievements of this thesis are presented in Chapter 3 to 6. Chapter 3 introduces the concept of hole injection in solid-state dye-sensitized solar cells (ssDSCs) and reports the multiexponential dynamics spanning from the picosecond to the nanosecond for the regeneration of the oxidized dye by the hole transport material (HTM) *spiro*-MeOTAD. We show that accurate information is obtained by probing the oxidized state of the dye in the near-infrared, as this gives direct information on the fraction of dye regenerated by the HTM. The effect of the pore filling fraction of HTM on the dye regeneration is also discussed. Chapter 4 deals with post-treatment of mesoporous TiO_2 films using TiCl_4 solutions, which is commonly applied during the fabrication of ssDSCs to improve their performance. The effect of this post-treatment upon the charge carrier dynamics is scrutinized; kinetic studies show that hole injection in *spiro*-MeOTAD and charge recombination are markedly slower in TiCl_4 -treated films. These findings are rationalized by a model describing the interaction at the interface between TiO_2 , the dye

and *spiro*-MeOTAD, which emphasizes the importance of controlling the contact between the HTM and the sensitized semiconducting oxide network.

Chapter 5 presents the photophysics of a new and very promising light absorber, the perovskite $\text{CH}_3\text{NH}_3\text{PbI}_3$. The main spectroscopic signatures of this material deposited on a mesoporous framework of Al_2O_3 , as obtained by transient absorption spectroscopy, are introduced and analysed. The photophysical processes are uncovered, enabling the study of interfacial processes in Chapter 6, where perovskite is interfaced either with an electron extraction layer such as TiO_2 , or deposited on an inert scaffold to resolve the electron injection step. Hole injection dynamics are also monitored by interfacing the perovskite material with the hole extracting layer *spiro*-MeOTAD. By using a combination of techniques, including femtosecond and nanosecond transient absorption, terahertz spectroscopy and time-resolved photoconductance measurements, both processes are revealed. We provide a timescale as well as a mechanistic pathway for all reactions in the system.

KEYWORDS: solid-state dye-sensitized solar cell, TiO_2 , Al_2O_3 , perovskite, $\text{CH}_3\text{NH}_3\text{PbI}_3$, hole transport material, *spiro*-MeOTAD, charge transfer, femtosecond transient absorption, nanosecond transient absorption

Résumé

Notre génération doit faire face à l'épuisement des réserves naturelles ainsi qu'à la menace du changement climatique. La conversion quantique de l'énergie solaire se présente comme l'une des solutions possibles à ces problèmes, et de ce fait, le développement de cellules solaires peu coûteuses et efficaces est l'un des objectifs majeurs de la recherche photovoltaïque. Cette thèse a pour but la compréhension des mécanismes qui régissent le fonctionnement des cellules solaires solides, de type hybride organique-inorganique. Ces cellules sont basées sur un réseau de TiO_2 mésoporeux servant de couche transportant les électrons. L'oxyde nanocristallin est recouvert par un absorbeur de lumière, tel que un colorant sensibilisateur ou un semi-conducteur hybride organique-inorganique comme la perovskite $\text{CH}_3\text{NH}_3\text{PbI}_3$, et imprégné avec un transporteur de trou organique. Le principe fondamental consiste en la séparation des processus d'absorption de la lumière et de transport de charges. Le fonctionnement du système est basé sur la compétition cinétique entre les réactions de séparation de charge et de recombinaison, ce qui rend nécessaire la connaissance des échelles de temps pour ces processus. Cette information est accessible à travers des études spectroscopiques résolues en temps impliquant des techniques telles que l'absorption transitoire.

Dans le premier chapitre, certains aspects fondamentaux de la photochimie sont présentés, ainsi qu'une revue des spécificités des cellules solaires à colorant sensibilisateur et des cellules basées sur les perovskites. Le chapitre 2 décrit les techniques expérimentales utilisées pour étudier ces systèmes. Les résultats majeurs de cette thèse sont présentés dans les chapitres 3 à 6.

Le chapitre 3 introduit le concept d'injection de trou dans les cellules solaires solides à colorant sensibilisateur (ssDSCs) et rapporte une dynamique multiexponentielle, allant de la picoseconde à la nanoseconde, pour la régénération de l'état oxydé du colorant par le transporteur de trou organique (HTM) *spiro*-MeOTAD. Il est montré qu'une information précise est obtenue en sondant l'état oxydé du colorant dans le proche infrarouge; celui-ci donnant un accès direct à la fraction de colorant régénérée par le transporteur de trou. L'effet de la fraction de remplissage du TiO_2 mésoporeux par le HTM sur la régénération du colorant est discuté. Le chapitre 4 considère le post-traitement du film de TiO_2 par des solutions de TiCl_4 . Ce post-traitement est communément appliqué dans les ssDSCs pour augmenter leurs performances. L'effet de ce traitement sur la dynamique des charges dans

les ssDSCs est examiné; les études cinétiques montrent que l'injection du trou dans le HTM, ainsi que la recombinaison, sont retardées lors de ce traitement. Les résultats sont expliqués dans le cadre d'un modèle décrivant les interactions entre le TiO₂, le colorant et le *spiro*-MeOTAD, et qui souligne l'importance de contrôler le contact entre le HTM et le réseau d'oxyde semi-conducteur sensibilisé.

Le chapitre 5 présente la photophysique d'un nouvel absorbeur de lumière très prometteur, la perovskite CH₃NH₃PbI₃. Les caractéristiques spectroscopiques de ce matériau déposé sur une matrice mésoporeuse inerte d'Al₂O₃, obtenues par absorption transitoire, sont introduites et analysées. Les processus photophysiques sont mis en évidence, permettant ainsi l'étude des processus aux interfaces dans le chapitre 6, où la perovskite est mise en contact soit avec une couche extractrice d'électrons comme le TiO₂, soit déposé sur une matrice inerte afin de résoudre l'étape d'injection d'électron. L'injection de trou est également analysée en mettant la perovskite en contact avec une couche extractrice de trous composée de *spiro*-MeOTAD. En utilisant une combinaison de techniques expérimentales, dont l'absorption transitoire femtoseconde et nanoseconde, la spectroscopie terahertz et des mesures de photoconductance résolue en temps, ces deux processus sont mis en évidence. Une échelle de temps ainsi qu'un mécanisme sont proposés pour toutes les réactions ayant lieu dans le système.

MOTS-CLÉS: cellule solaire solide à colorant sensibilisateur, TiO₂, Al₂O₃, CH₃NH₃PbI₃, perovskite, transporteur de trou, *spiro*-MeOTAD, transfert de charge, absorption transitoire femtoseconde, absorption transitoire nanoseconde.

Table of contents

CHAPTER 1 Introduction	9
1.1 Light absorption and charge transfer	10
1.1.1 Light and matter.....	10
1.1.2 Absorption, emission and scattering	12
1.1.3 Potential energy diagrams.....	13
1.1.4 Transitions and Jablonski diagrams	14
1.1.5 Non-radiative transitions	17
1.1.6 Light absorption in semiconductors	18
1.2 Dye-sensitized solar cell	23
1.2.1 TiO ₂	25
1.2.2 Dye	26
1.2.3 Liquid redox mediators	27
1.2.4 The solid-state solar cell.....	28
1.3 Dynamics of charge transfer processes	29
1.4 Perovskite-based solar cells.....	33
1.4.1 Perovskites: structure and properties	33
1.4.2 Perovskite in photovoltaic devices.....	35
1.4.3 Perovskite, what is your function?	36
1.5 References	39
CHAPTER 2 Experimental part	47
2.1 Flash Photolysis.....	48
2.1.1 Fundamentals of the technique.....	48
2.1.2 Excitation source.....	49
2.1.3 Detection	50
2.2 Femtosecond transient absorption spectroscopy	51
2.2.1 Fundamentals of the technique.....	51
2.2.2 Laser	51
2.2.3 NOPA.....	52
2.2.4 Pulse compression.....	53
2.2.5 Probe schemes.....	54
2.2.6 Monochromatic Pump-probe.....	55
2.2.7 White-light continuum (WLC) probe	56
2.3 Samples preparation	62
2.4 References	63

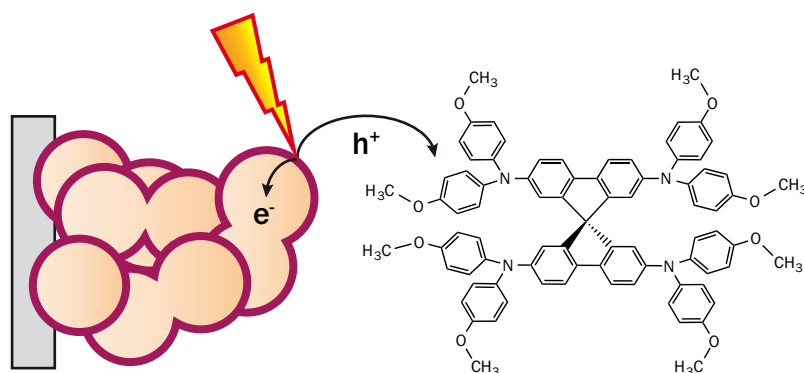
CHAPTER 3 Hole injection in solid-state DSCs	65
3.1 Introduction	66
3.1.1 Hole mobility.....	68
3.1.2 Pore wetting and filling	71
3.1.3 Interface engineering.....	74
3.2 Methods.....	74
3.2.1 Samples preparation	74
3.2.2 Femtosecond transient absorption.....	75
3.3 Monitoring of the hole transfer reaction	76
3.3.1 Dynamics of hole injection in the visible	77
3.3.2 Dynamics of hole injection in the near IR.....	79
3.4 Investigation of the effect of pore filling fraction	81
3.5 Conclusion	83
3.6 References	83
CHAPTER 4 Effect of TiCl₄ post-treatment in ssDSCs	89
4.1 Introduction	90
4.2 Methods.....	92
4.2.1 Samples preparation	92
4.2.2 Nanosecond flash photolysis	93
4.2.3 Femtosecond transient absorption.....	93
4.2.4 Femtosecond transient absorption data treatment	94
4.3 Results	100
4.3.1 Absorption spectra.....	100
4.3.2 SEM pictures	102
4.3.3 Electron injection dynamics	103
4.3.4 Hole injection dynamics.....	104
4.3.5 Hole injection in TiCl ₄ -treated samples	106
4.3.6 Hole injection with different TiCl ₄ treatments	107
4.3.7 Charge recombination	107
4.4 Discussion	108
4.5 Conclusion	111
4.6 References	111
CHAPTER 5 Photophysical processes in CH₃NH₃PbI₃	115
5.1 Introduction	116
5.2 Methods.....	117
5.2.1 Samples preparation	117

5.2.2	Femtosecond transient absorption.....	119
5.3	Results.....	120
5.3.1	Overview of spectral signatures in $\text{CH}_3\text{NH}_3\text{PbI}_3$	120
5.3.2	Fluence effects.....	124
5.3.3	Global analysis.....	124
5.4	Band model for $\text{CH}_3\text{NH}_3\text{PbI}_3$	128
5.5	Conclusion.....	135
5.6	References.....	136
CHAPTER 6 Photoinduced processes at the heterojunction of $\text{CH}_3\text{NH}_3\text{PbI}_3$.....		139
6.1	Introduction.....	140
6.2	Methods.....	142
6.2.1	Samples preparation.....	142
6.2.2	Spectroscopic characterization.....	144
6.3	Hole injection into <i>spiro</i> -MeOTAD.....	147
6.3.1	Femtosecond transient absorption.....	147
6.3.2	THz spectroscopy.....	150
6.4	Electron injection into TiO_2	151
6.4.1	Ultrafast transient optical absorption spectroscopy.....	151
6.4.2	Time-resolved microwave photoconductance measurements.....	154
6.4.3	Nanosecond transient optical absorption spectroscopy.....	155
6.5	Discussion.....	156
6.6	Conclusion.....	160
6.7	References.....	162
CHAPTER 7 Conclusions and outlook.....		163

CHAPTER 1

Introduction

In the first part of this chapter, a brief overview of photochemistry is presented, including some fundamental aspects of the interaction of light and matter both in molecular systems and in semiconductors. Then, the two systems studied throughout this thesis, both the solid-state dye-sensitized solar cell and the perovskite-based cell, will be described together with a review of the literature to constitute the state-of-the-art in this field.



1.1 Light absorption and charge transfer

The quest for renewable energies is one of the most urging challenges of the 21st century. The International Agency for Energy reported a global power consumption of 17 TW in 2011, and this value is expected to increase to 30 TW by 2040 with a population of 9 billions individuals.¹

Sunlight can be considered as a infinite source of energy: one hour of sunlight on Earth would be sufficient to supply enough energy for an entire year, and indeed a surface of land covered with 850 000 km² of photovoltaic panels working at 10% efficiency and with a capacity factor of 20% would meet all the present world's energy demand.²

The sun is a fantastic source of energy, and not only for photovoltaic applications. Light-driven processes are omnipresent in our everyday life: from the mechanism of vision to the synthesis of vitamin D, not forgetting the indispensable photosynthesis in which glucose is created from CO₂ and water. All of these arise from the interaction of light and matter, which we are going to explore in more detail.

1.1.1 Light and matter

Visible light belongs to the spectrum of electromagnetic radiation, together with low-energy IR light, microwaves, radio waves, and high-energy X-rays and gamma rays for example. Electromagnetic radiation is represented as the combination of an oscillating electric field and of an oscillating magnetic field, which are perpendicular between each other and perpendicular to the direction of propagation. This is the so-called classical wave picture of light, but in certain cases it can be convenient to describe it as a stream of particles, referred to as photons. When the electromagnetic wave interacts with a charged particle, its electric field induces an oscillation of this charge. Conversely, an oscillating charge radiates, in all directions except in the axis of the oscillation. The fact that static charges do not radiate is an important property that should be kept in mind.

Matter, on the other side, is constituted of atoms that contain charged particles such as negative electrons orbiting around positively charged nuclei. The position of the electrons around the nuclei cannot be described by classical mechanics laws, and must be accounted for by quantum mechanics. In this picture, the electron positions can be described by the distribution of their probability to be found at a certain position around the nucleus, which is mathematically described by a wavefunction φ . The spatial symmetry of their

probability of distribution is an atomic orbital. The simplest orbital is the s orbital with spherical shape, then the p orbital that has one symmetry axis and then more complex orbitals such as d, f , etc.

Molecules are formed by the combination of these orbitals in order to share their electrons between different atoms and to create a stable closed shell configuration. These shared orbitals are called molecular orbitals (MOs). Indeed, two hydrogen atoms will share their unique electron in order to “see” two electrons. The molecular orbitals created from two s atomic orbitals are then of two types: a first σ orbital where the electrons are shared between the two nuclei and screen the two repulsing nuclei (bonding). The second orbital is called σ^* and is a higher energy configuration. Here, the electrons are distributed at the opposite and the repulsion between the nuclei is greater (antibonding). For the π molecular orbitals, originating from p atomic orbitals and which are off-axis, the screening of the nuclei is less effective, thus the π and π^* orbitals are respectively more energetic and less energetic than the σ and σ^* orbitals. The n orbitals correspond to the lonely pairs, which are non-bonding electron pairs. When light is exciting a molecule, a transition between these orbitals can happen that changes the electronic configuration of the molecule. More specifically, *visible* light absorption deals with *electronic* transitions, where an electron is promoted from a low-energy orbital to higher energy orbitals. When the electron is promoted from one orbital to another, its distance \mathbf{r} from the nucleus changes, and an instantaneous dipole moment $\mathbf{u} = q \cdot \mathbf{r}$ is created.

The MOs can be found as singlet states (where the spins, i. e. the rotational precession of the electrons on themselves are opposite and 180° out-of-phase), or triplet states (where the electrons on two degenerate orbitals have the same precession, or opposite in-phase precession). The electronic energy levels are then called S_0, S_1, S_2 etc., and T_1, T_2 , etc. In a molecule, two MOs are of special interest: the highest occupied MO, called HOMO and the lowest unoccupied MO, called LUMO, between which the first transition can take place.

1.1.2 Absorption, emission and scattering

Since energy levels for atoms and molecules are quantized and not continuous, light *absorption* occurs when there is an allowed transition from a discrete energy level to a higher one. For this, the exact amount of energy corresponding to the transition must be provided. The fact that a transition is allowed or forbidden follows certain rules that will be described later in the text. An excited state M^* is formed by the absorption of a photon in the ground state M :



Then the atom or molecule can return this energy radiatively, so that the excited state decay back to the ground state, in the process of *emission*:



Non-radiative deactivation, where the energy is lost as heat and not as light, is also a possible decay pathway. Among the radiative pathways, *stimulated emission* (SE) is the other process to consider. In this case, it is a photon that triggers the decay of an excited state, resulting in the emission of two photons:



These reactions can be written in kinetic terms similarly to first- and second-order chemical reactions, with I being a photon concentration:

$$\text{Absorption} \quad \frac{d[M^*]}{dt} = B_{12}I[M] \quad (1.4)$$

$$\text{Emission} \quad \frac{d[M^*]}{dt} = -A_{21}[M^*] \quad (1.5)$$

where B_{12} and A_{21} represent the Einstein coefficients respectively for absorption and for emission. The Einstein coefficients give the probability for each type of transition.

For the case of stimulated emission, the change of concentration of an excited state with time is then proportional to the concentration of photons and of excited states, multiplied by the Einstein coefficient for SE, B_{21} :

$$\text{Stimulated Emission} \quad \frac{d[M^*]}{dt} = -B_{21}I[M^*] \quad (1.6)$$

In the case when the impinging light does not have the required amount of energy for the transition, *elastic scattering* occurs; the electromagnetic radiation provokes an oscillation of the matter's charges, and their oscillation will immediately return a photon of the same frequency.

1.1.3 Potential energy diagrams

Molecules can be modelled as oscillators where the atoms are connected through springs. Like in the classical oscillator case, potential energy is a function of the distance that makes the atoms come closer, and then repel each other. An associative state has an energy minimum that corresponds to the most stable geometry. The most stable associative state is generally the ground state S_0 , the first excited state is then S_1 . Each molecular orbital can be described by a potential curve as a function of the nuclear configuration (i.e. the nuclear coordinate, which is the distance between the nuclei for the simple case of a diatomic molecule), as shown in Figure 1.1.

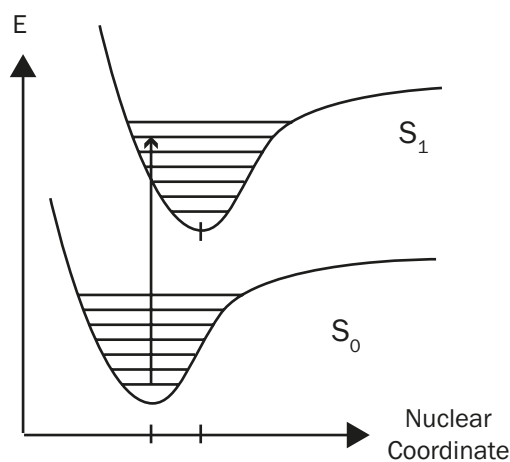


Figure 1.1 Potential energy diagram

The potential curve thus describes an electronic energy level. On top of these electronic levels, there are several sub-levels that correspond to the vibrational energy levels of a molecule (shown on Figure 1.1), and each vibrational energy level, mainly in the gas phase, has closely spaced rotation energy level that nearly form a continuum. Usually at room temperature only the first vibration levels are populated. All of these states can be

characterized by a specific wavefunction that contains a nuclear, electronic, vibrational (and rotational) part:

$$\Phi_{tot} = \Phi_{nuclei} \Phi_{electrons} = \Phi_{nuclei} \Phi_{el} \Phi_{vib} \Phi_{rot} \quad (1.7)$$

In the frame on the Born-Oppenheimer approximation, the nuclear motion can be separated from the electronic motion, as the nuclei are practically immobile in the timescale of motion of the electrons.

1.1.4 Transitions and Jablonski diagrams

Allowed and forbidden transitions are dependent on the overlap of the overall wavefunctions between the initial state φ_i and the final state φ_f , which in the case of light absorption are respectively the ground state and excited state. The overall wavefunction is considered here as the product the electronic, vibrational and rotational wavenfunctions. The oscillatory strength describes to which extent a transition is allowed ($f=1$) or forbidden ($f=0$) and is related to the Einstein coefficients defined in section 1.1.2. The oscillatory strength factorizes several “overlap factors”:

$$f = f_{spin} f_{spatial} f_{sym} f_{vib} \quad (1.8)$$

The spin overlap factor f_{spin} is 1 for a transition with same multiplicity (S-S or T-T), while transitions between different multiplicities are forbidden ($f_{spin}=0$).

The spatial overlap $f_{spatial}$ concerns the spatial overlap of the orbitals; indeed if they are too distant the transition will not take place.

f_{sym} is a symmetry factor, as transition between different types of orbitals (that implies a change in the angular momentum of the electron) will be hindered.

f_{vib} is the vibrational overlap factor, best known as Franck-Condon factor, which is related to the overlap of the vibrational wavefunctions in the ground and excited state.

For a transition to be possible, none of these factors should be zero.

Jablonski diagrams are a schematic view of all the possible transitions that can take place in a molecular system. They also provide the timescales for each of them. Radiative and non-radiative transitions are shown on Figure 1.2 and detailed below.

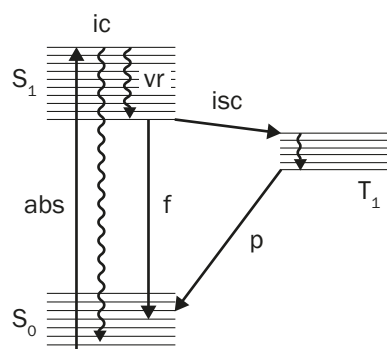


Figure 1.2 Jablonski diagram

A transition between state S_0 and S_1 occurs upon light absorption to a vibrationally excited state of S_1 (abs, 10^{-16} s). Vibrational relaxation (vr, 10^{-12} s) releases the excess energy, and internal conversion (ic, 10^{-9} - 10^{-6} s) can occur between the excited state and the ground state. Fluorescence can take place from the lowest vibrational level (f, 10^{-9} s). Intersystem crossing (isc, 10^{-9} - 10^{-6} s) is a conversion process from a singlet state to a triplet state T_1 . From the triplet state, the possible radiative deactivation pathway is the spin-forbidden transition phosphorescence (p, 10^{-3} - 10^3 s).

Radiative transitions

Absorption

The electronic ground state S_0 is the only available level at room temperature. Populating excited states at higher temperature would usually lead to the destruction of the molecules. Upward transitions are then all radiative transitions that depend on the Einstein coefficient B_{12} . Absorption of light occurs usually very fast, in the order of a few hundreds of attoseconds (10^{-16} s). A very important property of light absorption is stated by the Franck-Condon principle. Within the Born-Oppenheimer approximation, a transition between two distinct electronic states S_0 and S_1 can take place only “vertically”, i.e. at a common nuclear geometry. Thus, there must be an overlap of the vibrational wavefunction in order to obtain an allowed transition. Vibrational decay can then occur in the ps timescale (10^{-12}): The vibrationally excited states are rapidly cooled down by releasing heat to the lowest vibrational level of the electronically excited state.

Fluorescence

Fluorescence is a direct radiative transition between states of same multiplicity. According to the Kasha’s rule, the transition always takes place from the lowest vibrational level of the lowest electronically excited state, to the various vibrational levels of the electronic ground state. There are many known exceptions to the Kasha’s rule. Fluorescence usually operates in the ns (10^{-9}) timescale. Decay to the lowest vibrational level can form an exciton, a tightly bound species formed by an electron and its corresponding hole.

Phosphorescence

Phosphorescence is the spin-forbidden version of the fluorescence, where the radiative transition takes place usually from the triplet excited state to the singlet ground state. This forbidden process thus is much longer than fluorescence and can occur in the ms up to the hours timescale.

Luminescence kinetics

The lifetime of all these radiative processes all depends on the probability for the transition and thus on the Einstein coefficient for spontaneous emission B_{21} . The probability for the transition is the same for molecules of the same species, thus the decrease of the number of excited molecules in time is given by:

$$\frac{d[M^*]}{dt} = -k_r [M^*] \quad (1.9)$$

which integrates to:

$$M^* = M_0^* e^{(-k_r t)} = M_0^* e^{\left(\frac{-t}{\tau_r}\right)} \quad (1.10)$$

This is a first-order reaction where M_0^* is the initial number of excited state molecules, k_r is the rate constant or alternatively one can consider the time constant $\tau_r = 1/k_r$.

Sometimes a more practical quantity can be used: the half time $t_{1/2}$, where half of the population has already decayed. In the case of a monoexponential process, the time constant and the half time are related by the relationship:

$$t_{1/2} = \tau_r \ln(2) \quad (1.11)$$

In practice, it is never possible to obtain the “pure” luminescence lifetime of a molecule as it competes with other non-radiative pathways of decay. These can be internal conversion, intersystem crossing or intermolecular/intramolecular quenching (charge transfer or energy transfer). The quantum yield for fluorescence is given by:

$$\Phi_f = \frac{k_f}{k_f + k_{isc} + k_{ic} + k_q [Q]} \quad (1.12)$$

Where k_f is the rate constant for fluorescence, k_{isc} is the rate constant for inter-system crossing to a triplet state, k_{ic} the rate constant for internal conversion and $k_q[Q]$ the product of the rate constant for the intermolecular/intramolecular quenching and of the concentration of quencher.

1.1.5 Non-radiative transitions

These are non-radiative transitions that dissipate their energy through heat. The controlling factor of the deactivation is the overlap between the wavefunctions of the initial and final state, φ_i and φ_f , just as for radiative transitions. In this case though, the transition is also governed by the separation in energy between the two states. In a more schematic picture, there should be a point of isoenergetic crossing in the two potential energy curves. The general expression of the rate constant k_{NR} of a non-radiative transition is given by the Fermi's golden rule:

$$k_{NR} = \frac{2\pi}{h} |H|^2 \cdot \rho(E_f) \quad (1.13)$$

$|H|$ represents the electronic coupling matrix element between the initial and final states (in other words, the coupling of the electronic wavefunctions at the isoenergetic crossing), and $\rho(E_f)$ is the Frank-Condon weighted density of states. This last term is the density of vibrational levels of the final state, at the energy of the initial state. Since higher vibrational levels are increasingly spread out in energy space, the vibrational levels of the final state are less likely to overlap with the ones of the initial state and the rate constant will first increase to a maximum and then decrease with increasing energy difference between the initial and final state.

Internal conversion and intersystem crossing

Internal conversion refers to a case where the energy dissipation through heat implies two states with the same spin multiplicity. In the case of intersystem crossing though, there is a change in spin multiplicity. The conservation rules imply that only the total angular momentum should be conserved, thus a change in spin multiplicity also requires a change in angular momentum (e.g. a change between a singlet $n\pi^*$ state to a triplet $\pi\pi^*$ state). Intersystem crossing requires a strong spin-orbit coupling able to degenerate spin states.

Quenching of excited states by energy or charge transfer

Quenching occurs when the excess energy of an excited state (M^*) is transferred to an external molecule (Q). This process can be obtained in two ways: either energy or charge transfer.

Energy transfer is possible if the quencher molecule has an excited state lower in energy than M^* . In this case, M^* can transfer its energy via several different mechanisms. One is the electron exchange mechanism (Dexter) where a high-energy electron of M^* is exchanged for a low-energy electron of Q . The other one is called the Förster mechanism, where the excited electrons that decays to a lower orbital in M^* will induce a dipole-dipole interaction in Q , thus moving one electron. The rate of this process is dependent on the inverse cube of the distance, as the dipoles should be closely coupled.

On the other hand, charge transfer is the most important mechanism for photochemistry, as it can lead to new species. An electron or a hole from the excited molecule can be transferred to a neighbouring ground state molecule, provided proper alignment of the energy levels. This incredibly rich field of photochemistry is the one we will be focusing on in this thesis, and in particular because of its implications in solar cells.

1.1.6 Light absorption in semiconductors

A very short description of the solid-state physics and light absorption in semiconductors will be provided, mainly in order to define the framework for the discussion on the perovskite systems presented in Chapters 5 and 6.

Band structure in semiconductors

In semiconductors, by analogy with molecular orbitals, each atomic orbital will add together and because of the splitting, the large number of energy levels will superimpose to form a continuum of energy levels. These dense and broad levels give rise to the lowest unoccupied band, namely the conduction band (CB) and the highest occupied band, namely the valence band (VB), separated by a forbidden region, i.e. the band gap. Photoexcitation with photon energy greater than the energy of the band gap will promote an electron in the CB and leave a hole behind in the VB. At absolute zero temperature, an intrinsic semiconductor will not be able to conduct electricity due to the fact that all of its electrons are involved in bonding, in the valence band. With increasing temperature,

and if the band gap is small enough ($< 3 kT$) the electrons will gain kinetic energy and some of them will be promoted to the conduction band. Electron motion can then occur, either by motion of electrons in the conduction band, or by motion of holes (electron vacancies) in the valence band. Doping of the semiconductor can greatly increase its conduction. In this case, electrons (n-doping) or holes (p-doping) are added in the CB and in the VB respectively through the use of an atom with different number of valence electrons, and the increase in the number of carriers will increase the conductivity in the material. The mathematical treatment of the band structure of a semiconductor is given by the Bloch's equation, in which the wavefunction of an electron free space is multiplied by a periodic function corresponding to the periodicity of the lattice of the semiconductor crystal. Thus the Bloch wavefunction has the form of the product of a plane wave $e^{i\mathbf{k}\cdot\mathbf{r}}$, with \mathbf{k} being the wavevector (the change in spectral phase per unit length) and a periodic $u_{i\mathbf{k}}(\mathbf{r})$ part, depending on the distance \mathbf{r} :

$$\varphi(\mathbf{k},\mathbf{r}) = u_{i\mathbf{k}}(\mathbf{r})e^{i\mathbf{k}\cdot\mathbf{r}} \quad (1.14)$$

The map of energies E against wavevector \mathbf{k} , $E(\mathbf{k})$, is better known as the crystal band structure and gives the position of the band gap as well as the Brillouin zones, where $E(\mathbf{k})$ reaches a maximum or a minimum.

An important characteristic of the electrons and holes in semiconductors is their effective mass. Because of the different forces experienced by an electron/hole in a crystal lattice, the carriers will no longer have the same rest mass as the one of a free carrier m_0 in vacuum, but rather an effective mass m^* . The effective mass describes how the crystal momentum of a carrier, $\mathbf{p} = m^* \mathbf{v} = \hbar\mathbf{k}$, where \mathbf{v} is the velocity, responds to an applied force \mathbf{F} .

$$\mathbf{F} = \frac{d\mathbf{p}}{dt} = m^* \frac{d\mathbf{v}}{dt} \quad (1.15)$$

Since the velocity is also expressed by $\mathbf{v} = \nabla_{\mathbf{k}} E(\mathbf{k})$, for the specific case of an electron in the conduction band, m_c^* is given by:

$$m_c^* = \hbar^2 \left(\frac{d^2 E_c(k)}{dk^2} \right)^{-1} \quad (1.16)$$

For example, m_c^* can be larger or smaller than m_0 : large values of m_c^* are indicative of conduction band electrons being strongly influenced by the atomic potentials. The same is true for holes in valence band. The effective masses of electron and holes are generally different due to the different curvature of the CB and VB, thus changing the forces experienced by each of the carriers.

Direct and indirect band gaps

When the minimum of the CB and the maximum of the VB occur for the same \mathbf{k} , the semiconductor is said to have a *direct band gap* and a photon of energy equivalent to the band gap (E_g) is sufficient to create an electron-hole pair through a vertical transition (Figure 1.3a). On the other hand, when the minimum of the CB and the maximum of the VB are not vertical (i.e. are found at different values of \mathbf{k}), the material is said to have an *indirect band gap* (Figure 1.3b). The consequence of this is that an optical transition is not possible only with a photon of energy equal to the band gap, since the crystal momentum $\mathbf{p} = \hbar\mathbf{k}$ is not conserved. Extra momentum has to be supplied by a vibration of the lattice, which is a *phonon*. It is also possible to observe an indirect transition by emission of a phonon. As a general result, optical absorption is generally weaker in indirect band gap materials (transitions are less probable) and it will be strongly dependent on the temperature.

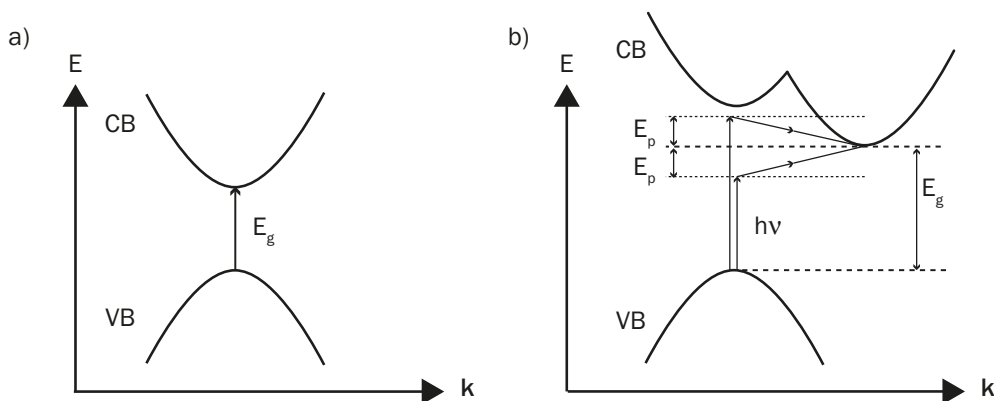


Figure 1.3 Absorption in a direct and indirect band structure

a) In a direct band structure, a photon with energy E_g is sufficient to promote an electron in the conduction band. b) For an indirect transition, a photon with $h\nu$ must be coupled to a phonon with energy E_p and $h\nu = E_g - E_p$. A transition can also occur by absorption of a photon of energy $h\nu = E_g + E_p$, thus resulting in emission of a photon of energy E_p .

It is useful to define here the *absorption coefficient* α of a material, which is a description of the attenuation of the light intensity $I(x)$ through a material of thickness dx :

$$\frac{dI}{dx} = -\alpha I \quad (1.17)$$

(1.17) integrates to the Lambert's law, with I_0 being the incoming light intensity:

$$I(x) = I_0 \exp(-\alpha x) \quad (1.18)$$

For a direct band gap material, it can be shown that the absorption coefficient is related to the energy of the incoming photon E :

$$\alpha_{dir}(E) = A'(E - E_g)^{1/2} \quad (1.19)$$

with A' being a constant dependent on the material.

In an indirect band gap material, this relation will be different and has to take into account the probability for the absorption or the emission of a phonon of energy E_p . The number of phonons N_p depends on the temperature T and is given by the Bose-Einstein statistics, with k_B being the Boltzmann constant:

$$N_p(T) = \frac{1}{\exp\left(\frac{E_p}{k_B T}\right) - 1} \quad (1.20)$$

Then the absorption coefficient for an indirect transition, where A'' is a constant dependent on the material, is given by:

$$\alpha_{ind}(E) = \frac{A''(E - E_g + E_p)^2}{\exp\left(\frac{E_p}{k_B T}\right) - 1} \quad (1.21)$$

From these equations, one can determine the type of transition in a semiconductor by plotting the absorption coefficient as a function of the energy. In the case of a direct transition, $\alpha_{dir}^2 = f(E)$ will give a straight line, and the intercept of the abscissa will give an estimation of the band gap E_g . The absorption of an exciton, i.e. an electron-hole pair bound together by Coulombic interaction, can be detected in this representations as a peak or shoulder in the graph of $\alpha_{dir}^2 = f(E)$. For an indirect transition, the function

$\alpha_{ind}^{-1/2} = f(E)$ should show two distinct linear parts (dependent on the temperature), corresponding to the absorption of a phonon for energies below E_g and to the absorption and/or emission of phonons for energies above E_g .

Electronic energy levels in the dark and under illumination

When electrons have no kinetic energy (at absolute zero temperature), they will fill all the lowest *available* levels up to the Fermi energy level E_F . In the case of the semiconductor, this means that all the states in the VB are occupied and all the states in the CB are empty. In an intrinsic (undoped) semiconductor, E_F lies in the middle of the bandgap, and corresponds to a level that would have a probability of occupation of $1/2$, if it was not forbidden. At higher temperatures, and for band gaps $E_g \leq 3kT$, the electrons will gain kinetic energy and some of them will be promoted in the CB. Thus the probability of finding an electron in a state of energy E will be given by the Fermi-Dirac statistics and will depend on the temperature T :

$$f(E,T) = \frac{1}{\exp\left(\frac{E - E_F}{k_B T}\right) + 1} \quad (1.22)$$

It is useful to see the Fermi level as the chemical potential of the electron in the semiconductor. For n-doped semiconductors, the Fermi level will be shifted towards higher energies, while in p-doped semiconductors, the Fermi level will be shifted towards lower energies. It can be shown from (1.22) that the Fermi levels at equilibrium in the dark, respectively for a n-doped and a p-doped semiconductor, are given by relationships resembling Nernst equation:

$$\begin{aligned} E_{F,n} &= E_C + kT \ln\left(\frac{N_n}{N_c}\right) \\ E_{F,p} &= E_V - kT \ln\left(\frac{N_p}{N_v}\right) \end{aligned} \quad (1.23)$$

With E_C, E_V being the position of the conduction and the valence band, N_C, N_V the effective conduction and valence band densities of states and N_n, N_p the densities of electrons and holes in the system.

These relationships will not hold anymore under illumination: the photogeneration of carriers will change the concentrations of electrons in the CB and holes in the VB, thus effectively shifting their Fermi levels. A local thermal equilibrium will be reached, with a different chemical potential, called the *quasi Fermi level*. The quasi Fermi levels, respectively for electrons and holes are defined as:

$$\begin{aligned} E_{F,n}^* &= E_C + kT \ln\left(\frac{N_n + n^*}{N_c}\right) \simeq E_C \\ E_{F,p}^* &= E_V - kT \ln\left(\frac{N_p + p^*}{N_v}\right) \simeq E_V \end{aligned} \quad (1.24)$$

where n^* and p^* are the densities of photogenerated electrons and holes. An interesting consequence is that the quasi Fermi levels of electrons and holes are very close respectively to the conduction band and valence band.

1.2 Dye-sensitized solar cell

The dye-sensitized solar cell (DSC) has undergone a long historical development that can be traced back in the 19th century, when the first sensitization of semiconductor was discovered by Moser.³ It is only in the 1960s though that the understanding of the mechanism of charge injection from photoexcited dye molecules into n-type semiconductor became clearer.⁴ Indeed, it appeared that a dye excited by light absorption could “inject” an electron in the conduction band of a semiconductor metal oxide such as ZnO or TiO₂, thereby marking the first step of the development of photoelectrochemical cells. This pioneering work showed that it is possible to harvest light from the visible part of the spectrum and use a semiconductor metal oxide (which in the case of TiO₂ only absorbs in the UV) as a conducting film for separating the charges. The electron injected in the semiconductor can then be extracted in an external electrical circuit, through a conductive glass, provided that a way to regenerate the dye is found. Usually, a redox mediator (liquid, solid, or gel electrolyte) and a counter electrode are used to reduce the oxidized dye and close the electric circuit. This resulted in 1985 in the dye-sensitized cell, also known as the Grätzel cell.⁵ A schematic presentation of the operating principles of the DSC is given in Figure 1.4.

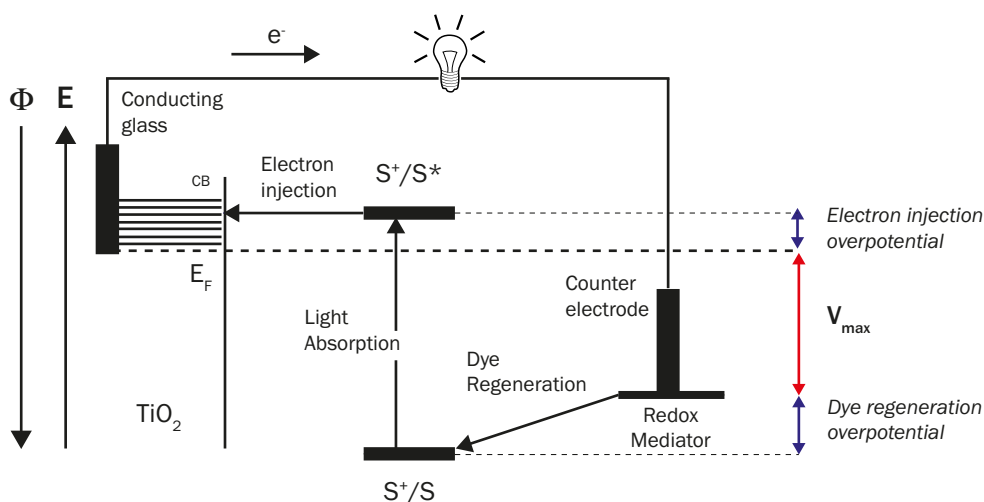


Figure 1.4 Operation principle and energy level scheme of a DSC

Upon light absorption in the sensitizer ($S \rightarrow S^*$), an electron is injected in the conduction band (CB) of TiO₂. The electron can then be extracted through a conductive glass (usually fluorine doped tin oxide, FTO) through an external circuit. A redox mediator is employed to regenerate the oxidized dye, while the redox mediator is regenerated at the counter electrode by electrons passed through the load, thus closing the circuit. The open-circuit voltage of the solar cell (red arrow, V_{\max}) corresponds to the difference between the redox potential of the mediator and the Fermi level (E_F) of the TiO₂.

The main advantage of this photoelectrochemical cell, which belongs to the molecular photovoltaic systems, is to separate the function of light absorption and carrier transport. This principle is different from conventional p-n junctions, where the semiconductor assumes these two roles simultaneously, thus rendering the system very sensitive to the purity of the starting material. The breakthrough introduced by Grätzel and co-workers consisted in increasing the effective surface area to ensure efficient harvesting of the light.^{5,6} Instead of using flat surfaces to deposit the dye, mesoporous oxides are employed to maximize the surface where the dye can be loaded. Twenty year of successive works have brought many more improvements, which will be summarized in the next sections. The dyes have been refined to harvest larger parts of the visible spectrum, up to the near infrared, TiO₂ conductivity has been improved through the addition of doping and specific treatments to insure a better necking (i.e. contact) of the particles. The electrolyte can be tuned to have a better match with the energy levels of the oxidized state. Usually triiodide/iodide couples are used but recently electrolytes based on cobalt have proven to be very efficient. Another fundamental turn was taken in 1998, with the introduction of a solid hole transport material, *spiro*-MeOTAD.⁷ The replacement of the liquid electrolyte by an organic film has many critical implications: indeed, it avoids the spilling or

evaporation of electrolyte from the sealing of the cell and at the same time avoids corrosion of the metal electrode.

1.2.1 TiO₂

The semiconductor metal oxide of choice to function as an acceptor and electron transporting material is anatase TiO₂, although some works have evidenced the possibility of using other oxides such as ZnO, SnO₂ and Nb₂O₅.⁸ The common property of these metal oxides is to have a wide bandgap (usually more than 3V), thus they do not absorb visible light. The preferential use of TiO₂ in DSCs is mainly related to the fact that this material is fairly cheap, abundant and most importantly, non-toxic.

From a practical point of view, in order to make a mesoporous framework on which to anchor the sensitizer, nanoparticles of TiO₂ from a colloidal solution are deposited on a conductive glass, either by doctor blading or screen-printing. The following step is then to fire in air the films at high temperatures in order to calcinate any organic residues as well as sintering the particles to create a continuous conductive network. The resulting film thickness can vary between 2 and 20 μm, with 10 to 30 nm diameter particles and porosity between 50 and 70%. While the most thermodynamically stable form of TiO₂ at room temperature is rutile for the macroscopic crystals, the DSCs employ the anatase form, which is more stable for nanocrystals smaller than 20 nm.⁹

The valence band is mainly constituted by the occupied 2p orbitals of the O²⁻ ions, while the conduction band is formed by the empty 3d orbitals of the Ti⁴⁺ ions. Surface Ti^{IV} sites are Lewis acids, thus offering a convenient way to attach dye molecules with electron-rich anchoring groups such as carboxylates (Figure 1.5).

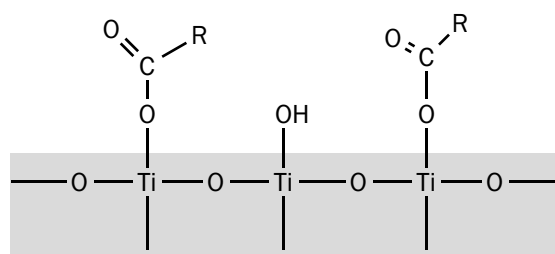


Figure 1.5 Chemical structure of TiO₂ surface grafted with carboxylated groups

Regardless to the preparation route, TiO₂ is usually slightly oxygen-deficient. This lack of oxygen, which can also be considered as the presence of Ti³⁺ impurities, is at the origin of

the n-doping of this semiconductor, which can be used as the photoanode of the electrochemical cell.

The determination of the unoccupied acceptor states, i.e the density of states (DOS) in TiO_2 is not trivial and many different results can be found in the literature.^{10,11} The presence of a broad distribution of trap states below the conduction band is generally accepted and is also known to be largely influenced by the local environment. It has been suggested that rather than a definite flat-band position, the nanocrystalline TiO_2 possesses an exponential tailing of the DOS, which can be tuned by addition of ions and dipolar molecules. This is achieved by the additives commonly introduced in the electrolyte or with the HTM. The additives can influence the surface charge and thus the position of the conduction band edge. In the case of the HTM, this will be explained in Chapter 3.

1.2.2 Dye

An ideal sensitizer should fulfil many specific requirements. At first, a sensitizer should absorb as much as possible from the visible spectrum, and have a sufficient molar extinction coefficient ϵ (usually ϵ in the range of 10^4 M cm^{-1} are considered good for a dye-sensitizer characterized by a broad absorption spectrum). Then, its excited energy level should be as close as possible to the lower edge of the conduction band of TiO_2 in order to efficiently inject while minimizing the energy losses by thermalisation of the carriers in the semiconductor oxide. Its redox potential should be well matched so that it can be regenerated via electron donation from the redox electrolyte. Last and not least, in order to successfully implement the DSC technology in our everyday's life, the sensitizer should be stable enough to sustain about 20 years of exposure to natural sunlight, which corresponds approximately to 10^8 turnover cycles.

In practice, the sensitizer is grafted onto the TiO_2 surface through suitable anchoring groups, e.g. carboxylate or phosphonate groups (Figure 1.6a). Deposition on the TiO_2 films is made from solution. The dye is beforehand dissolved in an appropriate solvent, usually a mixture of *tert*-butanol (tBuOH) and acetonitrile (MeCN). The mesoporous oxide film is heated to 500°C prior dipping into the dye solution in order to remove any residual water. The desired chemisorption of the dye consists in a perfect monolayer of dye; however it has been observed that high solution concentration as well as short dipping times can lead to aggregation problems, and thus more than a monolayer of dye at the surface of TiO_2 .¹²

Molecular engineering of sensitizers has been a constant driving force in the field of DSCs since the first seminal paper in 1991.⁶ The best photovoltaic performances are achieved with ruthenium polypyridil complexes, such as N3, N719, Z907^{13,14} however the last years have seen a large development of porphyrin dyes¹⁵ and organic dyes,¹⁶ with a push-pull donor- π -acceptor (D- π -A) structure such as in Y123.^{17,18}

With ruthenium-based dyes, the optical transition has metal-to-ligand charge transfer character (MLCT). Upon light absorption in the dye, an electron is transferred from the metal ion Ru(II) d-orbital to the π^* orbitals of the ligand. The HOMO is mainly constituted by the 4d orbitals of the ruthenium and 3p orbitals from the sulphur on the thiocyanate group, while the LUMO is concentrated on the π^* structure of the bipyridyl ligands, shared with the carboxylate groups.¹⁹ The electronic coupling between the dye and the Ti(3d) conduction band manifold will be determinant for the efficiency of injection, this is why a good anchoring of the dye at the surface of the oxide is necessary (Figure 1.6a).

In the case of the organics D- π -A dyes, the optical transition occurs between the donor (electron-rich HOMO) moiety and the acceptor (electron-poor LUMO) moiety, which is directly attached to the TiO₂ surface (Figure 1.6b). The HOMO is then far away from the interface, rendering the back reaction of the electron more difficult.

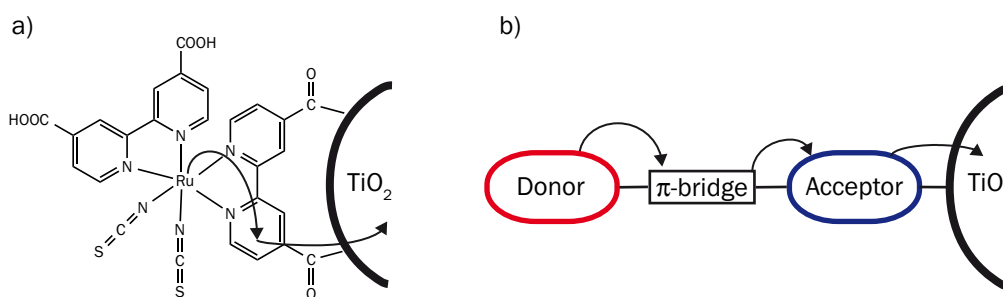


Figure 1.6 Dye | TiO₂ interface

a) Schematic view of a ruthenium dye (N3) attached to the TiO₂ surface via its carboxylate groups. b) Schematic view of a D- π -A dye attached to the TiO₂ surface. The arrows indicate the electron transfer steps after light absorption.

1.2.3 Liquid redox mediators

Liquid redox mediators will only be succinctly described, as this is not the main focus of the present work. A redox mediator must regenerate the dye: its redox potential should thus be more negative than the redox potential of the ground state dye. However, in order to keep a high open circuit voltage, the dye regeneration overpotential (Figure 1.4) should

be minimised while still keeping enough thermodynamic force for dye regeneration. So far, the couple triiodide/iodide was the best redox mediator in conjunction with ruthenium-based dyes. The triiodide/iodide redox couple (I_3^-/I^-) has a suitable redox potential allowing for efficient dye regeneration. In order to increase the available concentration of iodide for the regeneration reactions, electrolytes with high iodide concentrations can be prepared using a pure iodide ionic liquid of the dialkyl imidazolium family, or by dissolving the latter in an appropriate solvent. The reduction of the triiodide species by photoinjected electrons on the surface of TiO_2 is very slow and therefore limits the cathodic dark current. However, the (I_3/I^-) mixture absorbs slightly in the visible region. Another drawback consists in the slow regeneration reaction (Figure 1.4) obtained with this electrolyte, due to the complex chemistry of its particular redox reaction, involving the presence of two iodide anions for the exchange of one electron with an oxidized sensitizer.²⁰ More recently, different electrolytes, based on one-electron redox couples, such as in particular $[Co(bpy-pz)_2]^{3+/2+}$, have been shown to allow for improved conversion efficiencies.^{15,17} However, careful engineering of the dye must be made in order to account for the faster charge recombination at the TiO_2 | electrolyte interface.

1.2.4 The solid-state solar cell

Besides the conventional liquid DSCs, substantial research efforts have been concentrated on gel and solid-state electrolyte, which could be deposited on the mesoporous framework by easy techniques such as spin-coating or dip-coating. This solid alternative is a way to circumvent the problems related to the leakage of the electrolyte and corrosion of the electrode. Early work by Tennakone et al.²¹ showed that a solid-state device based on CuI could deliver 4.7% power conversion efficiency. However, CuI proved to be unstable. Organic molecular and polymer semiconductors represent another class of materials potentially useful as hole conductors. They are solution processable, cheap and versatile, although their mobility is generally lower than in inorganic-based compounds. Following the pioneer work of Bach et al., in 1998,⁷ that featured a solid-state DSC based on the hole transport material (HTM) *spiro*-MeOTAD with a solar-to-electric power conversion efficiencies of 0.74%, the conjunct efforts of many research groups allowed reaching efficiencies close to 8% for a dye-sensitized film impregnated with *spiro*-MeOTAD.²² Many other types of organic HTM have been tested, but so far *spiro*-MeOTAD remains unsurpassed.²³⁻²⁵ Throughout this thesis, we thus used *spiro*-MeOTAD as the standard for

our measurements. The chemical structure is shown in Figure 1.7, where the *spiro* center linking the two fluorene moieties of the molecule is evident.

The main issues associated to the solid-state system, which are the poor charge mobility in the HTM, as well as its partial or incomplete pore filling of the mesoscopic structure, will be discussed in detail in Chapter 3.

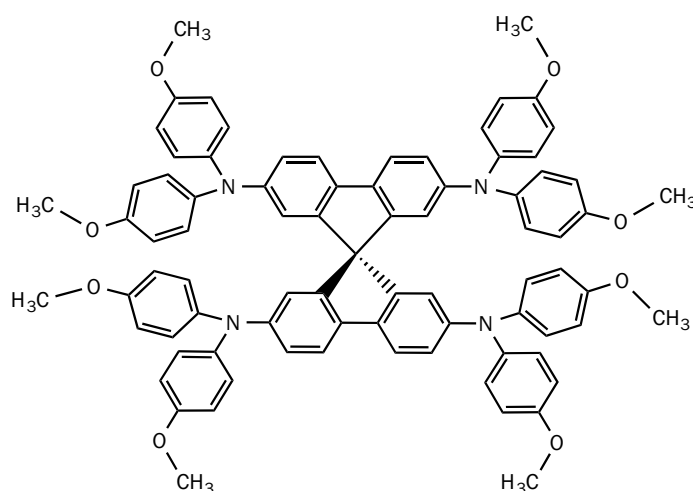


Figure 1.7 Chemical structure of 2,2',7,7'-tetrakis-(N,N-di-p-methoxyphenylamine)-9,9'-spirobifluorene, (*spiro*-MeOTAD)

1.3 Dynamics of charge transfer processes

As already mentioned, the efficient photovoltaic function of these cells is based upon the light-induced charge separation at the dye | TiO₂ interface. Indeed, due to the small size on the TiO₂ nanoparticles (< 30 nm diameter), it is not possible to use the properties of a built-in electric field to separate the charges. The crucial parameter that governs this type of cell is then the control of the dynamics at the various interfaces. Efficient sensitization requires that the rate for interfacial electron injection has to be larger than the decay of the excited state to the ground state by luminescence or non-radiative processes. In the same way, regeneration of the oxidized state by the electrolyte or HTM has to be faster than the recombination with injected electrons. Another process that must be avoided is the recombination of electrons in TiO₂ to the oxidized electrolyte or HTM.

Hence, the main challenge in these systems is the kinetic competition within all these reactions, and how to selectively tune the timescale of the different processes in order to increase the efficiency of the cell. It is then of paramount importance to study the

timescales of all these different reactions. We will briefly review the literature for all of these specific pathways.

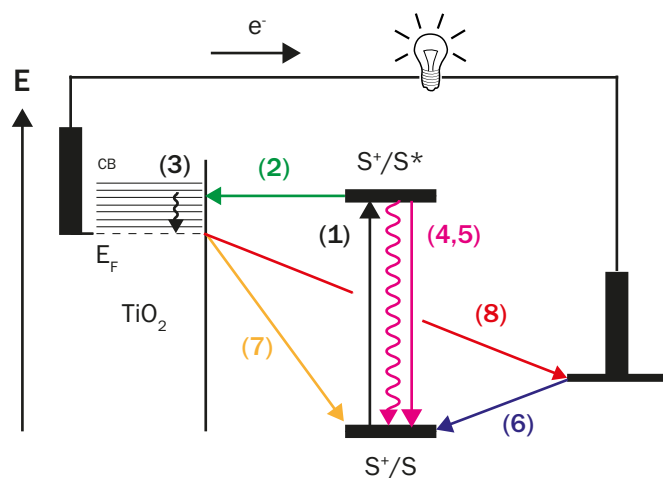


Figure 1.8 Schematic view of charge separation and charge recombination processes

(1) Light absorption by the sensitizer S (10^{-16} - 10^{-15} s). (2) Electron injection into the semiconductor oxide (10^{-15} s - 10^{-11} s). (3) Thermalisation in the conduction band of TiO_2 (10^{-12} s). (4, 5) Radiative and non-radiative deactivation processes of the dye sensitizer (10^{-9} s). (6) Regeneration of the oxidized sensitizer S^+ by a redox mediator (i.e. interception of the oxidized state, 10^{-9} s - 10^{-6} s). (7) Back electron transfer from the TiO_2 conduction band to the oxidized sensitizer S^+ (10^{-6} s - 10^{-3} s). (8) Back electron transfer from the TiO_2 conduction band to the oxidized redox mediator (10^{-6} s - 10^{-3} s when using HTM, 10^{-2} s - 10^0 s when using the $(\text{I}_3^-/\text{I}^-)$ couple).

Electron injection

Electron injection from dye sensitizers grafted on the TiO_2 surface (process (2) in Figure 1.8) has been widely studied in the solar cell community in the past decades, both theoretically and with experimental spectroscopic techniques. Theoretical studies have suggested that the rate for electron transfer can be extremely fast (from ps to fs) in the case where a good energetic overlap is achieved between the dye excited state and the conduction band of TiO_2 .²⁶⁻²⁹ Following the first studies of Tachibana et al. in 1996, many spectroscopists have measured experimentally the rate of electron injection into TiO_2 and reported multiphasic kinetics with an ultrafast component (10-100 fs) as well as a slower exponential in the picosecond timescale (10-100 ps).³⁰⁻³⁴ A recent study by Bräm et al. suggests that electron injection from the singlet state of ruthenium sensitizers can be even faster than 10 fs.³⁵ The origin of the slower component can be ascribed to many different factors that depend on the preparation conditions, such as the pH of the surface, the electrolyte composition, the nature of the TiO_2 , the adsorption on the dye at the surface, as well as the excitation wavelength.^{12,36-39} A detailed description of the results of

these studies is beyond the scope of this introduction but it can be highlighted that all of them agree on the presence of a varying fraction of ultrafast component.

Electron injection is in kinetic competition with deactivation of the excited state (to the ground state by fluorescence and internal conversion, and to some extent by intersystem crossing to the triplet state). Internal conversion and vibrational relaxation have recently been estimated to occur on a timescale of less than 10 fs, which is similar to what observed for electron injection.⁴⁰ The electron injection efficiency can be defined as:

$$\eta_{inj} = \frac{k_{inj}}{k_{inj} + \sum k_{deact}} \quad (1.25)$$

where k_{inj} is the rate constant for electron injection and $\sum k_{deact}$ is the sum of the rate constant for radiative and non-radiative deactivation processes (processes (4) and (5) in Figure 1.8). The lifetime of the dye excited state should be large enough to allow electron injection: usually the deactivation pathways of the sensitizer occur in the nanosecond timescale, thus leaving enough time for the electron injection to take place. Such deactivation process can be a loss pathway when loosely bound dye aggregates are present in the system, where the injection does not take place efficiently.

Back electron transfer to the oxidized sensitizer

Back electron transfer, or recombination from the TiO₂ CB to the oxidized sensitizer (process (7) in Figure 1.8) can be up to 10 orders of magnitude slower than electron injection.⁴¹ It usually ranges from the μ s to ms and is a process largely determined by the nature of the dye. Such a difference between the rate of electron injection and the one for back electron transfer can be ascribed to the back electron transfer lying in the inverted Marcus region, while the electron injection is activationless. It is also to ascribe, for the electron injection, to the presence of a continuum of acceptor levels in the TiO₂ that can easily accept an electron, and where a process of trapping of the electron can take place in addition. On the opposite, back electron transfer occurring from the continuum of energy levels such as in a semiconductor to a discrete electronic state of the dye molecule will be less probable, and will require detrapping of the electron. Position of the HOMO far away from the interface, while the LUMO is directly attached to the TiO₂ surface has also to be taken into account (cf. section 1.2.2).

The efficiency of a DSC will be directly related to the kinetic competition between the back electron transfer to the oxidized sensitizer and the interception of the oxidized state by the electrolyte. The dye regeneration yield is given by:

$$\eta_r = \frac{k_r}{k_r + k_b} \quad (1.26)$$

where k_r is the rate constant for dye regeneration and k_b is the rate constant for recombination. Ideally, k_r should be as larger than k_b as possible, in order to have the regeneration yield as close to 1 as possible.

Back reaction kinetics was found to be strongly dependent upon electron concentration (and thus light intensity), electrolyte composition (in particular the presence of potential determining ions such as Li^+), and the application of an electrical bias to the TiO_2 film.^{42,43} Many different strategies have been implemented in order to retard recombination in DSCs. For example, blocking layers on the surface of TiO_2 can be applied in order to retard the recombination, such as for example TiCl_4 treatments (cf. chapter 4). Al_2O_3 layers deposited by atomic layer deposition have also shown to be efficient.⁴⁴ Another strategy currently employed is the use of D- π -A dyes (cf. section 1.2.2), where the HOMO is spatially far away from the surface.

Interception of the oxidized state

While some tentative have been made to regenerate the dye oxidized form by intramolecular electron transfer, for example by using a dyad design where the hole is translated away from the TiO_2 surface,⁴⁵ the most effective and widely used way to regenerate the Ru^{III} center is by intermolecular regeneration with a liquid redox mediator such as the couple triiodide/iodide described in section 1.2.3. This process is described by the blue arrow in Figure 1.8 (process 6). As it is shown from equation (1.26), a good electrolyte must be engineered in order to be as fast as possible with respect to the recombination reactions. Thus the ideal timescale for regeneration is between the ns and the μs timescale. (I_3^-/I^-) suffer from one fundamental drawback as described in section 1.2.3: they imply a two-atoms reaction that can only be slower than a one-electron regeneration reaction. The use of cobalt complexes as electrolytes is a way to circumvent this two-step reaction, but still not all dyes can function with this very bulky electrolyte.

In **solid-state** DSCs, the situation is slightly different. The interception of the oxidized

dye state can occur very rapidly (ps to ns timescale),⁴⁶ since it originates from a one-step regeneration reaction. This process is rather referred to as “hole injection” into the HTM and will be the object of chapter 3.

Back reaction with the oxidized electrolyte or oxidized HTM

The back reaction with the oxidized redox mediator is shown as process (8) in Figure 1.8, and is generally referred to as the electron lifetime. While the back reaction of electrons with the oxidized electrolyte is rather slow (ms timescale), for the same reasons than for the forward regeneration reaction, the back reaction of electrons with oxidized HTM is also much faster (μ s timescale). In order for the surface of TiO_2 not to come into contact of HTM molecules, specific strategies such as molecular engineering of the dye are possible, e.g. the long chains of the Z907 dye. The chains will then block the access to the surface of TiO_2 . This subject will be addressed in detail in Chapter 3. Blocking barriers are also an option, and in this thesis, we will address in Chapter 4 the special case of how TiCl_4 treatment can be applied to decrease the charge recombination with oxidized *spiro*-MeOTAD.

1.4 Perovskite-based solar cells

1.4.1 Perovskites: structure and properties

The latest, most exciting development in the field of solid-state solar cells is constituted by a new unique material from the class of perovskites. Initially thought as light absorbers, we will show that they have many other interesting properties. Perovskites originate from the discovery of CaTiO_3 by the Russian mineralogist Lev Perovski. Later, many materials with the same crystal structure were discovered and more generally perovskite represent AMX_3 crystals, where A is a cation, M a metal cation, X an oxide or a halide anion. Perovskites extend as a three-dimensional network formed by an MX_6 corner-sharing octahedron. Perovskites have cubic geometry but in reality the lattice is never ideal and can present distortions that will affect physical and optical properties of the crystal. Additionally, the size of cation and metal ion will influence the lattice structure and will be crucial parameter to modulate the optical and electronic properties of the material.^{47,48} Organic-inorganic perovskites, where A is an organic cation, are of special interest in the

perovskite family due to their unique structure, where sheets of organic and inorganic components alternately stack on the molecular scale. The organic group usually consists of an alkyl chain or a single-ring aromatic group. These organic-inorganic hybrids are particularly promising because of their unique optical and electronic properties, where the organic layers help to define the degree of interaction between and the electronic properties arising in the inorganic layers. In addition to that, these materials can be easily prepared by wet-chemical synthetic routes, which offer potentially lower-cost and lower-temperature processes for materials preparation.

Herein, we shall focus mainly on the family of lead halide perovskites $\text{CH}_3\text{NH}_3\text{PbX}_3$, where $\text{X} = \text{I}, \text{Cl}, \text{Br}$, and more specifically on $\text{CH}_3\text{NH}_3\text{PbI}_3$ (crystal structure shown on Figure 1.9) but perovskites based on tin instead of lead could also be considered. One peculiarity of the perovskite containing small organic cations is that the CH_3NH_3^+ is free to rotate in the lattice.^{49,50}

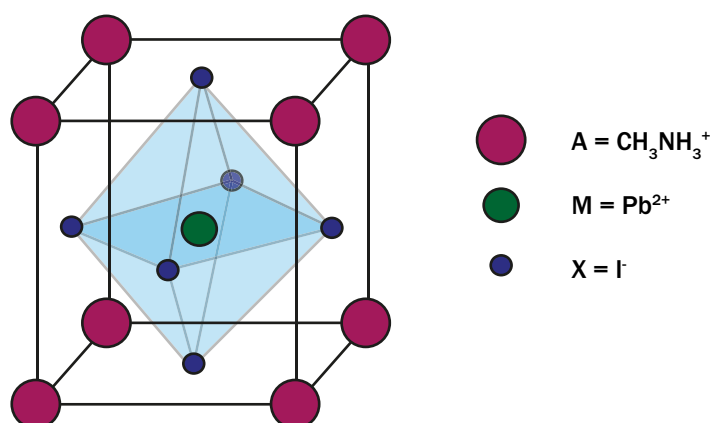


Figure 1.9 Crystal structure of $\text{CH}_3\text{NH}_3\text{PbI}_3$

Optical properties

Hybrid organic-inorganic perovskites are interesting optical properties mainly because of their direct band gap that can be tuned either by changing the alkyl group, the metal atom or the halide.⁵¹⁻⁵⁴

For the $\text{CH}_3\text{NH}_3\text{PbI}_3$, a direct band gap has been determined in the study by Kim et al.⁵⁵ Optical band gap (E_g) was determined based on diffuse reflectance spectroscopy, and the position of the valence band maximum was determined by ultraviolet photoelectron spectroscopy (UPS) measurements. A value of $E_g = 1.5$ eV was reported for $\text{CH}_3\text{NH}_3\text{PbI}_3$ deposited on mesoporous TiO_2 , and the position of the valence band energy (E_V) was estimated to -5.43 eV below vacuum level, which has been confirmed by Schulz et al.⁵⁶

Thus, from the optical band gap, the position of the conduction band can be estimated at $E_C = -3.93\text{eV}$ vs. vacuum.

Perovskites usually exhibit sharp resonances in their room-temperature optical absorption spectra,^{57,58} which arise from an exciton state associated with the inorganic semiconducting layers. This feature is of particular interest and will be discussed in this thesis in Chapters 5 and 6. Relatively low binding energies of approximately 50 meV are reported for excitons in $\text{CH}_3\text{NH}_3\text{PbI}_3$, due to their large Bohr radius (22 Å) and thus their reduced Coulomb interaction.^{59,60}

Electronic properties

Perovskites based on tin have long been known to exhibit high values of conductivity.^{61,62} Mitzi et al. reported in 1994 that layered tin-based perovskite, where tin iodide sheets were intercalated between organic layers, showed a transition from semiconducting to metallic behavior with increasing number of layers.⁶³ In a their comprehensive study, Stoumpos et al. report the mobilities for many different lead and tin perovskites, as determined through Hall effect and resistivity measurements. They find electron mobilities of $2320\text{ cm}^{-2}\text{ V}^{-1}\text{ s}^{-1}$ for $\text{CH}_3\text{NH}_3\text{SnI}_3$ and $66\text{ cm}^{-2}\text{ V}^{-1}\text{ s}^{-1}$ for $\text{CH}_3\text{NH}_3\text{PbI}_3$. These values are remarkably high and comparable to those of classical semiconductors like Si ($1400\text{ cm}^{-2}\text{ V}^{-1}\text{ s}^{-1}$). The authors also point out the fact that the very low carrier concentrations measured is indicative of a nearly intrinsic semiconductors. Effective diffusion lengths for $\text{CH}_3\text{NH}_3\text{PbI}_3$ as measured in solar cell architecture are discussed more extensively in section 1.4.3.

Due to the presence of a CH_3NH_3^+ cation and a PbX_3^- , $\text{CH}_3\text{NH}_3\text{PbI}_3$ can be considered as an ionic compound with a permanent electric dipole moment; for this reason, its dielectric constant is relatively high and initially estimated to 6.5,⁶⁴ but recent reports given even higher values, up to 30.⁶⁵ The high dielectric constant also explains the low binding energies of the exciton, since the photoinduced charges can be effectively screened by the dipoles of the lattice.

1.4.2 Perovskite in photovoltaic devices

The first report of perovskite materials used in devices for light energy conversion was made by Miyasaka and coworkers in 2009.⁶⁶ This work employed $\text{CH}_3\text{NH}_3\text{PbX}_3$ ($\text{X} = \text{Br}, \text{I}$) perovskite nanocrystals to replace the conventional dye sensitizer, in liquid electrolyte-based DSCs. They measured a relatively low power conversion efficiency (PCE)

of 3.8% and 3.1 % in $\text{CH}_3\text{NH}_3\text{PbI}_3$ - and $\text{CH}_3\text{NH}_3\text{PbBr}_3$ -based cells, respectively. Interestingly, a very high photovoltage was reported, up to 0.96 V, achieved with the lead bromide-based cell, which is an impressive value. Soon after, the PCE was raised to 6.5%, as reported in the work by Im et al.⁶⁷ However, these cells suffered from a major drawback, as they were decomposing very rapidly, typically 80% degradation after 10 min of illumination, due to the dissolution of the perovskite in the liquid electrolyte.

The interest in the perovskite system has soared with its introduction in the solid-state counterpart of the DSC, using *spiro*-MeOTAD. Record efficiencies of 9.7% were obtained for $\text{CH}_3\text{NH}_3\text{PbI}_3$ deposited on TiO_2 mesoporous framework,⁵⁵ while in the same period Lee et al. reported PCE of 10.9% for a supposedly mixed halide $\text{CH}_3\text{NH}_3\text{PbI}_2\text{Cl}$ deposited on Al_2O_3 framework,⁶⁸ where no extraction of the charges in the mesoporous oxide is possible. Due to the high short-circuit currents and photovoltages (respectively close to 20 mA cm⁻² and 1 V), these two works have attracted the attention of a very large scientific community and triggered the development of many studies using these perovskites in various photovoltaic architectures.^{53,69-72}

The classic preparation route for perovskite-based devices consisted in deposition from a precursor solution containing $\text{CH}_3\text{NH}_3\text{I}$ and PbI_2 in γ -butyrolactone. It was initially thought that in this way perovskite was deposited as quantum dots. The most recent literature seems to agree on the fact that this is not the case, in particular with the new processing methods. Indeed recently, a breakthrough in PCE was achieved by using a modified perovskite processing method, called the sequential deposition method, where PbI_2 is first spin-coated from a dimethylformamide solution on the TiO_2 film and then successively converted to perovskite by dipping into a $\text{CH}_3\text{NH}_3\text{I}$ solution in isopropanol. This new method has led to a PCE of 15% and a certified value of 14.1% with high reproducibility.⁷³ The last record to date on mesoporous TiO_2 has been certified for a device by a group at the Korean Research Institute of Chemical Technology (PCE=16.2%) and efficiencies above 17% are reported for research devices at the laboratory scale.⁷⁴ Perovskite layers on flexible substrates have also been reported, paving the route for numerous types of applications of these photovoltaic devices.⁷⁵⁻⁷⁸

1.4.3 Perovskite, what is your function?

Naturally, the question of the exact role of the perovskite material arose with the work presented by Snaith and co-workers, reporting 10% cells on Al_2O_3 framework.⁶⁸ The

authors observed that the open-circuit voltage (V_{OC}) obtained with these insulating Al_2O_3 -based devices was 200 mV higher than with a TiO_2 -based device, mainly because no energy losses associated to electron injection in the mesoporous oxide could take place. Furthermore, the hypothesis of a large diffusion length in the perovskite was formulated. The perovskite, initially thought as the analogous of a dye, seemed to be a material slightly more complicated than a common sensitizer: both its light harvesting properties and charge transport properties have to be considered.

Meanwhile, Etgar et al.,⁷⁹ demonstrated cells made of $CH_3NH_3PbI_3$ deposited on TiO_2 , where the perovskite material functions itself as the hole transport material. Such devices recently reached 8% efficiency.⁸⁰ The ambipolar character of this material thus became quite clear. Recently, Snaith and co-workers also reported that perovskite-based devices employing perovskite as a thin evaporated film can work with power conversion efficiencies as high as 15% without the need for a complex mesoporous architecture,⁷⁸ thus also demonstrating that this material can work as a *p-i-n* junction, with *n* being a thin compact layer of TiO_2 , *p* being an overlayer of *spiro*-MeOTAD and *i* corresponding to the perovskite evaporated layer. This has been recently confirmed in a recent study employing scanning electron microscopy techniques, which also suggests that this *p-i-n* operation mode is also valid for the mesoporous configuration, and for the $CH_3NH_3PbI_{3-x}Cl_x$ perovskite.⁸¹

The determination of the diffusion length of the carriers has been the object of many efforts. Both electrons and holes diffusion lengths appear to be very similar according to several reports.^{82,83} On the other hand, Edri et al. provide data supporting the holes being more efficiently extracted than the electrons for $CH_3NH_3PbI_3$.⁸⁴ It is also very likely to depend on the crystallinity of the material, and thus on the preparation conditions. A recent theoretical work supports the ambipolar character of $CH_3NH_3PbI_3$.⁸⁵ The authors report the effective masses for photogenerated electrons and holes, including the effect of spin-orbit coupling, and find very similar values for both carriers ($m_c^* = 0.23 m_0$ and $m_v^* = 0.29 m_0$, thus being an indication of a reduced interaction with the atomic potentials). These values are comparable to those of silicon, thus explaining the long-range photocarrier transport. In another theoretical work, first-principles calculations using Density Functional Theory have shown that defects in $CH_3NH_3PbI_3$ are shallow: since non-radiative recombination is mainly associated with deeper levels, the presence of these shallow levels could explain the long electron and hole diffusion lengths reported above.⁸⁶

The authors also point out that the conductivity might be tuned from p-type to n-type by appropriate control of growth conditions.

It is important to mention that some important differences between the pure iodide-based perovskite and the mixed halide $\text{CH}_3\text{NH}_3\text{PbI}_{3-x}\text{Cl}_x$ have been noticed. Diffusion lengths of 100 nm for electrons and holes were reported for $\text{CH}_3\text{NH}_3\text{PbI}_3$,⁸³ while electrons and holes diffusion lengths in $\text{CH}_3\text{NH}_3\text{PbI}_{3-x}\text{Cl}_x$ were found to be one order of magnitude higher, exceeding 1 μm .^{81,82} Other works support the finding that a small amount of Cl doping dramatically improves the charge transport properties without altering its optical properties.⁸⁷

As an additional interesting characteristic to note in this system, the high dielectric constant mentioned in the section above has implications in the capacitance properties of the perovskite: indeed, impedance spectroscopy studies have shown that $\text{CH}_3\text{NH}_3\text{PbI}_3$ can work as a capacitor and accumulate charges.⁸⁸ This capacitor-like behavior can be rationalized by a reorientation of the methylammonium cation in order to mask the charge from the inorganic framework PbI_3 .

With their spectacular evolution within only a few years, perovskite-based devices thus appear as the holy grail of photovoltaic devices. The only main concern that remains up to now is the presence of lead. Some attempts to replace lead by tin have been made but remain unsuccessful because of the lower stability of tin-based perovskites. However, a recent review put this in perspective: indeed, for a production capacity of 1 TW per year, less than 10,000 tons of lead would be needed. As a comparison, 4 million tons per year of lead are used for lead-acid batteries.⁸⁹ Therefore, it seems that lead should not be such a concern.

In this thesis, we shall focus on the photophysical and photochemical properties of solid-state systems based on $\text{CH}_3\text{NH}_3\text{PbI}_3$. The main questions that arise with this material are first of all the photophysics upon light absorption, but also the consecutive charge transfer processes. The photophysics of $\text{CH}_3\text{NH}_3\text{PbI}_3$ will be discussed in Chapter 5. Charge separation processes at the heterojunction are studied in this thesis in detail and are the object of Chapter 6. Charge recombination, within the material and at the various interfaces will also be followed by spectroscopic techniques. This thesis thus reports for the first time the dynamics of charge transfer processes in a perovskite-based solar cell.

1.5 References

The first part of this chapter (section 1.1) is based on the following books:

Moser, J.-E. *Processus Photochimiques, Lectures Notes*; EPFL: 2008-2009.

Drabbels, M. *Quantum Chemistry, Lectures Notes*; EPFL: 2006-2007.

Suppan, P. *Chemistry and Light*, The Royal Society of Chemistry, 1994

Nelson, J. *The Physics of Solar Cells*, Imperial College Press, 2003.

Turro, N. J. *Modern Molecular Photochemistry*; University Science Books, 1991.

Balzani, V., Ed.; *Electron Transfer in Chemistry*; volumes 1-5, Wiley-VCH, 2001.

1. International Energy Agency. Key World Energy Statistics. www.iea.org (2013).
at<<http://www.iea.org/publications/freepublications/publication/name,31287,en.html>>
2. Baxter, J. B., Richter, C. & Schmittenmaer, C. A. Ultrafast carrier dynamics in nanostructures for solar fuels. *Annu. Rev. Phys. Chem.* 65, 423–447 (2014).
3. Moser, J. Notiz über Verstärkung photoelektrischer Ströme durch optische Sensibilisierung. *Monats. Chem.* 8, 373–373 (1887).
4. Gerischer, H., Michel-Beyerle, M. E., Rebentrost, F. & Tributsch, H. Sensitization of Charge Injection Into Semiconductors with Large Band Gap. *Electrochim. Acta* 13, 1509–1515 (1968).
5. Desilvestro, J., Grätzel, M., Kavan, L., Moser, J. & Augustynski, J. Highly efficient sensitization of titanium dioxide. *J. Am. Chem. Soc.* 107, 2988–2990 (1985).
6. O'Regan, B. C. & Grätzel, M. A low-cost, high-efficiency solar cell based on dye-sensitized. *Nature* 353, 737–740 (1991).
7. Bach, U. *et al.* Solid-state dye-sensitized mesoporous TiO₂ solar cells with high photon-to-electron conversion efficiencies. *Nature* 395, 583–585 (1998).
8. Jose, R., Thavasi, V. & Ramakrishna, S. Metal Oxides for Dye-Sensitized Solar Cells. *Journal of the American Ceramic Society* 92, 289–301 (2009).
9. Kavan, L. in *Dye-sensitized solar cells* (Kalyanasundaram, K.) 45–81 (EPFL Press, 2010).
10. Ardo, S. & Meyer, G. J. Photodriven heterogeneous charge transfer with transition-metal compounds anchored to TiO₂ semiconductor surfaces. *Chem. Soc. Rev.* 38, 115–164 (2009).
11. Hagfeldt, A., Boschloo, G., Sun, L., Kloo, L. & Pettersson, H. Dye-Sensitized Solar Cells. *Chem. Rev* 110, 6595–6663 (2010).

12. Wenger, B., Grätzel, M. & Moser, J.-E. Rationale for kinetic heterogeneity of ultrafast light-induced electron transfer from Ru(II) complex sensitizers to nanocrystalline TiO₂. *J. Am. Chem. Soc.* 127, 12150–12151 (2005).
13. Nazeeruddin, M. K. *et al.* Conversion of light to electricity by cis-X₂bis (2, 2'-bipyridyl-4, 4'-dicarboxylate) ruthenium (II) charge-transfer sensitizers (X= Cl-, Br-, I-, CN-, and SCN-) on nanocrystalline titanium dioxide electrodes. *J. Am. Chem. Soc.* 115, 6382–6390 (1993).
14. Robertson, N. Optimizing dyes for dye-sensitized solar cells. *Angew. Chem. Int. Ed. (English)* 45, 2338–2345 (2006).
15. Yella, A. *et al.* Porphyrin-Sensitized Solar Cells with Cobalt (II/III)-Based Redox Electrolyte Exceed 12 Percent Efficiency. *Science* 334, 629–634 (2011).
16. Mishra, A. & Fischer, M. Metal-Free Organic Dyes for Dye-Sensitized Solar Cells: From Structure: Property Relationships to Design Rules. *Angew. Chem.* (2009).
17. Yum, J.-H. *et al.* A cobalt complex redox shuttle for dye-sensitized solar cells with high open-circuit potentials. *Nat. Commun.* 3, 631 (2012).
18. Tsao, H. N. *et al.* Cyclopentadithiophene Bridged Donor-Acceptor Dyes Achieve High Power Conversion Efficiencies in Dye-Sensitized Solar Cells Based on the tris-Cobalt Bipyridine Redox Couple. *ChemSusChem* 4, 591–594 (2011).
19. Balzani, V. *Electron Transfer in Chemistry: Molecules-level electronics, imaging and information, energy and the environment.* (Wiley-VCH, 2001).
20. Teuscher, J. *et al.* Kinetics of the Regeneration by Iodide of Dye- Sensitizers Adsorbed on Mesoporous Titania. *J. Phys. Chem. C* (2014).
21. Tennakone, K. & Kumara, G. A dye-sensitized nano-porous solid-state photovoltaic cell. *Semicond. Sci. Technol.* 1689–1693 (1995).
22. Burschka, J. *et al.* Tris(2-(1H-pyrazol-1-yl)pyridine)cobalt(III) as p-type dopant for organic semiconductors and its application in highly efficient solid-state dye-sensitized solar cells. *J. Am. Chem. Soc.* 133, 18042–18045 (2011).
23. Kroeze, J. E. *et al.* Parameters influencing charge separation in solid-state dye-sensitized solar cells using novel hole conductors. *Adv. Funct. Mater.* 16, 1832–1838 (2006).
24. Midya, A., Xie, Z., Yang, J. & Chen, Z. A new class of solid state ionic conductors for application in all solid state dye sensitized solar cells. *Chem. Comm.* (2010).

25. Smestad, G. *et al.* A technique to compare polythiophene solid-state dye sensitized TiO₂ solar cells to liquid junction devices. *Sol. Energ. Mat. Sol. Cells* 76, 85–105 (2003).
26. Stier, W. & Prezhdo, O. V. Nonadiabatic Molecular Dynamics Simulation of Light-Induced Electron Transfer from an Anchored Molecular Electron Donor to a Semiconductor Acceptor. *J. Phys. Chem. B* 106, 8047–8054 (2002).
27. Stier, W., Duncan, W. R. & Prezhdo, O. V. Thermally Assisted Sub-10 fs Electron Transfer in Dye-Sensitized Nanocrystalline TiO₂ Solar Cells. *Adv. Mater.* 16, 240–244 (2004).
28. Duncan, W. R., Stier, W. M. & Prezhdo, O. V. Ab Initio Nonadiabatic Molecular Dynamics of the Ultrafast Electron Injection across the Alizarin-TiO₂ Interface. *J. Am. Chem. Soc.* 127, 7941–7951 (2005).
29. Duncan, W. R. & Prezhdo, O. V. Nonadiabatic molecular dynamics study of electron transfer from alizarin to the hydrated Ti⁴⁺ ion. *J. Phys. Chem. B* 109, 17998–18002 (2005).
30. Tachibana, Y., Moser, J.-E., Grätzel, M., Klug, D. R. & Durrant, J. R. Subpicosecond interfacial charge separation in dye-sensitized nanocrystalline titanium dioxide films. *J. Phys. Chem.* 100, 20056–20062 (1996).
31. Hannappel, T., Burfeindt, B., Storck, W. & Willig, F. Measurement of ultrafast photoinduced electron transfer from chemically anchored Ru-dye molecules into empty electronic states in a colloidal anatase TiO₂ film. *J. Phys. Chem. B* 101, 6799–6802 (1997).
32. Asbury, J. B. *et al.* Femtosecond IR Study of Excited-State Relaxation and Electron-Injection Dynamics of Ru(dcbpy)₂(NCS)₂ in Solution and on Nanocrystalline TiO₂ and Al₂O₃ Thin Films. *J. Phys. Chem. B* 103, 3110–3119 (1999).
33. Tachibana, Y., Haque, S. A. & Mercer, I. P. Electron Injection and Recombination in Dye Sensitized Nanocrystalline Titanium Dioxide Films: A Comparison of Ruthenium Bipyridyl and Porphyrin Sensitizer Dyes. *J. Phys. Chem. B* (2000).
34. Benkő, G., Kallioinen, J., Korppi-Tommola, J., Yartsev, A. P. & Sundström, V. Photoinduced ultrafast dye-to-semiconductor electron injection from nonthermalized and thermalized donor states. *J. Am. Chem. Soc.* 124, 489–493 (2002).
35. Bräm, O., Cannizzo, A. & Chergui, M. Ultrafast fluorescence studies of dye sensitized solar cells. *Phys. Chem. Chem. Phys.* 14, 7934–7937 (2012).

36. Asbury, J. B., Anderson, N. A., Hao, E., Ai, X. & Lian, T. Parameters Affecting Electron Injection Dynamics from Ruthenium Dyes to Titanium Dioxide Nanocrystalline Thin Film. *J. Phys. Chem. B* 107, 7376–7386 (2003).
37. Myllyperkio, P., Benkő, G., Korppi-Tommola, J., Yartsev, A. P. & Sundström, V. A study of electron transfer in Ru(dcbpy)₂(NCS)₂ sensitized nanocrystalline TiO₂ and SnO₂ films induced by red-wing excitation. *Phys. Chem. Chem. Phys.* 10, 996–1002 (2008).
38. Mahanta, S., Furube, A., Matsuzaki, H., Murakami, T. N. & Matsumoto, H. Electron injection efficiency in Ru-dye sensitized TiO₂ in the presence of room temperature ionic liquid solvents probed by femtosecond transient absorption spectroscopy: effect of varying anions. *J. Phys. Chem. C* 116, 20213–20219 (2012).
39. Teuscher, J. *et al.* Photoinduced Interfacial Electron Injection Dynamics in Dye-Sensitized Solar Cells under Photovoltaic Operating Conditions. *J. Phys. Chem. Lett.* 3, 3786–3790 (2012).
40. Bräm, O., Messina, F., El-Zohry, A. M., Cannizzo, A. & Chergui, M. Polychromatic femtosecond fluorescence studies of metal–polypyridine complexes in solution. *Chem. Phys.* 393, 51–57 (2012).
41. Moser, J.-E. in *Dye-sensitized Solar Cells* (Kalyanasundaram, K.) 403–456 (EPFL Press, 2009).
42. Pelet, S., Moser, J.-E. & Grätzel, M. Cooperative effect of adsorbed cations and iodide on the interception of back electron transfer in the dye sensitization of nanocrystalline TiO₂. *J. Phys. Chem. B* 104, 1791–1795 (2000).
43. Haque, S. A. *et al.* Parameters influencing charge recombination kinetics in dye-sensitized nanocrystalline titanium dioxide films. *J. Phys. Chem. B* 104, 538–547 (2000).
44. Fabregat-Santiago, F. *et al.* The origin of slow electron recombination processes in dye-sensitized solar cells with alumina barrier coatings. *J. Appl. Phys.* 96, 6903 (2004).
45. Christ, C. S., Yu, J., Zhao, X., Palmore, G. T. R. & Wrighton, M. S. Intermolecular and intramolecular excited-state electron transfer involving electrode-confined rhenium carbonyl complexes: toward molecule-based systems for light absorption, charge separation, and optical energy conversion. *Inorg. Chem.* 31, 4439–4440 (1992).
46. Bach, U. *et al.* Charge separation in solid-state dye-sensitized heterojunction solar cells. *J. Am. Chem. Soc.* 121, 7445–7446 (1999).

-
47. Cheng, Z. & Lin, J. Layered organic–inorganic hybrid perovskites: structure, optical properties, film preparation, patterning and templating engineering. *CrystEngComm* 12, 2646–2662 (2010).
48. Mitzi, D. B., Chondroudis, K. & Kagan, C. R. Organic-inorganic electronics. *IBM J. Res. & Dev.* 45, 29–45 (2001).
49. Poglitsch, A. & Weber, D. Dynamic disorder in methylammoniumtrihalogenoplumbates (II) observed by millimeter-wave spectroscopy. *J. Chem. Phys.* 87, 6373–6378 (1987).
50. Kawamura, Y., Mashiyama, H. & Hasebe, K. Structural Study on Cubic-Tetragonal Transition of $\text{CH}_3\text{NH}_3\text{PbI}_3$. *J. Phys. Soc. Jpn.* 71, 1694–1697 (2002).
51. Mitzi, D. B. Templating and structural engineering in organic–inorganic perovskites. *J. Chem. Soc., Dalton Trans.* 1–12 (2000).
52. Knutson, J. L., Martin, J. D. & Mitzi, D. B. Tuning the band gap in hybrid tin iodide perovskite semiconductors using structural templating. *Inorg. Chem.* 44, 4699–4705 (2005).
53. Noh, J. H., Im, S. H., Heo, J. H., Mandal, T. N. & Seok, S. I. Chemical management for colorful, efficient, and stable inorganic-organic hybrid nanostructured solar cells. *Nano. Lett.* 13, 1764–1769 (2013).
54. Borriello, I., Cantele, G. & Ninno, D. Ab initio investigation of hybrid organic-inorganic perovskites based on tin halides. *Phys. Rev. B* 77, 235214 (2008).
55. Kim, H.-S. *et al.* Lead iodide perovskite sensitized all-solid-state submicron thin film mesoscopic solar cell with efficiency exceeding 9%. *Sci Rep* 2, 591 (2012).
56. Schulz, P. *et al.* Interface energetics in organo-metal halide perovskite-based photovoltaic cells. *Energy Environ. Sci.* (2014). doi:10.1039/C4EE00168K
57. Papavassiliou, G. C. Three- and low-dimensional inorganic semiconductors. *Prog. Solid State Ch.* 25, 125–270 (1997).
58. Papavassiliou, G. C., Mousdis, G. A., Koutselas, I. B. & Papaioannou, G. J. Excitonic bands in the photoconductivity spectra of some organic-inorganic hybrid compounds based on metal halide units. *Int. J. Mod. Phys. B* 15, 3727–3731 (2001).
59. Tanaka, K. *et al.* Comparative study on the excitons in lead-halide-based perovskite-type crystals $\text{CH}_3\text{NH}_3\text{PbBr}_3$ $\text{CH}_3\text{NH}_3\text{PbI}_3$. *Solid State Commun.* 127, 619–623 (2003).
60. Innocenzo, V. D. R. *et al.* Excitons versus free charges in organo-lead tri-halide perovskites. *Nat. Commun.* 5, 1–6 (2014).

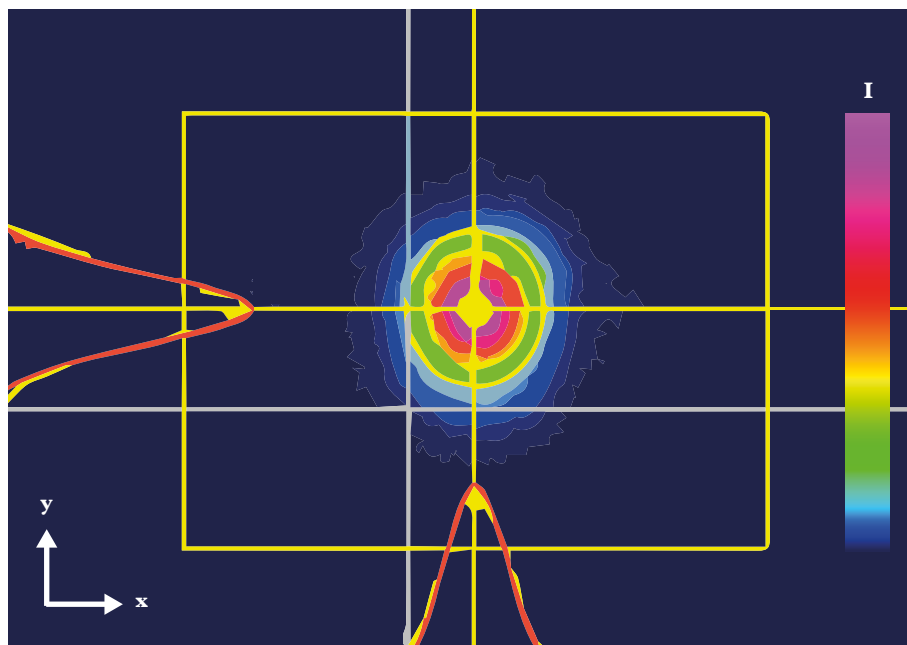
61. Yamada, K., Kawaguchi, H., Matsui, T., Okuda, T. & Ichiba, S. Structural phase transition and electrical conductivity of the perovskite $\text{CH}_3\text{NH}_3\text{Sn}_{1-x}\text{Pb}_x\text{Br}_3$ and CsSnBr_3 63, 2521–2525 (1990).
62. Takahashi, Y. *et al.* Charge-transport in tin-iodide perovskite $\text{CH}_3\text{NH}_3\text{SnI}_3$: origin of high conductivity. *Dalton Trans.* 40, 5563 (2011).
63. Mitzi, D. B., Feild, C. A., Harrison, W. T. A. & Guloy, A. M. Conducting tin halides with a layered organic-based perovskite structure. *Nature* 369, 467–469 (1994).
64. Hirasawa, M., Ishihara, T., Goto, T., Uchida, K. & Miura, N. Magnetoabsorption of the lowest exciton in perovskite-type compound $(\text{CH}_3\text{NH}_3)\text{PbI}_3$. *Phys. B* 201, 427–430 (1994).
65. Pellet, N. *et al.* Mixed-Organic-Cation Perovskite Photovoltaics for Enhanced Solar-Light Harvesting. *Angew. Chem. Int. Ed. (English)* 53, 3151–3157 (2014).
66. Kojima, A., Teshima, K., Shirai, Y. & Miyasaka, T. Organometal halide perovskites as visible-light sensitizers for photovoltaic cells. *J. Am. Chem. Soc.* 131, 6050–6051 (2009).
67. Im, J.-H. H., Lee, C.-R., Lee, J.-W., Park, S.-W. & Park, N.-G. 6.5% efficient perovskite quantum-dot-sensitized solar cell. *Nanoscale* 3, 4088–4093 (2011).
68. Lee, M. M., Teuscher, J., Miyasaka, T., Murakami, T. N. & Snaith, H. J. Efficient hybrid solar cells based on meso-superstructured organometal halide perovskites. *Science* 338, 643–647 (2012).
69. Heo, J. H. *et al.* Efficient inorganic-organic hybrid heterojunction solar cells containing perovskite compound and polymeric hole conductors. *Nature Photon.* 7, 486–491 (2013).
70. Bi, D., Yang, L., Boschloo, G., Hagfeldt, A. & Johansson, E. M. J. Effect of different hole transport materials on recombination in $\text{CH}_3\text{NH}_3\text{PbI}_3$ perovskite-sensitized mesoscopic solar cells. *J. Phys. Chem. Lett.* 4, 1532–1536 (2013).
71. Bi, D. *et al.* Efficient and stable $\text{CH}_3\text{NH}_3\text{PbI}_3$ -sensitized ZnO nanorod array solid-state solar cells. *Nanoscale* (2013). doi:10.1039/c3nr01542d
72. Bi, D., Moon, S.-J., Häggman, L., Boschloo, G. & Yang, L. Using a two-step deposition technique to prepare perovskite $(\text{CH}_3\text{NH}_3\text{PbI}_3)$ for thin film solar cells based on ZrO_2 and TiO_2 mesostructures. *RSC Adv.* (2013).
73. Burschka, J. *et al.* Sequential deposition as a route to high-performance perovskite-sensitized solar cells. *Nature* 499, 316–319 (2013).

-
74. NREL Chart. *www.nrel.gov* (2014). at <<http://www.nrel.gov/ncpv/>>
75. Docampo, P., Ball, J. M., Darwich, M., Eperon, G. E. & Snaith, H. J. Efficient organometal trihalide perovskite planar-heterojunction solar cells on flexible polymer substrates. *Nat. Commun.* 4, 2761 (2013).
76. Malinkiewicz, O. *et al.* Perovskite solar cells employing organic charge-transport layers. *Nature* 8, 128–132 (2013).
77. Ball, J. M., Lee, M. M., Hey, A. & Snaith, H. J. Low-temperature processed meso-structured to thin-film perovskite solar cells. *Energy Environ. Sci.* 6, 1739–1743 (2013).
78. Liu, M., Johnston, M. B. & Snaith, H. J. Efficient planar heterojunction perovskite solar cells by vapour deposition. *Nature* 501, 395–398 (2013).
79. Etgar, L. *et al.* Mesoscopic $\text{CH}_3\text{NH}_3\text{PbI}_3/\text{TiO}_2$ heterojunction solar cells. *J. Am. Chem. Soc.* 134, 17396–17399 (2012).
80. Abu Laban, W. & Etgar, L. Depleted hole conductor-free lead halide iodide heterojunction solar cells. *Energy Environ. Sci.* 6, 3249–3253 (2013).
81. Edri, E. *et al.* Elucidating the charge carrier separation and working mechanism of $\text{CH}_3\text{NH}_3\text{PbI}_{3-x}\text{Cl}_x$ perovskite solar cells. *Nat. Commun.* 5, 3461 (2014).
82. Stranks, S. D. *et al.* Electron-hole diffusion lengths exceeding 1 micrometer in an organometal trihalide perovskite absorber. *Science* 342, 341–344 (2013).
83. Xing, G. *et al.* Long-Range Balanced Electron- and Hole-Transport Lengths in Organic-Inorganic $\text{CH}_3\text{NH}_3\text{PbI}_3$. *Science* 342, 344–347 (2013).
84. Edri, E. *et al.* Why lead methylammonium tri-iodide perovskite-based solar cells require a mesoporous electron transporting scaffold (but not necessarily a hole conductor). *Nano. Lett.* 140131132402004 (2014). doi:10.1021/nl404454h
85. Giorgi, G., Fujisawa, J.-I., Segawa, H. & Yamashita, K. Small Photocarrier Effective Masses Featuring Ambipolar Transport in Methylammonium Lead Iodide Perovskite: A Density Functional Analysis. *J. Phys. Chem. Lett.* 4, 4213–4216 (2013).
86. Yin, W. J., Shi, T. & Yan, Y. Unusual defect physics in $\text{CH}_3\text{NH}_3\text{PbI}_3$ perovskite solar cell absorber. *Appl. Phys. Lett.* (2014).
87. Colella, S., Mosconi, E., Fedeli, P. & Listorti, A. $\text{MAPbI}_{3-x}\text{Cl}_x$ Mixed Halide Perovskite for Hybrid Solar Cells: The Role of Chloride as Dopant on the Transport and Structural Properties. *Chem. Mater.* (2013).

88. Kim, H.-S. *et al.* Mechanism of carrier accumulation in perovskite thin-absorber solar cells. *Nat. Commun.* 4, 2242 (2013).
89. Hodes, G. Perovskite-Based Solar Cells. *Science* 342, 317–318 (2013).

CHAPTER 2

Experimental part



2.1 Flash Photolysis

2.1.1 Fundamentals of the technique

Flash Photolysis (also known as nanosecond transient absorption) is the simplest form of pump-probe technique and was developed shortly before the first lasers. Eigen, Norrish and Porter won the 1967 Nobel Prize in Chemistry for the invention of this technique and its application on the study of fast chemical reactions “*effected by disturbing the equilibrium by means of very short pulses of energy*”.¹

The basic principle relies on short laser pump pulses exciting a sample, while a continuous light source such as a Xenon lamp probes the response of the sample to the excitation event (Figure 2.1). It is then possible to determine the difference in absorbance between the species that are created following the laser pulse and the ground state species. The difference in absorbance, termed ΔA , is given by:

$$\Delta A = A_{\text{pump}} - A_{\text{no pump}} = -\log\left(\frac{I_{T^*}}{I_0}\right) + \log\left(\frac{I_T}{I_0}\right) = -\log\left(\frac{I_{T^*}}{I_T}\right) \quad (2.1)$$

Where A_{pump} corresponds to the absorbance when the pump illuminates the sample, while $A_{\text{no pump}}$ corresponds to the absorbance without any pump. I_{T^*} and I_T are respectively the fraction of probe light transmitted through an excited and a non-excited sample, while I_0 is the probe light that illuminates the sample. Another simple way to express (2.1) is:

$$\Delta A = A_{\text{pump}} - A_{\text{no pump}} = -\log\left(\frac{\Delta I + I_T}{I_T}\right) \quad (2.2)$$

With ΔI being the transient perturbation in the transmitted intensity caused by the pump.

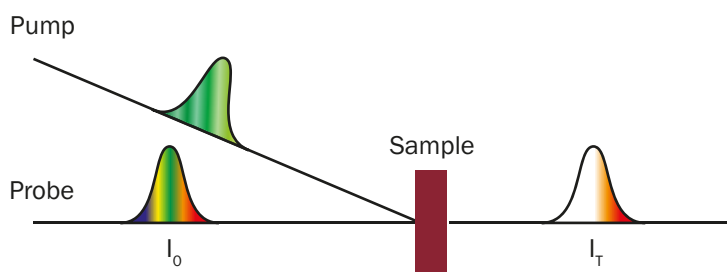


Figure 2.1 Schematic view of a pump-probe experiment

The incoming probe light I_0 on the sample can be partially absorbed by the sample, resulting in the transmitted component through the sample I_T . The incoming pump will excite the sample, generating species with different absorption spectra than the ground state.

Thus, a positive ΔA indicates a transient species with an absorbance greater than the ground state species, while a negative ΔA is often the sign of depletion of the ground state, referred to as ground state bleaching (GSB). In femtosecond experiments, a negative ΔA could also correspond to a stimulated emission process. In this case the stimulation occurs through the interaction of the laser probe beam with the excited states of the sample. The stimulated emission beam is coherent with the probe beam.

2.1.2 Excitation source

The excitation source is provided by a nanosecond Nd-YAG Q-switched laser (Continuum Powerlite-7030) with a frequency-tripled output (355 nm) and 20 Hz repetition rate. The UV output beam is used to pump a broadband optical parametric oscillator (OPO, GWU-355).

An OPO uses the concept of laser resonator, but where the optical gain is based on optical parametric amplification rather than on stimulated emission. Optical parametric amplification is obtained when a non-linear crystal is pumped by a high intensity laser beam. The nonlinear crystal can then split one incoming photon into two photons (signal and idler), and the sum of the signal and the idler energies equals the one of the original photon.² A schematic view is presented in Figure 2.2. In the oscillator, the signal beam is oscillating in a cavity with resonator mirrors, passing many times through the pumped non-linear crystal and thus further amplifying the signal output. The idler is usually ejected by one of the resonator mirrors. For parametric amplification to occur, phase matching conditions must be fulfilled. This means that the interacting waves, pump, signal and idler, must be in a constructive phase relationship, and is practically achieved by tuning the angle of the crystal and the distance between the waves.

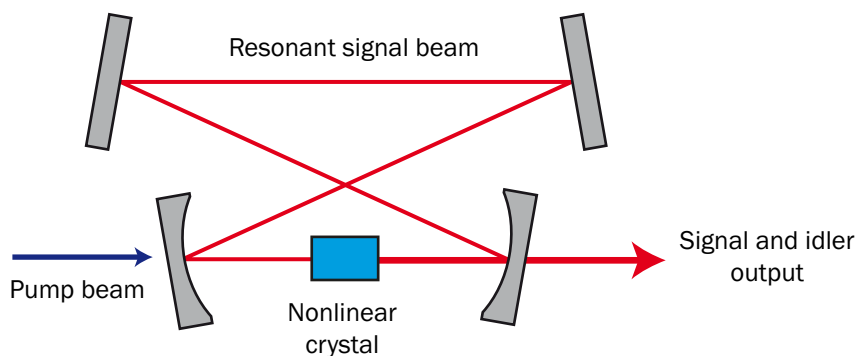


Figure 2.2 Schematic view of an optical parametric oscillator

The pump beam is injected through a dichroic mirror. The signal beam is resonant in the cavity, whereas the idler is usually ejected by at least of the resonator mirrors.

The OPO allows tuning the excitation pulse to the desired wavelength, which is chosen by rotation of the crystal and selection of the appropriate cavity mirrors. The laser beam is then usually attenuated to a fluence smaller than $80 \mu\text{J}/\text{cm}^2$ by the use of neutral density filters. The sample is set at a 60° angle to the excitation laser beam to avoid light scattering of the pump beam into optics for the detection. A scheme of the whole setup is presented in Figure 2.3.

2.1.3 Detection

The continuous wave (CW) probe light from a Xe arc lamp is passed through various filters to select the wavelength, the sample, and a monochromator before being detected (Figure 2.3). Detection in the visible (400-750 nm) is performed with a fast photomultiplier tube (R9910, Hamamatsu) connected to a high voltage source (750 V) allowing conversion of photons into electrons. The obtained current is thus monitored by an oscilloscope (DPO 7204, Tektronix). Temporal resolutions up to $1 \mu\text{s}$ can be achieved with $1 \text{ M}\Omega$ load on the oscilloscope, while much faster signals (down to 50 ns) can be monitored with 50Ω load on the oscilloscope. Similarly, detection in the IR (800-1800 nm) is provided by an InGaAs photodiode with $1 \text{ k}\Omega$ load (SM05PD5A, Thorlabs). The temporal resolution is limited by the diode response, which is $1.2 \mu\text{s}$. Averaging over at least 2,000 laser shots is usually necessary to obtain a satisfactory signal-to-noise ratio. Unless important fluctuations of the incoming probe beam were observed, measurements were operated in direct current (DC) mode.

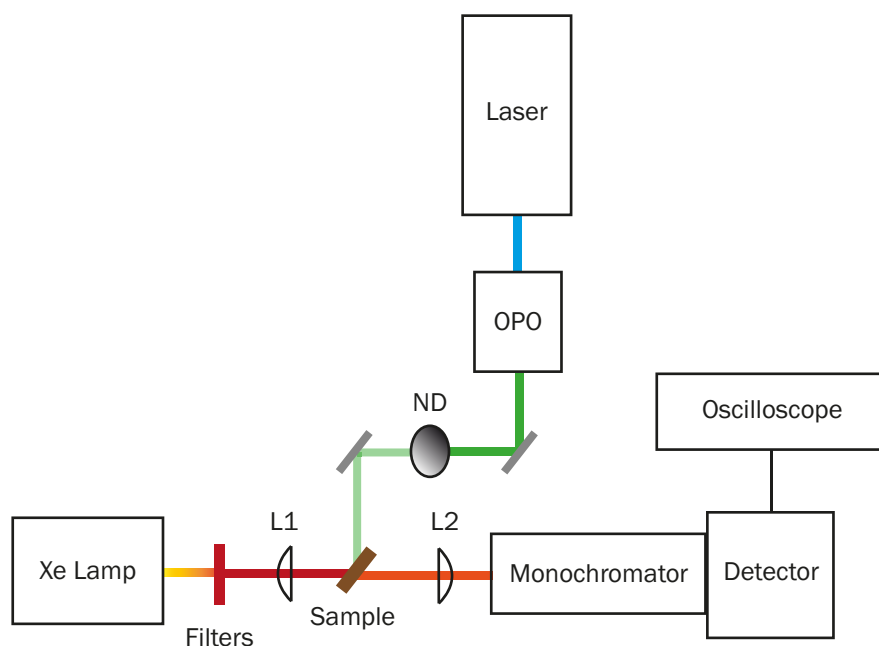


Figure 2.3 Nanosecond laser flash photolysis setup

A Nd:YAG laser pumps an Optical Parametric Oscillator (OPO) to obtain the desired wavelength. The beam is filtered by neutral density (ND) filters and used as the pump of the experiment. The probe light produced by a Xe arc lamp passes through various filters to select the desired probe wavelength. The probe beam is focused on the sample with a first plano-convex lens L1 on the sample, and then collimated by a second plano-convex lens L2 to the slit of the monochromator in order to be detected by the PMT or the diode connected to an oscilloscope. The oscilloscope is triggered synchronously to the pulsed laser by a fast photodiode.

2.2 Femtosecond transient absorption spectroscopy

2.2.1 Fundamentals of the technique

Femtosecond transient absorption spectroscopy is the ultrafast version of the flash photolysis technique. As signals faster than the nanosecond are difficult to resolve electronically, like with an oscilloscope in the previous case, a different scheme must be implemented. This is based on the properties of optical delays, where the time scale is set by the physical delay between a pump and a probe pulse travelling different distances. Indeed, since the light in air travels 1 meter in 3.33 ns, the desired time interval can be selected by adjusting the travelling distance with mirrors on a moving translation stage.

2.2.2 Laser

The femtosecond setup was mainly built during S. Pellet's thesis³ but has undergone many modifications since.^{4,5} The laser source is provided by a CPA-2001 from Clark-MXR.

The laser is based on a Ti:Sa medium pumped with the frequency-doubled output of a Nd-YAG laser (532 nm). The Nd-YAG is pumped with an arc lamp. The Ti:Sa seed is provided by a frequency-doubled Er-doped fiber laser (775 nm). The Er-doped fiber is itself diode-pumped and constitutes the oscillator of the system, which produces very short pulses.

The system relies on the technique of Chirped Pulse Amplification (CPA), where the seed pulse is first stretched in the time (and frequency) domain with a pair of dispersing diffraction grating to decrease the peak power.⁶ After successful amplification in the Ti:Sa laser cavity, the pulse is then compressed back with diffraction gratings to obtain a short amplified pulse. The 775 nm pulses are extracted from the cavity with a frequency of 1 kHz and a duration of approximately 150 fs. The average energy per pulse is 950 μ J.

2.2.3 NOPA

Transient absorption spectroscopy requires wavelength tunability. This is in practice achieved by the use of a Non-Linear Optical Parametric Amplifier (NOPA). The model used in our setup is based on a scheme developed by the group of Prof. Riedle.⁷ A part of the output of the CPA laser (150 to 200 μ J) is sent to each of the NOPAs. A NOPA is divided in two stages in order to get a satisfactory output power. In the first stage, a very small fraction of the beam is used to generate a White Light Continuum (WLC) through a sapphire plate.

White Light Generation is one among the many non-linear effects. Indeed, a strong laser pulse focused on a non-linear medium, such as a sapphire plate, will change the refractive index of the medium, which will oscillate with time. Moreover, since the different wavelengths of a broad short pulse travel at different speeds in the dispersive medium, and in this case the refractive index is changing in time, this will lead to a broadening of the different wavelengths generating what can be observed as a superbroad continuum. This effect is also known as self-phase modulation.^{2,8}

The remaining beam is frequency-doubled on a non-linear beta-baryum borate (BBO) crystal (387 nm), and then part of this beam as well as the WLC are then focused on another non-linear BBO crystal, where the desired wavelength can be obtained by tuning the angle of the crystal and the relative distance between the pump beam and the WLC seed in order to obtain the phase-matching conditions. This configuration gives the possibility to obtain wavelengths in the 450 to 1500 nm range. The region between 700

and 900 nm cannot be covered in this simple configuration because of the instability around the fundamental wavelength.

The output beam from the first stage can then further be amplified (typically 6 times) in a second BBO crystal, together with the remaining 387 nm beam. The energy of the outgoing pulses is then in the range of 6 to 12 μJ depending on the wavelength. The wavelength is monitored with a dual-channel spectrometer (S2000, Ocean Optics) coupled with an optical fiber.

In order to cover the range between 700 and 900 nm, an additional WLC generation stage can be inserted. In the first stage, one has to generate an IR wavelength between 1000 to 1100 nm, and then use this output to generate a WLC through a sapphire plate that is now far away from the fundamental wavelength. The resulting continuum can then be used in the second stage to generate the desired wavelength. In this work, 840 nm output wavelength was usually obtained with typical energies from 1 to 2 μJ .

In some experiments, an automatized TOPAS (Travelling Wave Optical Parametric Amplification of Superfluorescence, Light Conversion) was used to generate IR wavelengths with higher power.⁹

2.2.4 Pulse compression

Output pulses from the NOPA are slightly stretched, up to 200 fs. This phenomenon of group velocity dispersion (GVD) is due to the fact that the different frequency components of a pulse will travel at different velocities.² Thus, compression is needed to increase the temporal resolution of the pulse. This is achieved using a pair of SF10 glass prisms, where the GVD can be corrected, as shown in Figure 2.4. A first prism is used to refract the different wavelength components to different angles. Then a second prism is placed at a distance that will determine the compression and this will refract all components again. The second prism should be oriented in the reverse direction but with its axis parallel to the one of the first prism. The components will propagate in parallel directions in that prism, and because of the different path lengths, red wavelengths will travel more glass material and be slowed down with respect to blue ones. Then a second path after reflection on a mirror will allow compensating for the spatial dispersion and recollimate the beam. The angle of the incident beam on the prisms should be adjusted to the Brewster angle to minimize the reflection of the p-polarized laser beam.

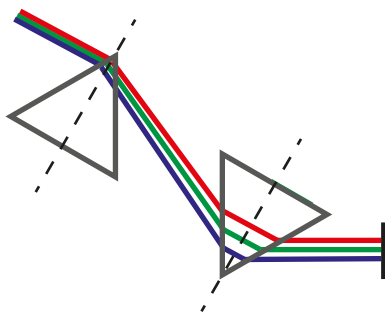


Figure 2.4 Scheme of prism alignment

The incoming beam is refracted at different angles with the first prism. A second prism refracts again the components, which will propagate in parallel directions in that prism. Because of the different path lengths, red wavelengths will travel more glass material and will be slowed down with respect to blue ones. A mirror is used to create a second path in the prisms and allows compensation for spatial dispersion of the beams.

The desired pulse compression is obtained by varying the distance between the prisms and measuring the pulse width with a portable autocorrelator (pulseCheck, APE). A typical output pulse length is in the order of 50 fs.

The autocorrelation technique consists in splitting the beam in two copies with a beam splitter, making part of the beam travel a tunable distance and then having the two parts recombining in a non-linear medium, where sum-frequency generation occurs and the corresponding sum-frequency wavelength can be detected.

2.2.5 Probe schemes

Two different probe schemes were mainly used in this thesis, both being in transmission mode. The first one is based on a monochromatic probe; the second employed a WLC probe. In both cases, the sample is traversed by the probe beam focalized on the sample with a parabolic mirror, in order to avoid further temporal stretching of the probe beam. The excitation beam is adjusted with a small angle with respect to the probe beam and the polarization is set at the magic angle (54.7°) with respect to the polarization of the probe light by use of a $\lambda/2$ waveplate. This ensures an isotropic excitation of the sample. Either the pump or the probe beam in the case of monochromatic pump-probe can be delayed by the use of a motorized translation stage (M531 PD, Physik Instrument) equipped with a retro-reflector (49-668, Edmund Optics). In both cases, a chopper on the pump beam at 500 Hz enables to distinguish a transient signal (with pump) from a signal without pump, as the probe is running at 1 kHz.

The diameter of the pump beam is monitored with a beam profiler (BC 106-Vis, Thorlabs) and the energy is measured with an energy meter (Vega, Ophir) and regulated with neutral density filters.

2.2.6 Monochromatic Pump-probe

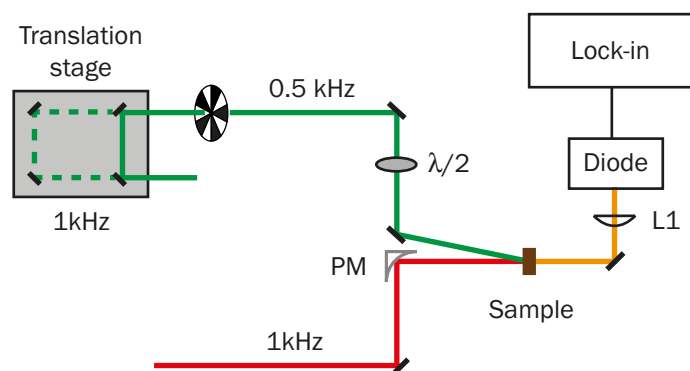


Figure 2.5 Schematic view of the monochromatic pump-probe detection

The pump beam is delayed by a retroreflector mounted on a motorized translation stage. The beam is then chopped by a rotating wheel at 500 Hz and directed on the sample. The polarization of the beam is adjusted to the magic angle with respect to the polarization of the probe beam with a half-wave plate. The probe beam (1 kHz) is focused on the sample using a parabolic mirror with a 20 cm focal length (PM). After transmission through the sample the probe beam is collimated through a lens (L1) and sent to the detector. The diode is connected to a lock-in amplifier referenced to the chopper.

Monochromatic pump-probe experiments were conducted in this work to measure in the 840-860 nm region before the WLC probe could be extended to the IR region. The schematic view of this type of detection is presented in Figure 2.5. One NOPA is used to generate the pump while a second, symmetrical NOPA is used for the probe. Both beams are compressed through a prism. Either the pump or the probe beam could be delayed by the use of a motorized translation stage. The detection is done using a diode (Nirvana, New Focus, model 2007 and 2017 respectively for visible and NIR) connected to a lock-in amplifier (SR-830, Stanford Research) referenced to the chopper (500 Hz).

The technique of lock-in amplification gives an easy way to extract very small AC signals from a noisy background.¹⁰ The lock-in can basically look at the signal at one specific reference frequency and phase. Noise signals and any other different frequency signals are rejected and do not interfere with the measurement. By “locking” on the frequency of our experiment (500 Hz), the lock-in extracts two quantities, X and Y, X being the “in-phase” signal, while Y gives the “out of phase” component. Y is usually set to zero by adjusting the phase so that X is directly proportional to the photovoltage (+/- sign). For determining the change in absorbance, it is also necessary to know the transmission through the sample without any excitation, and this is obtained by measuring the photovoltage when the pump is blocked and with the lock-in referenced to 1 kHz. The sign (positive or negative) of the absorbance can be difficult to obtain especially if the phases are changed between the two measurements. The safest way is then to measure a known sample to determine

the sense of the signal. Thus, by taking the equation (2.2), the change in absorbance can be written:

$$\Delta A = -\log\left(\frac{\Delta I + I_T}{I_T}\right) = -\log\left(\frac{X_{500\text{Hz}} + X_{1000\text{Hz}}}{X_{1000\text{Hz}}}\right) \quad (2.3)$$

Where $X_{500\text{Hz}}$ is photovoltage associated to the amplitude of the perturbation signal and $X_{1000\text{Hz}}$ corresponds to the photovoltage associated to the intensity transmitted through the non-excited sample.

The time resolution, or instrument response function (IRF) of the setup is measured by estimating the cross-correlation of the pump and probe pulses at the sample position by the Kerr gating technique.

The Kerr effect is based on the transient anisotropy that can be created in a material upon the action of an electric field, i.e, when a strong laser pulse impinges in a material, it can create an electric field in the direction of its polarization, thus rendering the material anisotropic in that specific direction. The probe and pulse beams have a polarization set at 45° with respect to each other in order to maximise the non-linear Kerr effect, and are focused onto a Kerr medium, which is either a SF10 window or a glass microscopic slide for measurements on solid state samples, alternatively a 1 mm cuvette filled with solvent for studies in solution. The probe is then blocked by a Glan-Thompson polarizer. When both pulses are temporally overlapped, the birefringence induced by the pump in the medium rotates the polarization of the probe, which is able to go through the polarizer in the detector.

Data obtained from monochromatic pump-probe experiments are fitted with an analytical convolution of a Gaussian instrument response function and n exponentials (decay or rises) as described in the thesis of J. Teuscher.⁵

2.2.7 White-light continuum (WLC) probe

A one-stage WLC setup has been built in collaboration with N. Banerji and J. Risse-De Jonghe to provide an alternative to the two-stages WLC NOPA built in the thesis of J. Teuscher.⁵ The initial goal of this operation was to obtain a more stable WL, even though less intense. The generation of the one-stage WLC was further improved by changing the sapphire plate for a CaF_2 crystal that gives a broader spectral range, with extended UV and IR part, as well as an increase in stability. The basic principle of WLC

generation has been introduced in section 2.2.3 but a more detailed description can be found elsewhere.⁸

WLC generation

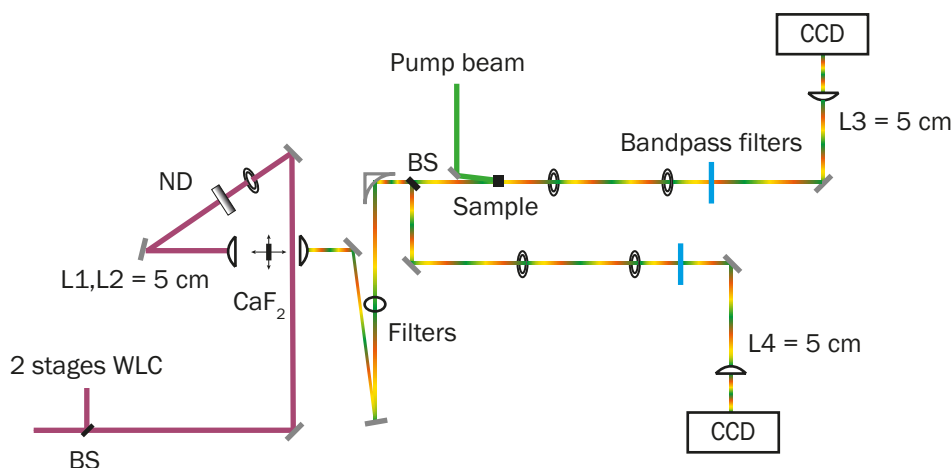


Figure 2.6 Scheme of WLC generation

Part of the 775 nm beam from the laser (20 μJ) is collimated by a first lens L1 on a CaF_2 crystal continuously moved by a function generator. The intensity of the incoming beam is controlled by an iris and a neutral density filter (ND). The WLC output is collected through a second lens L2. The WLC beam traverses several optical elements depending on the spectral region (visible or IR) and is collected by a parabolic mirror. Part of the beam is sent to the reference CCD camera, while the rest is focused onto the sample and then collected by the signal CCD camera. The beam is collimated in the respective cameras using two lenses L3 and L4, mounted on a three-axis translation stage.

A schematic picture of WLC generation is provided in Figure 2.6. From the main laser source, about 450 μJ at 775 nm are used to pump the two-stages white-light NOPA. The incoming energy needed for the one-stage white-light NOPA is around 20 μJ . The beam passes through an iris and a variable ND filter and is directed onto a 5 mm CaF_2 crystal via a 5 cm focal length lens. The crystal is mounted on a 2-axis translation stage, thus allowing for fine-tuning of its position with respect to the beam (x and y direction). The CaF_2 is continuously moved on the z-direction by a vibration generator (B2-2185.00, djb microtech ltd) controlled by a function generator (A2-2502.50, djb microtech ltd) as its damage threshold is lower than for a sapphire plate. The typical spectrum of the generated WLC is shown in Figure 2.7.

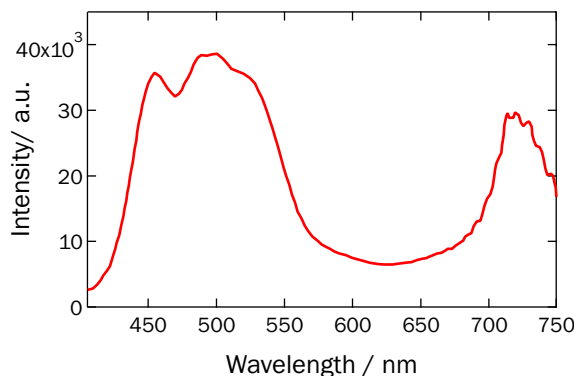


Figure 2.7 Typical spectrum for the WLC generated by a CaF₂ crystal

The intensity is given in arbitrary units and only the visible part (400-750 nm) is shown here; oscillations are more pronounced close to the fundamental (775 nm).

The energy control of the incident beam by the ND filter and the iris enables a stable and broad WLC spectrum, which is collimated by a 5 cm focal length lens. The beam passes through a wire grid polarizer to discard any unwanted polarization residuals and is directed to a parabolic mirror. The beam is directed to the detection part using the same parabolic mirrors as for the monochromatic pump-probe experiment. Half of the WLC is then sent to the reference camera path by reflection on a 1 mm OD 0.5 filter (“reference” beam), while the transmitted part (“signal” beam) is directed on the sample. Both beams are attenuated and directed in their respective charge-coupled device (CCD) cameras, reference and signal, with a three-axis 5 cm focal length achromatic lens.

Detection

The signal and reference beams are detected with two spectrographs (Princeton instruments, SpectraPro 2150) equipped with a 512×58 pixels back-thinned CCD (Hamamatsu S7030-0906) and assembled by Entwicklungsbüro Stresing, Berlin.

The spectrographs have two gratings: 500 nm blaze and 800 nm blaze, controlled by the software Mono. The first one enables the analysis of 350-800 nm WLC (visible region) and requires the implementation of 350-710 nm band-pass filters to discard the excess fundamental at 775 nm. The second grating enables the analysis of 800-1200 nm (IR region) with the implementation of 750 nm and/or 850 nm long pass filters. The wire-grid polarizer is optimized routinely and usually 90° rotation distinguishes visible from infrared WLC. Careful calibration of the spectrographs is achieved by placing several interferential filters in the common WLC beam and by controlling the position of the gratings.

Data acquisition system

The transmitted probe intensity acquisition is done shot-by-shot. The reference beam enables to account for white-light fluctuations. Typically, 3000 shots are averaged in order to obtain a good signal-to-noise ratio. We distinguish I_{T^*} , the intensity transmitted in the signal camera with the pump; I_T , the intensity transmitted in the signal camera without the pump, I_{R^*} , the intensity transmitted in the reference camera with the pump and I_R , the intensity transmitted in the reference camera without the pump. The absorbance change is then calculated via the following equation:

$$\Delta A = -\log\left(\frac{I_{T^*} I_{R^*}}{I_T I_R}\right) \quad (2.4)$$

The dark counts on the cameras are acquired before each measurement and subtracted from the transmitted light intensity for each camera.

Cross-correlation by Kerr gating

The principle is identical to what is described in section 2.2.6 and described in detail in a work by Yamaguchi and Hamaguchi.¹¹ The change in polarization of the probe upon pump action on a non-linear medium can be obtained, and detected by the CCD camera. The WLC has a broad spectral width and therefore presents large group velocity dispersion, called chirp. While passing a dispersive medium, longer wavelengths travel in front whereas smaller wavelengths are slower. This results in the blue being seen at time zero while the red has already travelled for a few picoseconds, as shown in Figure 2.8. This configuration of the setup has a typical cross-correlation (corresponding to its instrument response function, IRF) of the order of 50 fs for solid state samples, and about 100-200 fs for liquid samples.

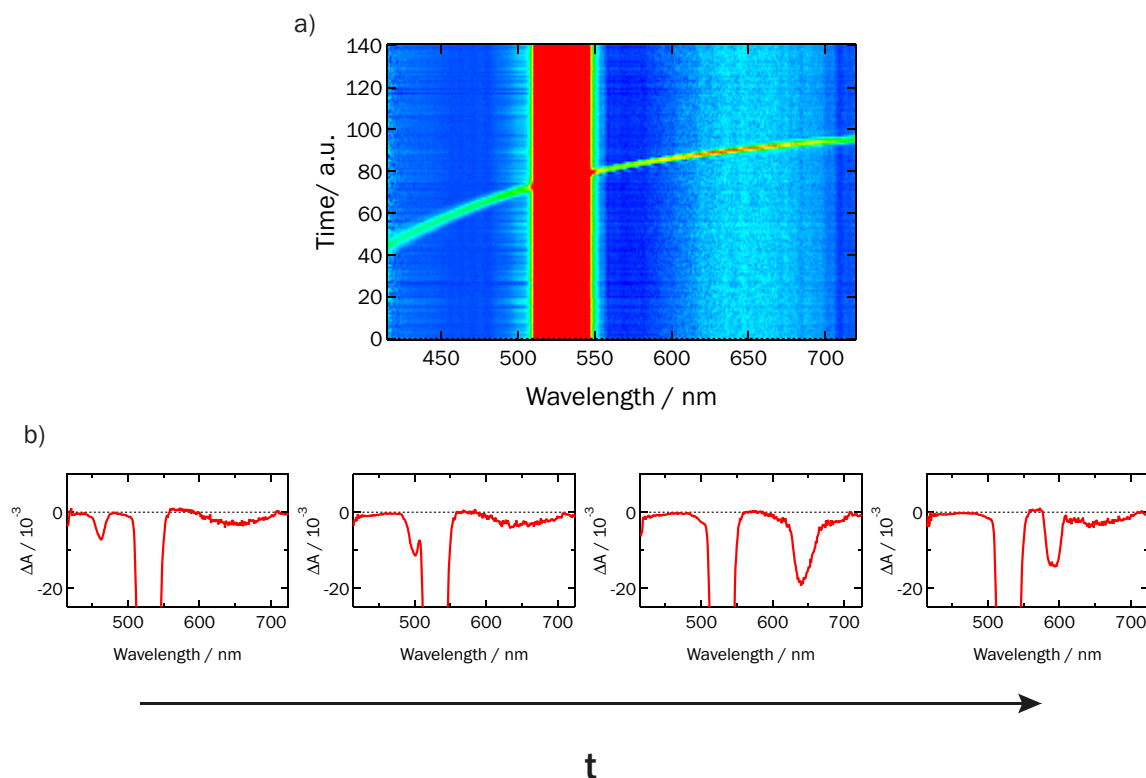


Figure 2.8 Chirp propagation

a) Graphical view of the temporal propagation of the different wavelengths. The red wavelengths are ahead of the blue wavelengths. b) Change in absorbance on the entire wavelength spectrum detected by the Kerr gating technique. One can see the propagation of the chirp at different time delays after excitation. Due to the chirp of the white light the temporal overlap between pump and probe – or time zero – is wavelength dependent. The temporal overlap of a certain component of the continuum with the pump pulse results in a coherent artifact.

Labview integration

The Labview software (National Instruments) is used for the data acquisition. The program was written by F. Gummy, J. Teuscher and N. Banerji. A schematic view of the synchronization of the laser trigger, the pump chopper and the record of the CCD cameras is shown in Figure 2.9. The laser trigger (Trig Laser In) running at 1 kHz is amplified and converted in a square signal (Trig Laser Out). The chopper is set to 500 Hz. A home-built chopper plate with a transmittive photomicrosensor has been designed. The transmittive photomicrosensor determines the on/off position by detecting when the pump beam is or is not on the photomicrosensor. The slight shift between the aperture for the sensor and the aperture for the laser beam is able to account for the jitter. At first, the Labview software starts a measurement (Trig Enable) and controls the synchronization of the camera with the laser trigger (Readout Camera synchronizes with Trig Laser Out). As soon as this is done, two on/off events (4 ms) are taken. The last event determines the order “on” or “off” of the events; this allows determining then if the event must be labeled

with “pump” or “no pump”. Each event is constituted by 512 pixels, which are then averaged at the end of the acquisition time. Typically 3000 shots, meaning 1500 on/off events are taken during a measurement.

The Labview software enables the real-time lecture of the raw WLC spectrum in both signal and reference cameras, as well as the calculated transient spectra averaged over a defined number of shots. The linear dependence between pixel and wavelength on the grating is manually calibrated with the use of interferential filters. A background spectrum is acquired before each measurement in order to account for the dark counts. The chopper wheel position is routinely checked, as it is possible to distinguish between on and off events in the signal camera.

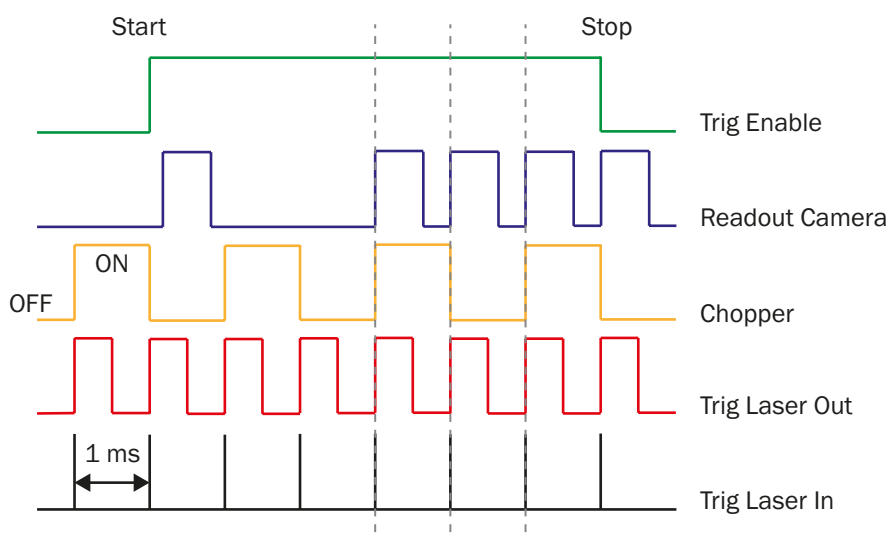


Figure 2.9 Synchronization of laser and cameras

The laser trigger (laser in) running at 1 kHz is amplified and converted in a square signal (laser out). The chopper is set to 500 Hz. The Labview software starts a measurement (trig enable). This allows the camera synchronizing with the laser trigger (readout camera). The first acquisitions before the synchronization are discarded.

Data treatment

A Matlab procedure developed by N. Banerji has been implemented in order to correct for the group velocity dispersion and extract the corrected dynamics at different wavelengths, as well as the spectral profiles at different time delays. The chirp mathematical correction is routinely done for short time scales (typically less than 50 ps).

The Kerr effect manifests as a transient absorbance change that can be approximated by a Gaussian function for each of the different wavelengths. The chirp mathematical correction is performed by fitting every wavelength component by a Gaussian function,

the width of each Gaussian providing the instrument response for each wavelength. The wavefront of all these Gaussian profiles can then be fitted with a monoexponential function as a function of time. Thus, the time zero for every wavelength is extracted from this function.

The Matlab routine allows chirp correction but also subtraction of the background spectra (i.e. noise) from the data. Typically, 20 to 30 spectra acquired before time zero are subtracted from the measurement in order to account for the spectral noise and for the pump beam up to a certain extent. Then, the corrected dynamics for different wavelengths and the spectral profiles at different time delays can be extracted from their initial matrix data file as data columns that are then treated separately in Igor Pro.

In order to disentangle various photophysical processes occurring on the same time scale, a global analysis can be run. For this, a multiexponential fit of the dynamics at different wavelengths is performed:

$$\Delta A = A_1 e^{\frac{-t}{\tau_1}} + A_2 e^{\frac{-t}{\tau_2}} + A_3 e^{\frac{-t}{\tau_3}} \quad (2.5)$$

Typically, two or three exponentials are needed to fit correctly the dynamics taken every 10 nm. This global fit enables to construct an associated spectra displaying the amplitudes, A_1 , A_2 and A_3 of the transient signal related to each time component τ_1 , τ_2 , and τ_3 , as a function of the wavelength.

2.3 Samples preparation

Details of sample preparation are given in each chapter. Samples for transient absorption spectroscopy have been prepared without any conductive glass or metal electrode in order to maximize the transmission through the sample. This configuration is chosen in order to be as close as possible to complete solar cells, but still keeping the possibility to measure the samples in transmission mode.

In the case of dye-based cells, TiO_2 is directly deposited on microscope glass slides, sensitized and then successively impregnated with the hole transport material. In some experiments, the samples were sealed with a thin microscopic glass and Surlyn[®]. In the case of perovskite-based cells, TiO_2 is also directly deposited on microscope glass slides, and then perovskite is deposited either through a single-step deposition method or a sequential method (cf. Chapter 5). The sample is finally impregnated with the hole

transport material. To avoid contact with ambient air the samples were measured in a sealed argon cell, unless otherwise specified.

2.4 References

1. The Nobel Prize in Chemistry 1967 *Nobelprize.org*. Nobel Media AB 2013. 1–2 (2014).
2. Rullière, C. *Femtosecond laser pulses: principles and experiments*. (Springer-Verlag, 1998).
3. Pelet, S. Femtosecond dynamics of electron transfer in the photosensitization of wide band gap semiconductors - EPFL Thesis n°2626. 1–140 (2005).
4. Wenger, B. Effect of Electronic and Nuclear Factors on the Dynamics of Dye-to-Semiconductor Electron Transfer - EPFL Thesis n°3447. 1–184 (2006).
5. Teuscher, J. Dynamics of electron transfer processes at the surface of dye-sensitized mesoporous semiconductor films - EPFL Thesis n°4731. 1–161 (2010).
6. Maine, P., Strickland, D., Bado, P., Pessot, M. & Mourou, G. Generation of ultrahigh peak power pulses by chirped pulse amplification. *IEEE J. Quant. Electron.* 24, 398–403 (1988).
7. Riedle, E. *et al.* Generation of 10 to 50 fs pulses tunable through all of the visible and the NIR. *Appl. Phys. B* 71, 457–465 (2000).
8. Fork, R. L., Shank, C. V., Hirlimann, C. & Yen, R. Femtosecond white-light continuum pulses. *Opt. Lett.* (1983).
9. Brauer, J. C. Linear and Time-Resolved THz Spectroscopy of Photonic and Charge Transporting Systems - EPFL Thesis n°5444. 1–212 (2012).
10. Horowitz, P. & Hill, W. *The art of electronics*. (Cambridge University Press, 1989).
11. Yamaguchi, S. & Hamaguchi, H.-O. Convenient Method of Measuring the Chirp Structure of Femtosecond White-Light Continuum Pulses. *Appl. Spectrosc.* (1995).

CHAPTER 3

Hole injection in solid-state dye-sensitized solar cells

This chapter introduces the concept of hole injection in solid state dye-sensitized solar cells. A brief review of the literature explaining the main characteristics of this solid-state system is presented, together with its current limitations. Initial measurements are compared with results reported in the literature and confirm the multiexponential dynamics spanning from the picosecond to the nanosecond for the regeneration of the oxidized dye by the hole transport material *spiro*-MeOTAD.

The spectral signature of the system in the visible is however not ideal as it includes both the bleaching of the ground state of the dye as well as the positive absorption from the oxidized *spiro*-MeOTAD. We will show that more accurate information can be obtained by probing the oxidized state of the dye itself in the near-IR, as this gives a direct information on the fraction of dye that has been regenerated by the hole transport material. Measurements in the near IR are presented and the effect of the pore filling fraction of *spiro*-MeOTAD on the dye regeneration is discussed.

3.1 Introduction

Solid-state dye-sensitized solar cells (ssDSCs) are an interesting alternative to liquid electrolytes devices, as they overcome problems related to leakages and corrosion. The first solid-state DSC has been reported by Bach and al. in 1998,¹ and since then much effort has been put into increasing the efficiency of such a system. Nowadays, ssDSCs based on molecular dyes reach 7% efficiency,² which is still half of what is obtained with liquid-based devices. In order to identify the limitations in solid-state systems, it is crucial to gain deeper insight into the study of carrier dynamics, i.e. the kinetics of holes and electrons following light excitation. Understanding the dynamics is of fundamental importance as the system works on a kinetic competition at the heterojunction between the processes of charge separation, such as electron and hole injection, and the processes of charge recombination, which are a principal loss pathway for the system.

In Chapter 1, we described the main mechanistic processes of a DSC. Here we will briefly review them in the case of a solid-state DSC impregnated with the organic hole transport material (HTM) *spiro*-MeOTAD, as shown on Figure 3.1. Under sunlight, the sensitizer, usually a carboxylated ruthenium (II) heteroleptic polypyridyl complex, undergoes several consecutive charge transfer processes: absorption of sunlight leads first to a metal-to-ligand charge transfer (MLCT) transition. Electron injection occurs then from the electronic excited state of the dye (S^*) into the conduction band of a wide bandgap oxide semiconductor such as TiO_2 . The electron injection is known to be ultrafast,³⁻⁶ occurring in the femtosecond timescale (1). Discussion of the possible multiexponential components of electron injection is beyond the scope of this chapter and has been reviewed in Chapter 1. After injection, the oxidized dye needs to be regenerated, and in solid-state DSCs this is practically achieved by the use of *spiro*-MeOTAD (2). Back reactions are indicated as (3) and (4). A schematic view of a solid-state DSC is shown in Figure 3.2.

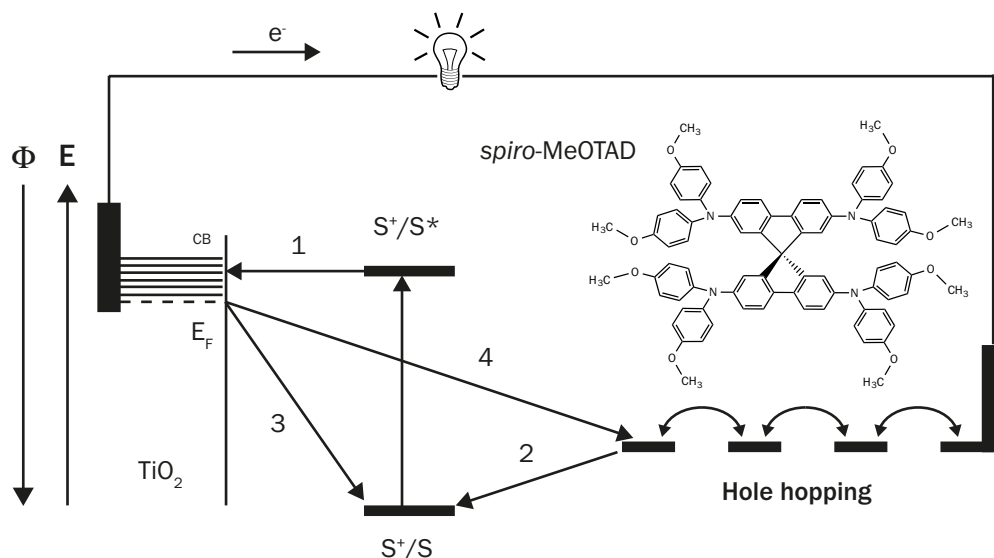


Figure 3.1 Energetic scheme of a ssDSC

After light absorption, the following reactions can occur: 1) Electron injection in the conduction band of the semiconductor, 2) Hole injection from the oxidized sensitizer into the HTM (the arrow is in the direction of electron transfer from the HTM to the oxidized sensitizer), 3) Back electron transfer with oxidized sensitizer, 4) Back electron transfer with oxidized HTM. The proposed mechanism for hole mobility inside the *spiro*-MeOTAD is hopping.

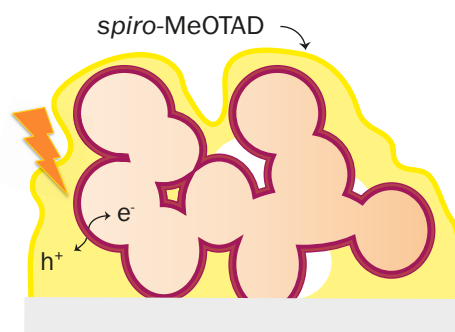


Figure 3.2 Schematic view of solid-state DSC

Mesoscopic TiO_2 covered with dye, and pore filling by *spiro*-MeOTAD. Electron and hole separation after light absorption is shown.

Oxidized dye in contact with HTM can transfer its hole to the HTM - the hole is then transported to the counter electrode where it can recombine with electrons to close the circuit. The dynamics of hole injection has reported by Bach et al. and is known to be largely multiexponential, spanning from the picosecond to nanosecond regime.⁷

The hole injection reaction (2) and extraction is in direct kinetic competition with recombination processes. On a microsecond to millisecond timescale, electrons injected in TiO_2 conduction band can recombine either with remaining oxidized dye (3) or with the oxidized HTM (4). The aim is then to have the fastest charge separation and transfer for the electron and the hole while slowing down the recombination pathways. Another reaction (not drawn on the scheme) that is likely to happen is reductive quenching; in this

case, the hole would be transferred faster to the *spiro*-MeOTAD than injection of the electron in the TiO₂. Evidences of hole transfer faster than electron transfer have been observed by time-resolved photoluminescence studies,⁸ but to date, this reaction has been poorly studied. Nevertheless, it could reveal a major pathway in ssDSCs with respect to liquid DSC, due to the fact that hole injection is a one-electron reaction.

It is worth noting that the reported hole injection in solid-state systems is much faster than for liquid-based DSC, because it involves a one-electron transfer process, whereas the iodide based electrolytes work on a more complicated reaction involving three iodide molecules.^{9,10} This could be seen as an advantage as it competes more efficiently with the recombination of the electron in CB with the oxidized dye (3), but the drawback lies in the fact that the back electron transfer – i.e. the recombination with oxidized hole transporter (4) - is then much faster as well. This has been already confirmed by impedance spectroscopy measurements, which found a recombination rate almost two orders of magnitude larger than for liquid electrolyte DSCs^{11,12} and identified it as a key limitation of the system.^{12,13}

Many parameters have an influence on the charge transfer at the heterojunction. In particular, hole mobility and pore wetting/filling seem to be the most crucial parameters that determine the efficiency of the system. As the accumulation of holes at the interface would lead to increased recombination and prevent further hole injection from the dye, a good hole mobility inside the HTM is needed. Hole mobility is also fundamental to extract efficiently the charge at the counter-electrode and decrease the series resistance through the cell. The other main issue is related to the contact between dye and hole transport material: in case of inhomogeneous and incomplete interfacial contact, the hole will not be efficiently extracted and transported.

3.1.1 Hole mobility

In molecular hole transporters, charge transport is in general different than band-like transport in inorganic semiconductors. It is likely to be a combination of three effects, namely polaron formation and transport, hopping across a Gaussian density-of-states energetic landscape, and carrier trapping.¹⁴ The first mechanism happens because of the strong electron-phonon coupling in organic semiconductor materials. The presence or absence of an extra charge couples with a lattice distortion and then the charge transport occurs from the displacement of the whole quasi-particle. Trap-controlled transport is a

thermally assisted process, where all charges in sites below threshold energy are trapped (not mobile), while all the charges in sites above are free to move. The hopping model considers the hopping of charge carriers within a lattice of localized states. These localized states are subjected to energetic and positional Gaussian disorder. The energetic disorder is due to the fluctuations of energy levels, while the positional disorder results from the fluctuations of intermolecular distances or the orientation of neighboring molecules. The hopping probability is related to electronic wave function overlap factor and Boltzmann factor for jumps to higher energy sites. In the case of real organic semiconductors, charge transport is likely to be explained by a superposition of these three effects depending on the conditions. For example, polaron effects dominate at higher temperatures whereas trapping depends on the density of defects and impurities. In the case of *spiro*-MeOTAD, time-of-flight (TOF) experimental results have been interpreted within the Gaussian disorder model.¹⁵

In the same study, the authors have shown that the hole mobility in *spiro*-MeOTAD is moderate ($2 \cdot 10^{-4} \text{ cm}^2 \text{ V}^{-1} \text{ s}^{-1}$) and that the charge transport is non dispersive, i.e. the carriers propagate through the material as Gaussian carrier packets with comparable velocities. The non-dispersive character is indicative of a relatively low energetic disorder and a small amount of trap states in the material. Further studies by Snaith et al. showed that the hole mobility depends on the charge density.¹⁶ If the density of states is considered as Gaussian, there will be a large amount of states in the center of the Gaussian and the spacing between adjacent states will be small. On the other hand, in the tail of the Gaussian, the number of available states decreases and the average distance between them will increase. If the lower states of the Gaussian are filled with charges, the transport will occur in the center of the Gaussian where the mobility increases due to the proximity of adjacent states.¹⁴ This is schematically shown in Figure 3.3. Thus, the charge density dependence is thought to arise from the filling of deep trap sites. This will effectively reduce the activation required for charge hopping.

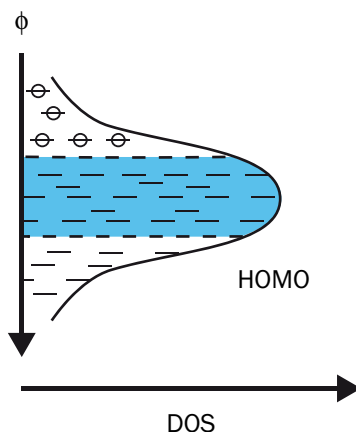


Figure 3.3 Schematic representation of DOS in *spiro*-MeOTAD

The HOMO is considered as a Gaussian distribution of density of states, and the region in blue indicates the energy region in which charge transport occurs easily. Open circles represent the sites occupied by holes and thus not available for transport. Occupying them will increase the probability of the transport occurring in the blue region.

In this context of charge-density dependence, the mobility could greatly be helped by addition of some dopants, which in the same time would reduce the series resistance through the cell,¹⁷ particularly important when a thick capping layer of HTM is present between the mesoporous film and the counter-electrode. The drawbacks of this approach include an increased recombination between electrons in the TiO_2 and the oxidized hole transporter, and a different morphology of the doped HTM, altering its pore filling properties. This was the case with the first solid-state devices that were p-doped with antimony and proved to be less efficient than non-doped devices.¹⁸ Furthermore, care should be taken not to over-oxidise the *spiro*-MeOTAD to avoid energetic mismatches between the TiO_2 and the HTM.¹⁹ Addition of ionic salts, such as lithium bis(trifluoromethylsulfonyl)imide salt (LiTFSI), appeared to be a better way to enhance the conductivity in *spiro*-MeOTAD films. It has been shown that the mobility of *spiro*-MeOTAD infiltrated in TiO_2 mesoporous network could be increased of one order of magnitude, up to $2 \cdot 10^{-3} \text{ cm}^2 \text{ V}^{-1} \text{ s}^{-1}$, upon addition of LiTFSI salt.¹⁸ These initial studies did not show evidences of chemical oxidation of the HTM by LiTFSI; the significant improvement in mobility was not attributed to increased charge density but rather to increased disorder into the network, leading to a broadening of the tails of the density of states, which gave more available sites for hole transport. However, more recent studies have shown the complex interplay between lithium salts, oxygen and *spiro*-MeOTAD.^{20,21} Abate et al. demonstrate and identify a mechanism by which Li^+ p-dopes *spiro*-MeOTAD in the presence of oxygen, and which consumes the lithium salt. Hence, increasing the charge density by p-doping without detrimentally altering the morphology

appears as an effective way to increase the mobility in organic semiconductors such as *spiro*-MeOTAD. Energy level shifts in *spiro*-MeOTAD upon LiTFSI addition was confirmed by photoelectron spectroscopy, thus supporting the hypothesis of a p-doping.²²

However, it has to be born in mind that LiTFSI effect is not limited to the HTM layer. In liquid devices, similarly to H⁺ ions, Li⁺ small cations can adsorb on the TiO₂ surface and lower its conduction band position,²³ thus increasing current generation but decreasing the open-circuit voltage of the cell. However, in ssDSCs it was observed that the open-circuit voltage of the cells was monotonically raised with increasing amount of lithium salts.²⁴ Therefore, the action of LiTFSI might be a complex interplay of many factors. In addition to lithium salts, 4-tert-butyl-pyridine (tBP) is a widely used additive to improve the performance of solar cells. tBP is generally considered to adsorb on the TiO₂ surface and act by suppression of the dark current at the semiconductor electrolyte or HTM junction, presumably blocking surface states that are active in the charge transfer.^{25,26} Furthermore, tBP acts as a proton sponge and helps solvating the Li⁺ ions, to inhibit their adsorption at the surface of TiO₂.¹⁴ Lithium ions and tBP are used in combination to obtain the best DSCs efficiencies, but to date still many things remain to learn about the exact nature of their synergy in ssDSCs.

3.1.2 Pore wetting and filling

The pore infiltration of *spiro*-MeOTAD into the mesoporous TiO₂ network has been studied extensively during the last years. Contadictory studies can be found in the literature on this topic. While some works have reported a complete pore filling even in films thicker than 2 μm,²⁷ many studies point in the direction of a partial or incomplete pore filling.^{26,28-32} It is generally considered that the pore filling remains one of the main sources of limitation of the system, especially in regard to liquid-based DSCs where the electrolyte evenly distributes in the porous structure.

The terminology of “pore filling” should be made more explicit there. Several parameters are taken into account when talking about pore filling, the major two being the infiltration depth and the pore filling fraction (i.e. the volume fraction of the pores filled by the HTM). Other important aspects include the wetting of the pore, which would be an indication of the homogeneity of the HTM film (Figure 3.4). Clearly, irregularities in the HTM deposition or segregation of the HTM would be detrimental for the hole transport

properties. It is still not very clear if *spiro*-MeOTAD deposits as a thin film or if “packets” are formed following solvent evaporation – and this cannot be resolved by electron microscopy techniques.

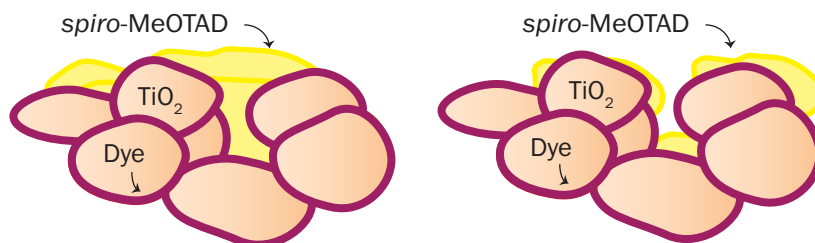


Figure 3.4 Schematic view of pore filling

Left: High pore filling; Right: Low pore filling.

All these parameters have to be optimized in order to have the best performing device. The dye's oxidized state must have an HTM molecule nearby in order to inject its hole, and this relates to the wetting of the surface. Once injected, the hole must be allowed to travel by the shortest path. If the HTM only deposits as a thin film, the hole will have more chances of recombination at the interface than if the pore is sufficiently filled with *spiro*-MeOTAD so that the charge can be directly extracted. The straightforward evidence for this picture is that higher performing cells are obtained when using higher concentration of *spiro*-MeOTAD in solution.²⁶

X-ray photoelectron spectroscopy studies showed that the infiltration depth was complete up to 5 μm TiO_2 thickness and that the concentration of the HTM was constant throughout the film.³¹ Nevertheless, the pore filling fraction decreased as the film thickness increases. This issue cannot be solved by further increasing the *spiro*-MeOTAD concentration in solution as there is a kinetic restraint: due to the evaporation of the solvent, only a limited amount of HTM can infiltrate into the pore before the excess solution is dried, forming an overlayer. This implies that is physically not possible to obtain a value of 100% pore filling fraction; in fact, Ding et al. estimated that for state-of-art devices with 2.5 μm thickness, the filled volume of the pores is 60-65%.³¹ For this reason, the optimized thickness for the TiO_2 film in the ssDSC is commonly accepted as below 3 μm . Over this value, problems of incomplete filling become dominant and the performance of the cells is greatly affected. TiO_2 films used for liquid-based DSC are usually three times thicker to maximize dye loading and light harvesting. Hence, the solid-state device must compromise between the pore filling parameter and light absorption. In

order to maximize the light absorption properties, one of the proposed solutions is use high extinction coefficient organic dyes.^{33,34} On the other hand, suggestions to overcome the pore filling problem include the use of larger pore size,³⁵ but then the lower dye loading problem would have to be addressed as well. Other possibilities concern the use of different types of TiO₂ nanostructures, such as TiO₂ fibers or nanowires.³⁶ Alternative casting techniques to the spin-coating method currently used could also be considered.^{29,37} It is also worth noting that many other hole transport materials have been tested, including smaller molecules that were thought to increase the pore filling fraction, but so far none have been shown to work better than *spiro*-MeOTAD.³⁸

Many experimental factors have an influence on the effective pore filling: besides the *spiro*-MeOTAD concentration in solution, the spin coating speed and acceleration are likely to influence the infiltration.³¹ In a study where the pore filling was increased from 26% to 65%, the authors demonstrated that higher hole injection efficiency can be obtained between these two limits, while slowing down the recombination rate because of better hole diffusion and therefore reduction of the hole concentration at the interface.³⁹ The hole injection efficiency was estimated by laser flash photolysis: the relative amount of *spiro*-MeOTAD oxidized state formed after the hole injection from the dye was monitored before its decay due to recombination with electrons in TiO₂. Higher pore filling resulted in higher signal from the HTM oxidized state, indicating clearly that at low pore filling fractions, many holes could not be injected because of lack of HTM.

Besides being one of the most crucial parameter for ssDSCs efficiency, pore filling is probably the most difficult to control. Difficulties in reproducibility of solid-state devices are often associated with it and not entirely understood. The HTM penetration is likely to be influenced by small changes in the sample preparation; due to the hydrophobic nature of the HTM, one of the issues is related with the nature of the dye. The more hydrophobic the dye is, the higher the probability of a better wetting of its surface by the dye will be. Other factors that are more difficult to control, such as the presence of dye aggregates at the surface, or even the presence of water into the pores, can have a detrimental effect on the pore filling.

3.1.3 Interface engineering

Other strategies not directly related to hole mobility or improved pore filling have been demonstrated to be useful in order to improve ssDSCs; these were mainly related with interface engineering that could retard the $e^-_{CB} - \text{HTM}^+$ recombination (4). Kroeze et al. reported longer recombination times by using dyes with long alkyl chains, acting as an insulating barrier for electron-hole recombination.⁴⁰ This is also one of the reasons Z907, with its long alkyl chains (C₉H₁₉) was subsequently used in our group as the standard for the ssDSCs. The long alkyl chains then have a double utility, as they can act as an insulating barrier, but are also strongly hydrophobic, thus helping in the wetting of the pores by the hydrophobic *spiro*-MeOTAD. Control of the interface electrostatics was also proposed.^{11,24,41} As an example, a dual-functional HTM is sandwiched between the dyed TiO₂ films and the normal HMT. This dual-functional HTM consists of a conjugated organic semiconductor grafted with ion supporting side chains, in this case tetra-ethylene glycol (TEG) chains, each able to coordinate one Li⁺ ion. The authors explain that this strategy removes the need to add tBP in the system to help LiTFSI solvation, as well as adding a screening layer of positive ions between the dye and the normal HTM without affecting the initial hole transfer yield. In the work by Hirata et al.,¹¹ a polymer with higher ionization potential than *spiro*-MeOTAD is used in between the dyed TiO₂ film and the *spiro*-MeOTAD. The polymer works as a spatial separator as well as allows achieving a redox cascade from the dye, to the polymer, and finally to the *spiro*-MeOTAD.

In this chapter, we will mainly show how it is possible to monitor the hole transfer reaction by transient absorption spectroscopy, and discuss its efficiency with respect to one of the parameters discussed above, i.e. pore filling.

3.2 Methods

3.2.1 Samples preparation

TiO₂ films were deposited by screen printing on microscopic glass slides and sintered for 30 min at 450°C before being dipped overnight into dye solutions of ~0.3 mM concentration. Two different dyes were used, either N3 (*cis*-bis(isothiocyanato)bis(2,2'-bipyridyl-4,4'-dicarboxylato)-ruthenium(II)) or Z907 (*cis*-disothiocyanato-(2,2'-bipyridyl-

4,4'-dicarboxylic acid)-(2,2'-bipyridyl-4,4'-dinonyl) ruthenium(II)); their chemical structure is shown in Figure 3.5. *Spiro*-MeOTAD (Merck KGaA) solutions were prepared in glovebox by dissolving the HTM in chlorobenzene at 60°C for 30 min. Unless otherwise stated, solution of 180 mg/ml of *spiro*-MeOTAD were used. In case where additives were used, lithium bis(trifluoromethylsulfonyl)imide salt (LiTFSI) dissolved in acetonitrile (170 mg/ml) was added to the *spiro* solution at a ratio of 15 μ l LiTFSI solution:72 mg *spiro*-MeOTAD, and 4-tert-butylpyridine (tBP) was added at a ratio of 7 μ l TBP:72 mg *spiro*-MeOTAD.

To obtain different pore filling fractions, the *spiro*-MeOTAD solution was diluted with chlorobenzene to various concentrations, but the ratio of *spiro*-MeOTAD to LiTFSI and tBP remained unchanged.

50 μ l of *spiro*-MeOTAD solution was deposited onto the dyed cell. After waiting 45 s in order to maximize the penetration of the solution prior to spin-coating, the cells were then spin-coated at a rate of 2000 rpm for 30 s. The samples were then left overnight either in a drybox or in a glovebox to allow full evaporation of the chlorobenzene. Finally, samples were sealed with Surlyn[®] polymer and thin microscopic glass slides in order to avoid contact with oxygen and external contaminations.

3.2.2 Femtosecond transient absorption

The setup has been described in detail in Chapter 2. The experimental configuration used in the work presented in this chapter was two-colors pump-probe experiments where two NOPAs allowed tuning two monochromatic beams at the desired wavelength. Since most of the measurements needed a probe in the near IR (840 nm) – the white light setup has not been used for these studies. Extension of the WLC to the near-IR region came later.

The outputs of the NOPAs are compressed by a pair of SF10 prisms down to sub 50 fs pulses. Measurement of the temporal profile of the pulses was done with an intensity autocorrelator (APE PulseCheck 15 Short Pulse). The pump is chopped at half the repetition frequency of the pulsed laser source. The change in transmittance of the sample, i.e. change in intensity of the probe beam, is measured by a photodiode (Nirvana detector, New Focus, model 2007) placed after the sample and protected by cut-off filters to avoid any scattering signal from the pump. The low-amplitude signal is extracted by a lock-in amplifier (SR-830, Stanford Research) referenced to the chopper.

Isotropic excitation of the sample is achieved through pump polarization set at the magic angle (54.7°) relative to the probe pulse with a $\lambda/2$ waveplate. The typical fluences on the sample are low to avoid kinetics depending on the laser intensity (energies were usually 70 nJ for the pump with 250 μm beam diameter and 30 nJ for the probe with beam diameters of 150 μm). A lens allows tuning the size of the pump before the sample to both decrease the fluence and allow for complete overlap of the probe. The instrument response function is typically of 120 fs.

3.3 Monitoring of the hole transfer reaction

This section will present several ways to monitor the hole transfer reaction (3) and compare it to previously published data. By the choice of the wavelengths of analysis, it will be shown that the data may be used as a direct estimation of the fraction of dye directly in contact with HTM. The influence of the pore filling fraction on the hole injection efficiency will then be addressed.

The initial results on the dynamic of hole injection were obtained on devices prepared with N3 dye, the first ruthenium sensitizer used in DSCs (Figure 3.5a). For the WLC experiments and pore filling studies, Z907 was used instead (Figure 3.5b). The two dyes have been extensively studied and their spectroscopic properties are well known. Due to their analogous structure, they have similar absorption spectra in their ground and oxidized state, which allowed using the same wavelengths for excitation and detection for transient absorption measurements.

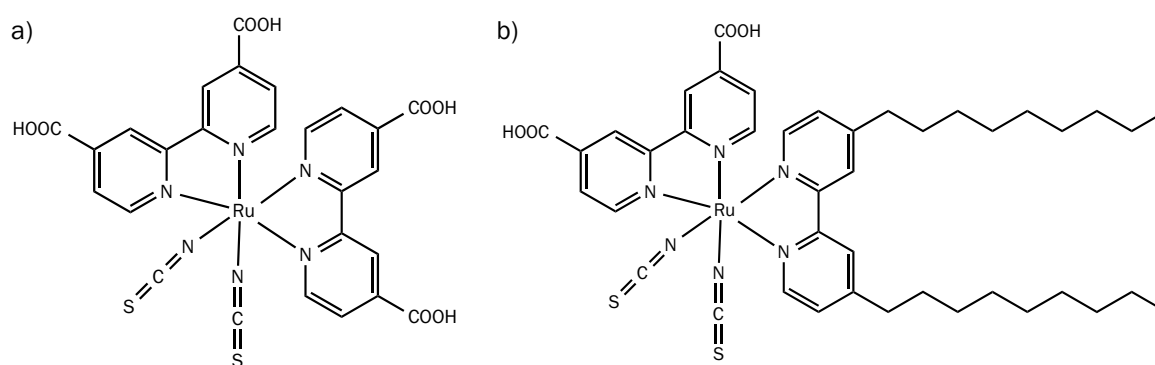


Figure 3.5 N3 dye (a) and Z907 dye (b)

3.3.1 Dynamics of hole injection in the visible

Figure 3.6 shows the initial measurements performed on the setup, that were carried out in order to check if the results were in agreement with previously published dynamic data.⁷ The excitation wavelength was set to 600 nm where only the ground state of the N3 dye is absorbing, while the probe was set to 520 nm where both the ground state of the dye as well as the oxidized form of the hole transport material absorb.⁷ The results shown in Figure 3.6a and Figure 3.6b display a very fast initial decay attributed to the bleaching of the ground state of the N3 dye.⁴ The slowest and positive components could be attributed to the appearance of the *spiro*-MeOTAD oxidized signal. The increase of *spiro*-MeOTAD is still visible on the nanosecond timescale (Figure 3.6a). Signal from a dyed sample without any HTM and covered with propylene carbonate is shown as a comparison to see the long lasting bleaching of the dye when no *spiro*-MeOTAD is present to extract a hole from it.

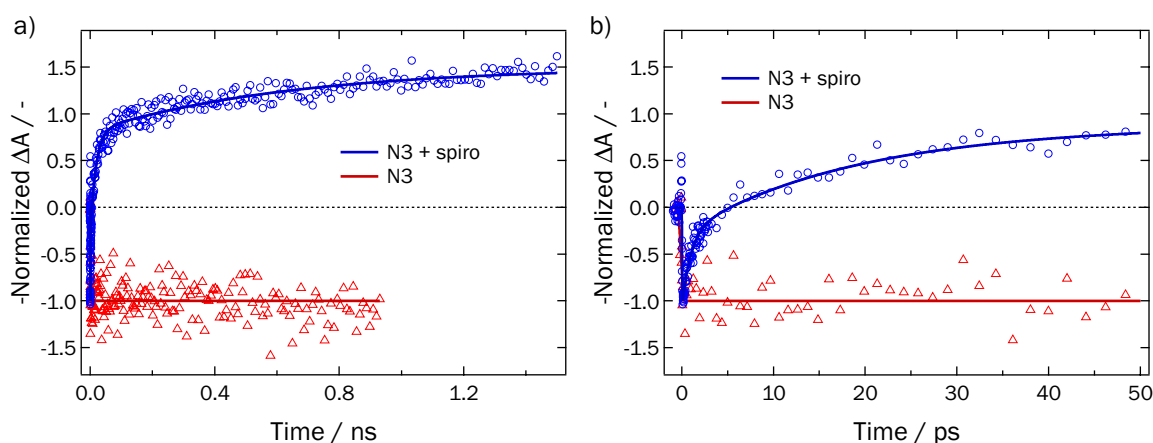


Figure 3.6 Femtosecond transient absorption of N3 | TiO₂

$\lambda_{\text{pump}} = 600 \text{ nm}$, $\lambda_{\text{probe}} = 520 \text{ nm}$. a) Blue dots: N3 | TiO₂ sample with *spiro*-MeOTAD; red triangles: N3 | TiO₂ reference (sample without *spiro*-MeOTAD) covered with propylene carbonate. Blue solid line is a fit result from the analytical convolution function of one Gaussian instrument response and four exponentials (the fourth exponential being fixed to a very long timescale), red solid line is plotted for illustration. b) Larger view of a) (0 – 50 ps). Fluence = 35 $\mu\text{J}/\text{cm}^2$.

The multiexponential dynamics observed is in agreement with what has been reported by Bach et al. (Table 3.1).⁷ These results are a first indication of an incomplete and inhomogeneous contact between the dye and the HTM. A first fraction of the dye molecules, well covered by the HTM, are rapidly regenerated, while the plateau indicates a region of the sample where the regeneration is slower. This is an indication for a distribution of distances between the dye molecules and the HTM molecules. Several

studies have also suggested that local variations in the electrostatics of the interface may exist.^{42,43} Haque et al. observed a weak dependence of the hole transfer yield on the energetic driving force for the hole injection reaction ($\Delta G_{\text{dye-HTM}}$); and explained this by an inhomogeneous broadening of the energetic driving force due to local variations of the TiO_2 | dye | HTM interface. The theoretical work by Bisquert et al. supports these experimental findings and stresses the importance of energetic disorder. However, energetic disorder and spatial disorder might be two sides of the same coin: indeed, specific orientation of the HTM molecule in the pore, coupled with ions distribution, may lead to variations in the energetics at the surface.

Table 3.1 Time constants for hole injection in N3+HTM|TiO₂, $\lambda_{\text{pump}} = 600$ nm, $\lambda_{\text{probe}} = 520$ nm

	τ_1	τ_2	τ_3
Time constant/ps	1	20	600
	A_1	A_2	A_3
Relative amplitude (%)	30	44	26

Similar measurements were performed on samples with Z907 dye, used in our group as the standard for the ssDSCs (absorption spectra of Z907-dyed samples are shown in Chapter 4). The results for the hole injection dynamics are very similar to what is obtained with the N3 dye. Figure 3.7 illustrates the hole transfer reaction from another perspective, and in a sample with Z907 dye. Transient absorption spectrum with a white-light continuum (WLC) probe was recorded at 580 nm excitation. Figure 3.7a shows a reference Z907 sample deposited on mesoporous TiO_2 , covered with propylene carbonate. Similarly to the N3 dye, the typical features of a ground state bleaching can be seen in the blue region (430-550 nm), while a small positive absorption from the dye's oxidized state after electron injection in the TiO_2 can be observed after 600 nm. The situation changes drastically with HTM addition: in Figure 3.7b, the negative band from 475 to 550 nm gradually becomes positive, thus showing the formation of oxidized *spiro*-MeOTAD that has a characteristic absorption peak in that range.⁴⁴

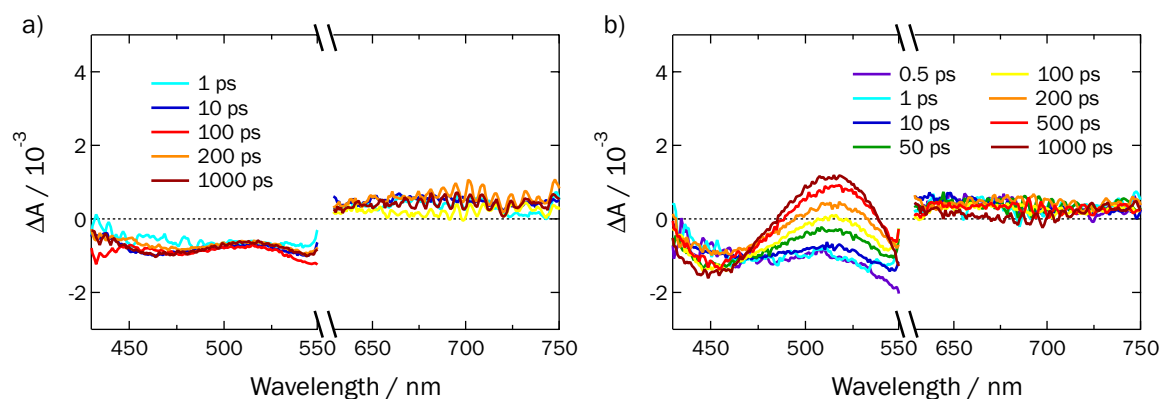


Figure 3.7 Broadband femtosecond transient absorption of Z907 | TiO₂

$\lambda_{\text{pump}} = 580$ nm, WLC probe. a) Z907|TiO₂ reference (sample without *spiro*-MeOTAD) covered with propylene carbonate. b) Z907|TiO₂ sample with *spiro*-MeOTAD. Color lines correspond to different time delays after the pump excitation. Fluence = 70 $\mu\text{J}/\text{cm}^2$.

3.3.2 Dynamics of hole injection in the near IR

Similar samples as in section 3.3.1 and sensitized with N3 dye were measured at a different probe wavelength, in the near IR. The aim was to observe the dynamics of the oxidized dye without any or little contribution from the oxidized state of the *spiro*-MeOTAD. This was achieved by monitoring the hole injection at 840 nm (NCS Ru(III) MLCT transition),⁴⁵ where the absorption from oxidized *spiro*-MeOTAD and electrons is low. However, their absorption cannot be completely neglected, and for extraction of the exact time constants related to the process of hole injection, as well as the contribution to the absorption of every species present, a kinetic model is presented in Chapter 4. Thus, in this section, the time constants extracted from the fit with the analytical convolution function of one Gaussian instrument response and three exponentials are given for qualitative discussion on the samples but are not representative of any process in the system. Results for a sample of N3 impregnated with *spiro*-MeOTAD are reported in Figure 3.8.

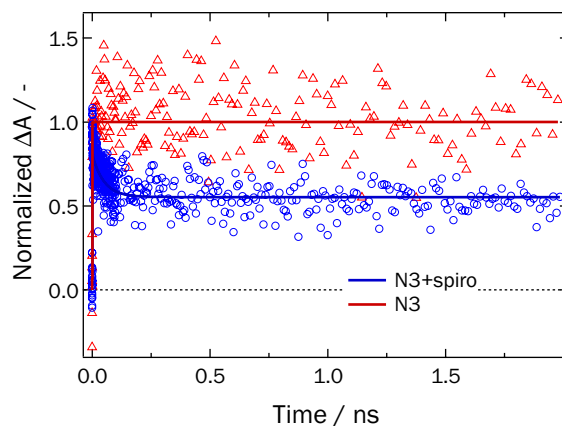


Figure 3.8 Femtosecond transient absorption of N3 | TiO₂

$\lambda_{\text{pump}} = 600 \text{ nm}$, $\lambda_{\text{probe}} = 840 \text{ nm}$. Blue dots: N3 | TiO₂ sample with *spiro*-MeOTAD; red triangles: N3 | TiO₂ reference (sample without *spiro*-MeOTAD) covered with propylene carbonate. Signal is mainly attributed to the oxidized form of the dye, with little contribution from electrons and the oxidized form of *spiro*-MeOTAD. Blue solid line is a fit result from the convolution of one Gaussian instrument response and three exponentials, red solid line is plotted for illustration. Fluence = 35 $\mu\text{J}/\text{cm}^2$.

Table 3.2 Time constants for hole injection in N3+HTM | TiO₂, $\lambda_{\text{pump}} = 600 \text{ nm}$, $\lambda_{\text{probe}} = 840 \text{ nm}$

	τ_1	τ_2	τ_3
Time constant/ps	1	50	long
	A_1	A_2	A_3
Relative amplitude (%)	24	24	52

An analogous multiexponential behavior is observed: half of the dye is regenerated in approximately 100 ps, while the other half is still under its oxidized form at 2 ns. The first and second time constants are similar to what is extracted from the measurements at a probe wavelength of 520 nm – confirming the hypothesis of a very fast hole injection for the dye molecules in direct contact with the HTM (Table 3.2).

The slow part is less straightforward to rationalize. Bach et al. estimated that the regeneration should be complete in a few nanoseconds, monitoring the formation of oxidized *spiro*-MeOTAD. It is not unlikely though that the information extracted from there is slightly different than what is given by the direct regeneration of the dye. In fact, fitting the formation of oxidized *spiro*-MeOTAD introduces an estimation of its final quantity that could be fairly different from the actual value, while the information obtained by the oxidized dye decaying dynamic is straightforward and gives a direct quantification of the hole injection efficiency. To go further in this direction, probing the dynamic of oxidized dye gives a direct measurement of the fraction of the dye that is not

regenerated because of non-contact with the HTM. On the other hand, when probing the appearance of oxidized *spiro*-MeOTAD, this information is missing and may underestimate the fact that a fraction of the dye molecules is in a segregated zone, not in contact with the HTM, and will follow a completely different kinetic. In fact, a model of two separate compartments could be hypothesized from these results: regions of dye well contacted with HTM that follow picosecond regeneration dynamics, and regions of total non-contact, where the dye is only subject to recombination with electrons in TiO₂ (dynamical process that is known to happen on the late microsecond – millisecond timescale). This simplified model would underline the important role played by the pore filling morphology by the HTM. To further confirm this, an interesting axis of research would be to understand if there are really two separate compartments or if some of the holes could hop from one dye to another until they reach the next region contacted by *spiro*-MeOTAD. Self-exchange hole transfer for Z907 dye in a liquid electrolyte has been evidenced by polarized transient absorption spectroscopy.⁴⁶ This would be an interesting technique to apply to solid-state systems.

For all the above-mentioned reasons, further measurements in the thesis were conducted at a probe wavelength of 840 nm to follow the decrease of the oxidized state of the dye, which is a straightforward indication of hole injection.

3.4 Investigation of the effect of pore filling fraction

As the pore filling appears to be one of the greatest bottlenecks of the system, a logical experiment was to look at the influence of the pore filling fraction on the kinetic of hole injection. The regeneration of the oxidized dye was then probed for two samples with different HTM concentration in the casting solution (72 mg/ml and 180 mg/ml of *spiro*-MeOTAD in chlorobenzene, corresponding respectively roughly to a calculated pore filling fraction of 26% and 65%).³¹ Figure 3.9 shows their kinetics over the first 20 ps. The overall kinetics over 2 ns was fitted with the convolution of one Gaussian and three exponential and yielded time constants similar to the ones reported in Section 3.3.2, reported for the N3 dye (Table 3.3). Only the first two exponentials are visible in Figure 3.9. Again, there is a good agreement between the results obtained for the N3 dye and Z907.

The amplitude of the first component ($\tau_1 = 1$ ps) is larger in the case of the higher pore filling (45% vs. 25%, Table 3.3), thus confirming the importance of the pore filling

parameter, in the early dynamic of hole injection. It is worth noting that the extinction coefficient of the oxidized form of *spiro*-MeOTAD is much smaller at this wavelength than the one of the dye, as it will be described in Chapter 4.

These results highlight that the electron transfer from the HTM to the oxidized dye is a fast one-electron transfer reaction and its only kinetic limitation comes from the actual distance and contact between the two reactants.

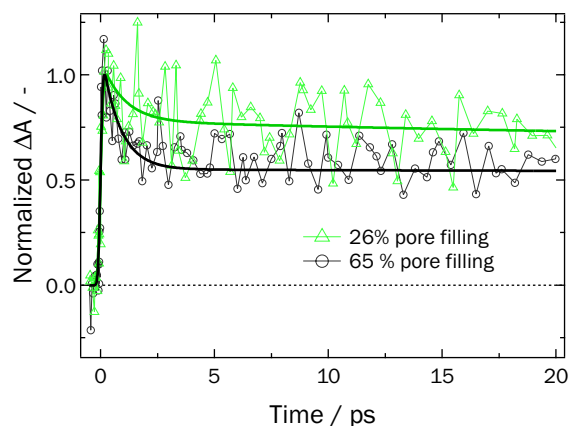


Figure 3.9 Femtosecond transient absorption of Z907 | TiO₂

$\lambda_{\text{pump}} = 600 \text{ nm}$, $\lambda_{\text{probe}} = 840 \text{ nm}$. Green triangles: 26% pore filling (corresponding to 72 mg/ml of *spiro*-MeOTAD in the casting solution); black circles: 65% pore filling fraction (corresponding to 180 mg/ml of *spiro*-MeOTAD in the casting solution). Signal is mainly attributed to the oxidized form of the dye, with little contribution from electrons and the oxidized form of *spiro*-MeOTAD. Solid lines results from the convolution of one Gaussian and three exponentials over a timescale of 2 ns. Only the first 20 ps are shown here. Fluence = 35 $\mu\text{J}/\text{cm}^2$.

Table 3.3 Time constants for hole injection in Z907+HTM | TiO₂, $\lambda_{\text{pump}} = 600 \text{ nm}$, $\lambda_{\text{probe}} = 840 \text{ nm}$, for different pore filling fractions

	τ_1	τ_2	τ_3
Time constant/ps	1	50	long
Relative amplitude (%)	A_1	A_2	A_3
26% pore filling	25	13	62
65% pore filling	45	15	40

3.5 Conclusion

In this chapter, the main issues related with solid-state DSCs have been discussed. Hole mobility and pore filling appear to be the key factors influencing these devices, which still need further understanding in order to obtain better performing devices. Time-resolved absorption spectroscopy is presented as a powerful tool to investigate the intricate kinetic processes that occur at the heterojunction of such a system. Femtosecond transient absorption dynamics in the visible allow following the regeneration of the ground state of the dye by oxidized *spiro*-MeOTAD, which appears to be multiexponential, indicating a large distribution of distances in the system. The optical signals in this region contain a mixture of the ground state bleaching and the oxidized *spiro*-MeOTAD, thus rendering more difficult the analysis of the dynamics. We show herein that probing in the near-IR gives access to the quenching of the oxidized state of the dye by the hole transport material *spiro*-MeOTAD, which is a direct information of the hole injection yield. Kinetic decay of the oxidized form of the sensitizer in the picosecond regime helps establishing a model for the morphology of the nanoporous structure filled with HTM. It is further shown that the pore filling fraction parameter is of crucial importance for the early dynamics of hole injection.

3.6 References

1. Bach, U. *et al.* Solid-state dye-sensitized mesoporous TiO₂ solar cells with high photon-to-electron conversion efficiencies. *Nature* 395, 583–585 (1998).
2. Burschka, J. *et al.* Tris(2-(1H-pyrazol-1-yl)pyridine)cobalt(III) as p-type dopant for organic semiconductors and its application in highly efficient solid-state dye-sensitized solar cells. *J. Am. Chem. Soc.* 133, 18042–18045 (2011).
3. Hannappel, T., Burfeindt, B., Storck, W. & Willig, F. Measurement of ultrafast photoinduced electron transfer from chemically anchored Ru-dye molecules into empty electronic states in a colloidal anatase TiO₂ film. *J. Phys. Chem. B* 101, 6799–6802 (1997).
4. Tachibana, Y., Moser, J.-E., Grätzel, M., Klug, D. R. & Durrant, J. R. Subpicosecond interfacial charge separation in dye-sensitized nanocrystalline titanium dioxide films. *J. Phys. Chem.* 100, 20056–20062 (1996).

5. Tachibana, Y., Haque, S. A. & Mercer, I. P. Electron Injection and Recombination in Dye Sensitized Nanocrystalline Titanium Dioxide Films: A Comparison of Ruthenium Bipyridyl and Porphyrin Sensitizer Dyes. *J. Phys. Chem. B* (2000).
6. Wenger, B., Grätzel, M. & Moser, J.-E. Rationale for kinetic heterogeneity of ultrafast light-induced electron transfer from Ru(II) complex sensitizers to nanocrystalline TiO₂. *J. Am. Chem. Soc.* 127, 12150–12151 (2005).
7. Bach, U. *et al.* Charge separation in solid-state dye-sensitized heterojunction solar cells. *J. Am. Chem. Soc.* 121, 7445–7446 (1999).
8. Snaith, H. J., Petrozza, A., Ito, S., Miura, H. & Grätzel, M. Charge Generation and Photovoltaic Operation of Solid-State Dye-Sensitized Solar Cells Incorporating a High Extinction Coefficient Indolene-Based Sensitizer. *Adv. Funct. Mater.* 19, 1810–1818 (2009).
9. Moser, J.-E. in *Dye-sensitized Solar Cells* (Kalyanasundaram, K.) 403–456 (EPFL Press, 2009).
10. Teuscher, J. *et al.* Kinetics of the Regeneration by Iodide of Dye- Sensitizers Adsorbed on Mesoporous Titania. *J. Phys. Chem. C* (2014).
11. Hirata, N. *et al.* Interface engineering for solid-state dye -sensitised nanocrystalline solar cells: the use of an organic redox cascade. *Chem. Comm.* 535–537 (2006). doi:10.1039/B513180D
12. Fabregat-Santiago, F. *et al.* Electron Transport and Recombination in Solid-State Dye Solar Cell with Spiro-OMeTAD as Hole Conductor. *J. Am. Chem. Soc.* 131, 558–562 (2009).
13. Fabregat-Santiago, F., Bisquert, J., Palomares, E., Haque, S. A. & Durrant, J. R. Impedance spectroscopy study of dye-sensitized solar cells with undoped spiro-OMeTAD as hole conductor. *J. Appl. Phys.* 100, 034510 (2006).
14. Snaith, H. J. in *Dye-sensitized Solar Cells* (Kalyanasundaram, K.) 163–206 (EPFL Press, 2009).
15. Poplavskyy, D. Nondispersive hole transport in amorphous films of methoxy-spirofluorene-arylamine organic compound. *J. Appl. Phys.* 93, 341–346 (2003).
16. Snaith, H. J. & Grätzel, M. Light-enhanced charge mobility in a molecular hole transporter. *Phys. Rev. Lett.* 98, 177402 (2007).

17. Dualeh, A., Moehl, T., Nazeeruddin, M. K. & Grätzel, M. Temperature dependence of transport properties of spiro-MeOTAD as a hole transport material in solid-state dye-sensitized solar cells. *ACS Nano* 7, 2292–2301 (2013).
18. Snaith, H. J. & Grätzel, M. Enhanced charge mobility in a molecular hole transporter via addition of redox inactive ionic dopant: implication to dye-sensitized solar cells. *Appl. Phys. Lett.* 89, 262114 (2006).
19. García-Cañadas, J. *et al.* Determination of electron and hole energy levels in mesoporous nanocrystalline TiO₂ solid-state dye solar cell. *Synthetic Metals* 156, 944–948 (2006).
20. Cappel, U. B., Daeneke, T. & Bach, U. Oxygen-Induced Doping of Spiro-MeOTAD in Solid-State Dye-Sensitized Solar Cells and Its Impact on Device Performance. *Nano. Lett.* 12, 4925–4931 (2012).
21. Abate, A. *et al.* Lithium salts as ‘redox active’ p-type dopants for organic semiconductors and their impact in solid-state dye-sensitized solar cells. *Phys. Chem. Chem. Phys.* 15, 2572–2579 (2013).
22. Schölin, R. *et al.* Energy Level Shifts in Spiro-OMeTAD Molecular Thin Films When Adding Li-TFSI. *J. Phys. Chem. C* 116, 26300–26305 (2012).
23. Haque, S. A. *et al.* Parameters influencing charge recombination kinetics in dye-sensitized nanocrystalline titanium dioxide films. *J. Phys. Chem. B* 104, 538–547 (2000).
24. Kuang, D. *et al.* Ion coordinating sensitizer for high efficiency mesoscopic dye-sensitized solar cells: influence of lithium ions on the photovoltaic performance of liquid and solid-state cells. *Nano. Lett.* 6, 769–773 (2006).
25. Nazeeruddin, M. K. *et al.* Conversion of light to electricity by cis-X₂bis (2, 2'-bipyridyl-4, 4'-dicarboxylate) ruthenium (II) charge-transfer sensitizers (X= Cl-, Br-, I-, CN-, and SCN-) on nanocrystalline titanium dioxide electrodes. *J. Am. Chem. Soc.* 115, 6382–6390 (1993).
26. Schmidt-Mende, L. & Grätzel, M. TiO₂ pore-filling and its effect on the efficiency of solid-state dye-sensitized solar cells. *Thin Solid Films* 500, 296–301 (2006).
27. Docampo, P., Hey, A., Guldin, S. & Gunning, R. Pore Filling of Spiro-OMeTAD in Solid-State Dye-Sensitized Solar Cells Determined Via Optical Reflectometry. *Adv. Funct. Mater.* (2012).
28. Olson, C., Veldman, D., Bakker, K. & Lenzmann, F. Characterization of the pore filling of solid state dye sensitized solar cells with photoinduced absorption spectroscopy. *Int. J. Photoenergy* 2011, 1–11 (2011).

29. Ding, I.-K. *et al.* Deposition of hole-transport materials in solid-state dye-sensitized solar cells by doctor-blading. *Organic Electronics* 11, 1217–1222 (2010).
30. Docampo, P. *et al.* Control of Solid-State Dye-Sensitized Solar Cell Performance by Block-Copolymer-Directed TiO₂ Synthesis. *Adv. Funct. Mater.* 20, 1787–1796 (2010).
31. Ding, I.-K. *et al.* Pore-filling of spiro-OMeTAD in solid-state dye sensitized solar cells: quantification, mechanism, and consequences for device performance. *Adv. Funct. Mater.* 19, 2431–2436 (2009).
32. Snaith, H. J. *et al.* Charge collection and pore filling in solid-state dye-sensitized solar cells. *Nanotechnology* 19, 424003 (2008).
33. Dualeh, A. *et al.* Influence of Donor Groups of Organic D- π -A Dyes on Open-Circuit Voltage in Solid-State Dye-Sensitized Solar Cells. *J. Phys. Chem. C* 116, 1572–1578 (2012).
34. Cai, N. *et al.* An Organic D- π -A Dye for Record Efficiency Solid-State Sensitized Heterojunction Solar Cells. *Nano. Lett.* 11, 1452–1456 (2011).
35. Feng, W., Umeda, T., Fujii, A., Wang, X. & Yoshino, K. Enhancement of Photoresponse by Enlarging the Effective Interface between Conducting Polymer and Titanium Oxide in Photovoltaic Device. *Jpn. J. Appl. Phys.* 43, 3473–3478 (2004).
36. Tétreault, N. *et al.* High-efficiency solid-state dye-sensitized solar cells: fast charge extraction through self-assembled 3D fibrous network of crystalline TiO₂ nanowires. *ACS Nano* 4, 7644–7650 (2010).
37. Fredin, K., Johansson, E., Blom, T. & Hedlund, M. Using a molten organic conducting material to infiltrate a nanoporous semiconductor film and its use in solid-state dye-sensitized solar cells. *Synthetic Metals* (2009).
38. Kroeze, J. E. *et al.* Parameters influencing charge separation in solid-state dye-sensitized solar cells using novel hole conductors. *Adv. Funct. Mater.* 16, 1832–1838 (2006).
39. Melas-Kyriazi, J. *et al.* The Effect of Hole Transport Material Pore Filling on Photovoltaic Performance in Solid-State Dye-Sensitized Solar Cells. *Adv. Energy Mater.* 1, 407–414 (2011).
40. Kroeze, J. E. *et al.* Alkyl Chain Barriers for Kinetic Optimization in Dye-Sensitized Solar Cells. *J. Am. Chem. Soc.* 128, 16376–16383 (2006).

41. Haque, S. A. *et al.* Interface Engineering for Solid-State Dye-Sensitized Nanocrystalline Solar Cells: The Use of Ion-Solvating Hole-Transporting Polymers. *Adv. Funct. Mater.* 14, 435–440 (2004).
42. Haque, S. A., Park, T., Holmes, A. B. & Durrant, J. R. Transient Optical Studies of Interfacial Energetic Disorder at Nanostructured Dye-Sensitised Inorganic/Organic Semiconductor Heterojunctions. *ChemPhysChem* 4, 89–93 (2002).
43. Bisquert, J., Palomares, E. & Quiñones, C. Effect of energy disorder in interfacial kinetics of dye-sensitized solar cells with organic hole transport material. *J. Phys. Chem. B* (2006).
44. Bach, U. Solid-state dye-sensitized mesoporous TiO₂ solar cells. - EPFL Thesis n°2187. 1–168 (2000).
45. Boschloo, G. Photoinduced absorption spectroscopy of dye-sensitized nanostructured TiO₂. *Chem. Phys. Lett.* 370, 381–386 (2003).
46. Ardo, S. & Meyer, G. J. Direct Observation of Photodriven Intermolecular Hole Transfer across TiO₂ Nanocrystallites: Lateral Self-Exchange Reactions and Catalyst Oxidation. *J. Am. Chem. Soc.* 1498–1507 (2010).

CHAPTER 4

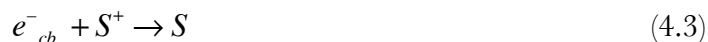
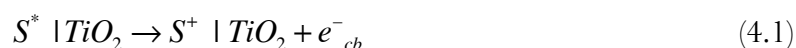
Effect of post-treatment of TiO₂ films by TiCl₄ in solid-state dye-sensitized cells

This chapter is adapted from the following publication: *Effect of post-treatment of titania mesoscopic films by TiCl₄ in solid-state dye-sensitized solar cells: A time-resolved spectroscopy study*, Marchioro, A., Dualeh, A., Punzi, A., Grätzel, M., Moser, J.-E., J. Phys. Chem. C, **2012**, *116*, 26721-26727. Post-treatment of mesoporous TiO₂ films using TiCl₄ solutions is commonly applied during the fabrication of solid-state dye-sensitized solar cells (ssDSCs), as this procedure improves the performance of the photovoltaic device. In this work, the effect of TiCl₄ treatment upon the charge carrier dynamics was investigated in ssDSCs. Kinetic studies, carried out using femtosecond and nanosecond transient absorption spectroscopy, showed that a biphasic electron transfer is observed, for both treated and non-treated films, whose kinetics is not significantly affected by the surface modification step. However, hole injection in the hole transport material (HTM) *spiro*-MeOTAD and charge recombination were found to be markedly slower in TiCl₄-treated films. These findings are rationalized by a model describing the interaction at the interface between TiO₂, the dye and *spiro*-MeOTAD. Results emphasize the importance of controlling the contact a between the HTM and the sensitized semiconductor oxide network.

4.1 Introduction

Solid-state dye-sensitized solar cells (ssDSCs), first reported in 1998 by Bach et al.,¹ are a promising alternative to conventional dye-sensitized cells (DSCs), as they circumvent potential problems of spilling and corrosion related to liquid electrolytes. Nowadays, systems based on solid organic hole transport materials (HTM) in conjunction with molecular dye-sensitizers reach 7.2% power conversion efficiency.² Compared to electrolyte-based DSCs with certified power conversion efficiencies of 12 %, ³ there is still some room for performance improvement.

The mechanistic processes in ssDSCs have been discussed in Chapter 3 and will be briefly reminded here. Following light excitation of the molecular sensitizer, an electron is injected in the conduction band (CB) of TiO₂ and can be extracted to generate a current in an external circuit (Equation (4.1)). Regeneration of the sensitizer is ensured by hole injection into the HTM, which has been shown in Chapter 3 to occur on the ps to ns timescale (Equation (4.2)). Undesirable back reactions can occur when electrons in the conduction band (e^-_{cb}) either recombine with some oxidized dye molecules (S^+), which did not inject holes sufficiently fast because of poor contact with the HTM, or directly with the oxidized HTM (Equations (4.3) and (4.4)). These recombination reactions are usually slower than forward electron transfer processes and take place in the μ s timescale. Reductive quenching of the dye's excited state by the HTM is also a pathway that needs in principle to be addressed in these systems (Equation (4.5)).⁴



As the DSC working principle relies on kinetic competition between forward charge transfer and recombination processes, the kinetics of hole and electron transfer reactions following light excitation must be understood in order to overcome the origin of the limitations in ssDSCs. Despite a large research effort aimed at improving the efficiency of

these solid-state devices, up to now only few studies concerning the mechanistic processes occurring in the system have been reported.

The hole mobility and the pore wetting/filling appear to be key parameters controlling charge separation efficiency and have been reviewed in Chapter 3. As the accumulation of holes at the interface would lead to increased recombination and prevent further hole injection from the dye, a good hole mobility in the HTM is needed and so far this is practically achieved by the use of various dopants.^{2,5,6} The other main issue is related to the contact between adsorbed dye molecules and the hole transport material:⁷⁻⁹ As it has been discussed in the previous chapter, when the contact with the HTM is inhomogeneous and/or incomplete, the hole will not be efficiently transferred and transported away from the interface. These two parameters are interconnected and related to the way the HTM has infiltrated the TiO_2 mesoporous structure, thus they strongly depend on the morphology and thickness of the film. Therefore the way the TiO_2 film is prepared must be carefully considered. Recently, new TiO_2 architectures have been tested to maximize the penetration of the HTM and this field is currently under investigation.¹⁰ On another hand, post-treatment of the surface of mesoporous titania films constituted of sintered spherical nanoparticles applied by bath deposition of TiO_2 from TiCl_4 aqueous solutions is routinely done in DSCs fabrication, as it markedly improves their photovoltaic efficiency and decreases recombination.^{11,12} This surface post-treatment of TiO_2 nanocrystalline anodes is indeed expected to increase the necking between nanoparticles and fill possible cracks in the film.¹³ The main effect observed in liquid DSCs is an enhancement of the photocurrent associated with a downward shift of the conduction band edge energy level. Sommeling et al. reported a complete work hypothesizing an effect of TiCl_4 on electron injection after ruling out a possible implication in electron transport and improved dye loading.¹¹ At this point, however, no systematic study on the effect of TiCl_4 treatment on solid-state devices has been performed. As the wetting of the surface with the HTM is critical for these devices, it is even more important to understand how surface treatments influence the morphology of the semiconductor film and affect the dynamics of electron transfer processes at the interface.

Here we report on the effect of TiCl_4 treatment upon the kinetics of charge transfer in ssDSCs studied by time-resolved transient absorption spectroscopy (TAS). By monitoring transient signals over a wide time range spanning from femtoseconds to milliseconds, TAS represents a powerful method to investigate the mechanistic processes occurring in the

photovoltaic device. Charge separation and charge recombination pathways in ssDSCs were examined in presence or absence of TiCl_4 post-treatment. Here, we show that adding this specific fabrication step affects the kinetics of processes in solar cells drastically, and that these changes are related to one of the bottleneck parameters of ssDSCs, i.e. the contact between the dye and the HTM *spiro*-MeOTAD. In a first part, we investigated the impact of TiCl_4 treatment on electron injection dynamics. Then, the effect on hole injection of different TiCl_4 treatment procedures was determined systematically. Beside the hole injection reaction (Equation 2), the competing back reaction of conduction band electrons (e^-_{cb}) with the oxidized form of the HTM (Equation 4) in treated and non-treated films was investigated in order to provide a complete picture of the kinetic competition in the system.

4.2 Methods

4.2.1 Samples preparation

The samples for the measurements presented in this chapter were prepared by Amalie Dualeh (LPI, EPFL). Nanocrystalline mesoporous 2.0-2.5 μm -thick TiO_2 films were prepared by screen-printing an aqueous paste onto glass microscope slides and sintering at a temperature of 500°C (average particle size 23 nm, average pore size 32 nm, approx. porosity 0.68). The samples treated by TiCl_4 were prepared as follows: the TiO_2 films were immersed in the dark in 20 mM aqueous titanium tetrachloride solution at either 70°C for 30 min or room temperature (RT) for 6 hours, prior to sintering at 500°C for 30 min. These two treatments influenced the morphology of the initially prepared mesoporous TiO_2 film, although not in a similar way. SEM pictures of TiO_2 compact films, which were not used for the kinetic studies, are presented in section 4.3.2 and show how 70°C treatment formed a conformal layer over the TiO_2 sintered nanoparticles, while RT treatment formed an additional layer including the nucleation of small islands.

Z907 complex (*cis*-bis(isothiocyanato)(2,2'-bipyridyl-4,4'-dicarboxylato)(4,4'-di-nonyl-2'-bipyridyl) Ru^{II}) was used as a dye sensitizer in this study.¹⁴ Sensitization of mesoporous TiO_2 was achieved by immersing the films overnight in a 0.3 mM Z907 solution in a mixture (1:1) of tBuOH and MeCN solvents. Samples infiltrated by *spiro*-MeOTAD HTM were prepared in an argon glovebox following a standard procedure to avoid any oxygen or moisture contact. *Spiro*-MeOTAD (Merck, KGaA) was dissolved in 400 μl

chlorobenzene at a concentration of 180 mg/ml by heating for 30 min at 60°C. Lithium bis (trifluoromethylsulfonyl)imide (LiTFSI) and 4-tert-butylpyridine (tBP) were added as follows: tBP was purified before use and 7 μl of this compound were added to the chlorobenzene solution to yield a concentration of 0.12 M tBP. 17 mg of LiTFSI were predissolved in 100 μl acetonitrile and 15 μl of this solution were added to the chlorobenzene solution to yield a concentration of 0.02 M LiTFSI. 40 μl of *spiro*-MeOTAD solution was deposited onto the sensitized substrates and allowed to infiltrate for 30 s in order to maximize the penetration of the HTM prior to spin coating for 30 s at 2000 rpm. After overnight evaporation of residual chlorobenzene, cells were sealed with Surlyn[®] (DuPont) cast polymer film and cover glass. Reference samples, containing no hole transport material, were covered with a solution of propylene carbonate with LiTFSI and tBP dissolved at the same concentration as the solution prepared for *spiro*-MeOTAD-infiltrated samples.

4.2.2 Nanosecond flash photolysis

Transmission-mode TAS experiments were conducted using a frequency-tripled, Q-switched Nd:YAG laser (Continuum, 20 Hz repetition rate) pumping an optical parametric oscillator (OPO-355, GWU). The output wavelength of the OPO was tuned to $\lambda = 590$ nm (7 ns pulse duration). The sample was set at a 60° angle with respect to the excitation laser beam. The fluence of the excitation light beam was attenuated to less than 40 $\mu\text{J}/\text{cm}^2$ at the sample in order to inject less than 2 electrons/nanoparticle on the average per pulse. This ensures that no significant shift in the TiO_2 Fermi level occurs as a result of a larger injected electrons population. The cw probe light from a Xe arc lamp was passed through various optical elements, the sample, and a monochromator ($\lambda_{\text{probe}} = 1000$ nm) before being detected by a fast photodiode. Averaging over at least 1000 laser shots was necessary to get satisfactory signal/noise ratios.

4.2.3 Femtosecond transient absorption

The setup is described in details in Chapter 2. Briefly, a Ti:Sa amplified femtosecond laser (CPA-2001, Clark-MXR) was used as a source. Half of the source intensity was used for pumping two non-collinear phase-matched optical parametric amplifiers (NOPA's), allowing for the generation of monochromatic pump and probe beams. At 590 nm pump

wavelength, typical energies of 8 μJ per pulse were obtained. The probe NOPA allowed the generation of a near-IR beam, with $\lambda_{\text{probe}} = 840$ nm and pulse energies of 1.5 μJ . The output pulses of the NOPAs were compressed by pairs of SF10 prisms, down to ca. 50 fs duration. The pump beam was chopped at half the repetition frequency of the pulsed laser source. The change in transmittance of the sample, i.e. change in intensity of the probe beam, was measured by a photodiode (Nirvana detector, New Focus, model 2007) placed after the sample and protected by cut-off filters to avoid any scattered light from the pump. The low-amplitude signal was extracted by a lock-in amplifier (SR-830, Stanford Research) referenced to the chopper placed in the pump beam. To ensure isotropic excitation of the sample, the pump polarization was set at magic angle (54.7°) relative to the probe pulse with a $\lambda/2$ waveplate. The typical fluence of the pump on the sample was low ($230 \mu\text{J}/\text{cm}^2$ per pulse, this should correspond, with a transmittance of 0.66 of the sample, to approximately 8 injected electrons/ TiO_2 nanoparticle). A lens allowed tuning the size of the pump beam before the sample to both decrease the fluence and allow for complete overlap of the probed spot area. Temporal overlap between the pump and probe pulses at the sample position was measured with a Kerr gating technique and gave typical instrument response function (IRF) of 120 fs.

4.2.4 Femtosecond transient absorption data treatment

The procedure for the fitting of the femtosecond TA signals is described herein. Electron injection was fitted with a model described elsewhere,^{15,16} using the convolution of one Gaussian with two exponentials, the second exponential being fixed ($\tau = 10 \mu\text{s}$). For hole injection, a specific model was derived, allowing a correct description of the TAS signals by isolating the contribution of the dye regeneration from the electron injection, as in presence of *spiro*-MeOTAD these two processes occur on a very similar timescale. Furthermore, as small differences in the kinetics of electron injection were noticed in the TiCl_4 treated samples with respect to non-treated samples, this model also accounts for this factor.

The probe wavelength, 840 nm, was chosen in order to observe the oxidized state of the dye with little contribution from the excited state.¹⁶⁻¹⁸ However this contribution cannot be totally neglected and thus the extinction coefficient of the excited state will be discussed further on. Past work on the kinetics of hole injection¹⁹ probed the rise of the oxidized state of the HTM. In this work, we decided to probe the rise and decrease of the oxidized

dye, in order to take into account any eventual dye that would not be in contact with the HTM and thus, would not inject its hole. This could not be probed by looking at the rise of the oxidized state of the HTM, as it has been explained in Chapter 3. Ideally, no contribution for the HTM oxidized state is desired in order to observe the sole contribution of the oxidized dye. However, in the spectral region of oxidized dye absorption, this requirement could not be fulfilled and the data treatment must take into account a minimal contribution by the oxidized state of the HTM. Additionally, the absorption of the electrons in the same spectral region has to be addressed as well. The current model does not address the issue of reductive quenching of the excited state of the dye by the HTM.

Determination of the extinction coefficients

The extinction coefficients of all the species present at 840 nm were determined. Z907 extinction coefficient was extracted by nanosecond flash photolysis experiments of Z907 | TiO₂ samples, covered with an inert solvent, where the amplitude of the signal from oxidized dye at 840 nm was compared to the amplitude of the bleaching signal from the ground-state species. In the microsecond timescale of the experiment, no contribution from the excited state of the dye was expected and thus the extinction coefficient corresponds to species present after electron injection. Using the extinction coefficient of the ground state species reported at 526 nm ($\epsilon_S = 1.2 \cdot 10^4 \text{ M}^{-1} \text{ cm}^{-1}$),²⁰ we could calculate an extinction coefficient value of $6.7 \cdot 10^3 \text{ M}^{-1} \text{ cm}^{-1}$, corresponding to the extinction coefficient of the oxidized species plus the corresponding free electrons in the conduction band that have broad absorption spectra in the IR. From the same flash photolysis measurements probing at longer wavelengths and based on the literature,^{21,22} we could estimate this value for the electrons as being approximately $\epsilon_e = 1.3 \cdot 10^3 \text{ M}^{-1} \text{ cm}^{-1}$, leading to a value of $\epsilon_{S^+} = 5.4 \cdot 10^3 \text{ M}^{-1} \text{ cm}^{-1}$ for the oxidized species alone. We further assume for the purpose of this analysis that the extinction coefficient of the electrons is independent of the concentration. This is not the case for strong accumulation conditions,²³ but the laser intensities used in the femtosecond study should not exceed 8 electrons/TiO₂ nanoparticle.

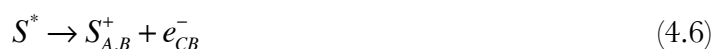
The extinction coefficient of the first oxidized form of *spiro*-MeOTAD, formed by regeneration of the oxidized dye, is also weakly absorbing at this wavelength, with an extinction coefficient of $\epsilon_{D^+} = 8.5 \cdot 10^2 \text{ M}^{-1} \text{ cm}^{-1}$ as determined by NIR absorption of the

chemically oxidized form, in agreement with previously measured values.^{24,25} To the best of our knowledge, the extinction coefficient of the excited state of the dye (denoted ϵ_{S^*}) was not reported clearly in the literature. For the purpose of this quantitative model, we thus tried to extract an approximate value for the extinction coefficient of the excited state species. From data published in Tachibana's thesis and previous reports,^{17,26} the relative amplitude of the excited state with respect to the signal of the oxidized species and the electrons is 33% of a signal constituted by oxidized state and electrons, i.e. an absorption coefficient of roughly $\epsilon_{S^*} = 2.2 \cdot 10^3 \text{ M}^{-1}\text{cm}^{-1}$. Hence, on a total signal of oxidized dye S^+ , excited state S^* , electrons e^- and oxidized HTM D^+ ($\epsilon_{\text{tot}} = 5400 + 2200 + 1300 + 850 = 9750 \text{ M}^{-1} \text{ cm}^{-1}$), we have 55% contribution from the oxidized state, 23 % contribution from the excited state, 13% for the electrons and 9% coming from the oxidized HTM. These values will allow a correct weighting of the different contributions in the signal.

Differential model and fitting equation

As the overall signal contains more than one contribution, it was necessary to separate the temporal evolution of each of these contributions. For this purpose, differential equations were used to describe the temporal evolution of all species. All the subpicosecond processes and the instrument response function were not taken into account in the kinetic model and considered as a step function, as the processes of interest were much slower. Furthermore the injection efficiency is considered to be 100%.

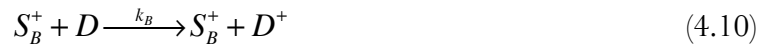
After electron injection, the following process is hole injection into the HTM. A multiexponential process has been observed and previously described by Bach et al.,¹⁹ as well as reported in Chapter 3. This was ascribed to a kinetic inhomogeneity, i.e. different types of populations. In our model, we consider a first type of population (A) that represents the oxidized dye molecules in close contact with the HTM; the rate constant for hole injection will be named k_A . A second type of population (B), represents the oxidized dye molecules at longer distances from the HTM, thus subjected to hole hopping to transfer their hole.²⁷ We made the assumption that statistically these distances will average giving rise to a unique rate constant, namely k_B . The ground state species, denoted S, can give rise after injection to either S_A^+ or S_B^+ . Considering the following reactions:





Equation (4.6) describes the instantaneous rise within the laser pulse that is completed at time $t=0$ and is described by a step-function as discussed above. Equations (4.7) and (4.8) take into account the slower injection part respectively for A and B populations. The time constant of this process, k_1 , can readily be extracted from fitting a reference of $\text{Z907} | \text{TiO}_2$ and inert solvent. The time constant k_1 remains the same for both A and B populations, since the electron injection is not related with the type of dye (in contact or not) with the HTM.

The regeneration of the different types of dye populations by HTM is given by the rate constants k_A and k_B in (4.9) and (4.10):



Thus the temporal evolution of the species can then be described by the following equations:

$$\frac{dS^*}{dt} = -2k_1 S^* \quad (4.11)$$

$$\frac{dS_A^+}{dt} = k_1 S^* - k_A S_A^+ \quad (4.12)$$

$$\frac{dS_B^+}{dt} = k_1 S^* - k_B S_B^+ \quad (4.13)$$

$$\frac{dD^+}{dt} = k_A S_A^+ + k_B S_B^+ \quad (4.14)$$

with $S_A^+(t)$ and $S_B^+(t)$ being the concentrations of the oxidized dye, respectively for populations A and B, and $D^+(t)$ being the concentration of the oxidized HTM. The initial conditions are $S^*(t=0) = S_0^*$, $S_A^+(t=0) = S_{A,0}^+$, $S_B^+(t=0) = S_{B,0}^+$ and $D^+(t=0) = D_0^+ = 0$.

The temporal evolution of the electrons must also be considered, and once they are formed, on the timescale of interest, we can consider that their concentration remains constant (recombination processes are much slower).

$$\frac{de^-}{dt} = -\frac{dS^*}{dt} = +2k_1S^* \quad (4.15)$$

with $e_0^- = S_{A,0}^+ + S_{B,0}^+$. The system of differential equations (4.11), (4.12), (4.13), (4.14), and (4.15) can be solved in Mathematica (v.8.0.4.0).

Once the temporal evolution of the concentrations is found, the transient absorbance signal (the change in absorbance with and without laser pulse) can be described by weighting each concentration with the corresponding *relative* extinction coefficient, following the Beer-Lambert law:

$$\Delta A = A_{pump} - A_{no\ pump} = \sum_i \varepsilon_i \cdot c_i(t)_{pump} - \sum_i \varepsilon_i \cdot c_i(t)_{no\ pump} \quad (4.16)$$

As at this wavelength, the ground state species do not absorb, the second term of Equation (4.16) is zero and the overall equation is:

$$\begin{aligned} \Delta A = & e^{-2k_1t} \varepsilon_{S^*} S_0^* + \varepsilon_{electrons} (S_0^* - e^{-2k_1t} S_0^*) + \varepsilon_{electrons} (S_{A,0}^+ + S_{B,0}^+) \\ & + \frac{1}{(2k_1 - k_A)(2k_1 - k_B)} e^{-2k_1t - k_{A^t} - k_{B^t}} \varepsilon_{D^+} \cdot (-2e^{2k_1t + k_{A^t}} k_1^2 S_0^* - 2e^{2k_1t + k_{B^t}} k_1^2 S_0^* \\ & + 4e^{2k_1t + k_{A^t} + k_{B^t}} k_1^2 S_0^* + e^{2k_1t + k_{A^t}} k_1 k_A S_0^* + e^{k_{A^t} + k_{B^t}} k_1 k_A S_0^* - 2e^{2k_1t + k_{A^t} + k_{B^t}} k_1 k_A S_0^* \\ & + e^{2k_1t + k_{B^t}} k_1 k_B S_0^* + e^{k_{A^t} + k_{B^t}} k_1 k_B S_0^* - 2e^{2k_1t + k_{A^t} + k_{B^t}} k_1 k_B S_0^* - e^{k_{A^t} + k_{B^t}} k_A k_B S_0^* \\ & + e^{2k_1t + k_{A^t} + k_{B^t}} k_A k_B S_0^* - 4e^{2k_1t + k_{B^t}} k_1^2 S_{A,0}^+ + 4e^{2k_1t + k_{A^t} + k_{B^t}} k_1^2 S_{A,0}^+ + 2e^{2k_1t + k_{B^t}} k_1 k_A S_{A,0}^+ \\ & - 2e^{2k_1t + k_{A^t} + k_{B^t}} k_1 k_A S_{0,A}^+ + 2e^{2k_1t + k_{B^t}} k_1 k_B S_{A,0}^+ - 2e^{2k_1t + k_{A^t} + k_{B^t}} k_1 k_B S_{A,0}^+ \\ & - e^{2k_1t + k_{B^t}} k_A k_B S_{A,0}^+ + e^{2k_1t + k_{A^t} + k_{B^t}} k_A k_B S_{A,0}^+ - 4e^{2k_1t + k_{A^t}} k_1^2 S_{B,0}^+ + 4e^{2k_1t + k_{A^t} + k_{B^t}} k_1^2 S_{B,0}^+ \\ & + 2e^{2k_1t + k_{A^t}} k_1 k_A S_{B,0}^+ - 2e^{2k_1t + k_{A^t} + k_{B^t}} k_1 k_A S_{B,0}^+ + 2e^{2k_1t + k_{A^t}} k_1 k_B S_{B,0}^+ \\ & - 2e^{2k_1t + k_{A^t} + k_{B^t}} k_1 k_B S_{B,0}^+ - e^{2k_1t + k_{A^t}} k_A k_B S_{B,0}^+ + e^{2k_1t + k_{A^t} + k_{B^t}} k_A k_B S_{B,0}^+) \\ & + \varepsilon_{S^+} \left(-\frac{e^{-2k_1t - k_{A^t}} (-e^{2k_1t} k_1 S_0^* + e^{k_{A^t}} k_1 S_0^* - 2e^{2k_1t} k_1 S_{A,0}^+ + e^{2k_1t} k_A S_{A,0}^+)}{2k_1 - k_A} \right. \\ & \left. - \frac{e^{-2k_1t - k_{B^t}} (-e^{2k_1t} k_1 S_0^* + e^{k_{B^t}} k_1 S_0^* - 2e^{2k_1t} k_1 S_{B,0}^+ + e^{2k_1t} k_B S_{B,0}^+)}{2k_1 - k_B} \right) \end{aligned} \quad (4.17)$$

where the extinction coefficients are listed above. Equation (4.17) can be used as a fit function in Igor (v. 6.00) with the corresponding initial guesses on $S_{A,0}^+$ and $S_{B,0}^+$, and the

relative extinction coefficients as fixed parameters. As previously mentioned, the subpicosecond processes and the instrument response function were taken as a step function in this analysis, as the processes of interest were much slower, thus the fits start at $t = 1$ ps. S_0^* and k_1 were both estimated from the reference of Z907|TiO₂ with inert solvent and taken as fixed parameters. k_B , the slowest exponential, needed to be sometimes fixed (usually $3 \cdot 10^7$ s⁻¹). Thus on a total of ten parameters, seven are fixed or constrained.

Estimation of the S_0^* parameter

The initial population in the excited state can be extracted from a fitting a reference measurement of Z907|TiO₂, in absence of *spiro*-MeOTAD. It is calculated considering only the growth after the subpicosecond, ultrarapid injection. The amplitude of this slow part, denoted ΔA_{slow} and shown in Figure 4.1, is given by the following equation:

$$\Delta A_{slow} = \Delta A_{S_f^+} + \Delta A_{e_f^-} = \epsilon_{S^+} S_f^+ + \epsilon_{e^-} e_f^- \quad (4.18)$$

and $S_0^* = S_f^+ = e_f^-$, where S_f^+ is the final concentration of oxidized dye and e_f^- the final concentration of electrons, corresponding to the species produced in the slow part.

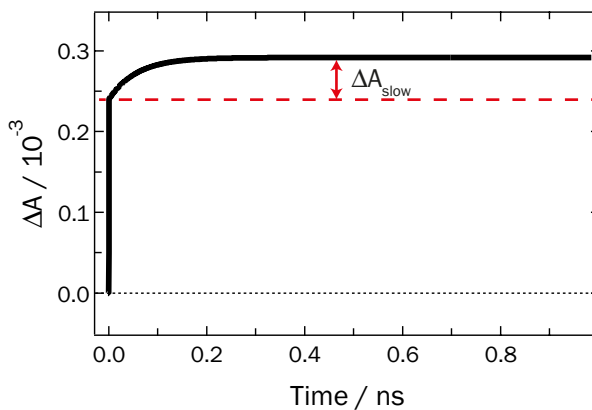


Figure 4.1 Scheme showing the amplitude of the slow part ΔA_{slow}

Thus:

$$S_0^* = S_f^+ = \frac{\Delta A_{S_f^+}}{\epsilon_{S^+}} = \frac{\Delta A_{slow} - \Delta A_{e_f^-}}{\epsilon_{S^+}} = \frac{\Delta A_{slow} - \epsilon_{e^-} e_f^-}{\epsilon_{S^+}} = \frac{\Delta A_{slow} - \epsilon_{e^-} S_0^*}{\epsilon_{S^+}} \quad (4.19)$$

$$S_0^* = \frac{\Delta A_{slow}}{(\epsilon_{S^+} + \epsilon_{e^-})} \quad (4.20)$$

In this case, the only species present are S^* , S^+ and e^- . The relative extinction coefficients, for the excited state absorption, the oxidized state and the electrons, are 61%, 24% and 15%. The relative initial excited state concentration becomes:

$$S_0^* = \frac{\Delta A_{slow}}{(0.61 + 0.15)} \quad (4.21)$$

This allows an estimation of the initial concentration of excited state from the reference and thus can be put as a constrained parameter in the fit equation (4.17).

4.3 Results

Fs and ns TAS measurements were performed on samples prepared with and without TiCl_4 treatment. Z907 dye was used throughout all the study. Dye photoexcitation was carried out at 590 nm, and the dye oxidized state's transient absorption probed at 840 nm, as explained in section 4.2.4.

4.3.1 Absorption spectra

Absorption spectra of Z907 | TiO_2 films and Z907 + *spiro*-MeOTAD | TiO_2 films are reported here, together with the absorbance of the corresponding solutions, obtained from desorption of the dye in a basic solution. The UV-vis-near IR spectrum was measured with a Lambda 950 spectrophotometer (Perkin-Elmer) equipped with a 60 mm integrating sphere (LabSphere). A total transmission spectrum (the direct transmission plus the scattered transmission) was measured for the films measuring between 2 and 2.5 μm . Solutions were measured in normal transmission mode, without the integrating sphere. The RT treatment and the 70°C treatment being very similar, only the results for the 70°C treatment are presented here.

Absorption spectra for Z907 | TiO_2

The absorption spectra derived from the total transmission of Z907 adsorbed on the 70°C treatment film and the non-treated film are shown in Figure 4.2. They both show a maximum at 525 nm, accordingly to the values reported in the literature.²⁰

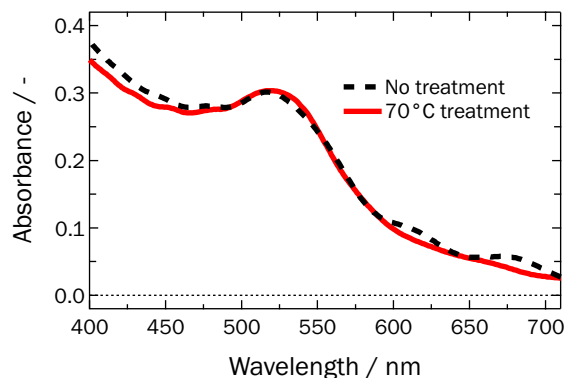


Figure 4.2 Absorption spectra of Z907 | TiO_2 films

Non-treated film (dashed black line) and 70°C treated film (red plain line).

Absorption spectra for desorbed Z907

In order to quantitatively estimate the difference in dye loading on a treated and non-treated film, dye desorption experiments, as already described by Sommeling et al.¹¹ were performed on the same films used for the integrating sphere measurements. First, the average thickness of each film was measured with profilometer (Alpha-Step 500 profilometer, KLA-Tencor) as shown in Table 4.1. The area of all the films was identical.

Table 4.1 Thickness of the non-treated and 70°C treated TiO_2 films before dyeing

Sample	Average thickness (μm)
No treatment	1.96
70°C treatment	2.47

Then, after usual dyeing procedure, a solution (1:1) NaOH 0.1 M/ H_2O was prepared in order to desorb the dye from the TiO_2 surface. The solutions were then measured with the standard detector of the Lambda 950 spectrophotometer. The spectra were slightly blue-shifted, indicating a partial deprotonation of the dye. To obtain the exact dye loading, the absorbance of the desorbed solutions was divided by the average film thickness (Figure

4.3). As expected, the difference was small, in the order of 4%, this confirming the values reported in Sommeling's paper.

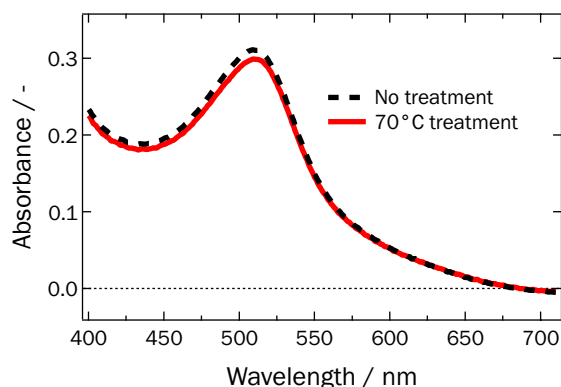


Figure 4.3 Absorption spectra of solutions of desorbed Z907

As obtained from the desorption of a non-treated film (dashed black line) and 70°C treated film (red plain line). The absorbance was divided by the corresponding film thickness indicated in Table 4.1.

Absorption spectra of Z907+spiro-MeOTAD | TiO₂

The spectra of the samples of films with *spiro*-MeOTAD shows the same absorption peak for the dye as well as a supplementary feature at 400 nm – indicative of presence of unoxidized *spiro*-MeOTAD (Figure 4.4). A small peak at 1000 nm shows the presence of a minimal quantity of oxidized *spiro*-MeOTAD, probably induced by the exposition to oxygen.

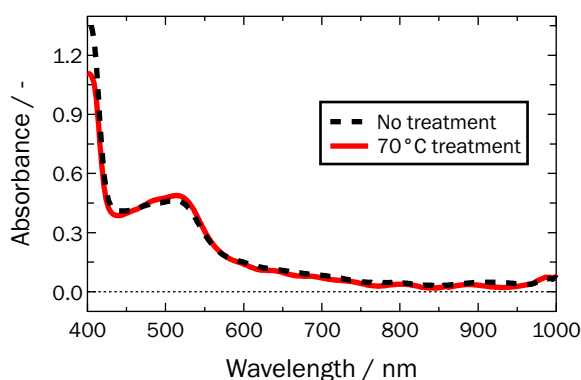


Figure 4.4 Absorption spectra of Z907+spiro-MeOTAD | TiO₂ films

Non-treated film (dashed black line) and 70°C treated film (red plain line).

4.3.2 SEM pictures

SEM pictures were taken by Amalie Dualeh (LPI, EPFL). A difference between the TiO₂ underlayers with and without TiCl₄ treatment can be observed on the SEM pictures. When compared to a non-treated underlayer (Figure 4.5a), the 70°C treatment (Figure

4.5b) shows formation of a structured layer over the TiO_2 sprayed layer, that appears to be conformal. With RT treatment (Figure 4.5c), the formation of an additional layer includes the nucleation of small islands (white dots) on the compact TiO_2 layer. In both cases, more material is deposited over the substrate, inducing a change in the surface structure and properties that, in the case of the mesoporous TiO_2 structure will most likely modify the contact between TiO_2 nanoparticles and the HTM.

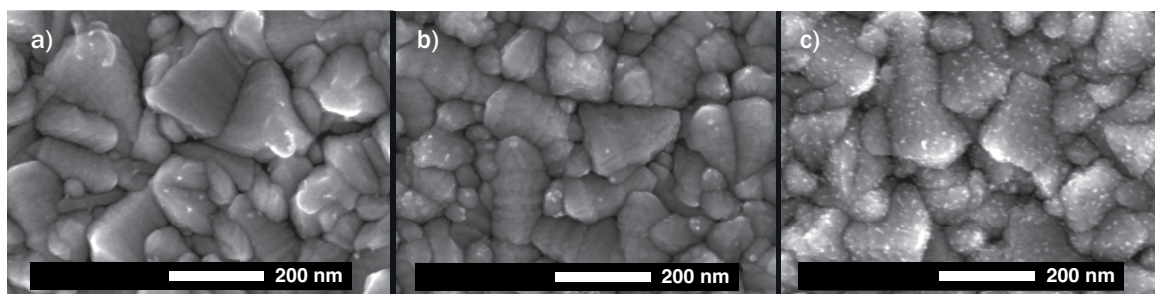


Figure 4.5 SEM pictures of the TiO_2 underlayer with different treatments

a) Non-treated TiO_2 underlayer, b) 70°C treated TiO_2 underlayer and c) RT treated TiO_2 underlayer

4.3.3 Electron injection dynamics

At first, the influence of TiCl_4 treatment on electron injection dynamics from Z907 was monitored. Films of Z907/ TiO_2 were prepared as described in the experimental section, but no *spiro*-MeOTAD was deposited. Electron injection has been reported to take place in the femtosecond time scale, provided that dye adsorption on the surface is performed under certain conditions.²⁸⁻³¹ TAS measurements over a time span of 1 or 2 ns were conducted on Z907 sensitized TiO_2 samples with and without TiCl_4 treatment (Figure 4.6). The samples were covered with propylene carbonate (PC) as an inert solvent. Measurements were performed both with neat PC, as well as with a solution of PC containing LiTFSI and tBP at the same concentrations as used for the preparation of the *spiro*-MeOTAD solution, and no noticeable difference was observed within the two sets of samples. No difference was also observed between different TiCl_4 treatments (70°C treatment or RT treatment). At 840 nm, the observed signal corresponds mainly to the formation of the dye oxidized state (S^+) by electron injection in the TiO_2 as explained before. This dye's oxidized state, in the absence of a redox mediator, has a lifetime of a few hundreds of microseconds. Thus on the timescale of the experiment, only the rise of the S^+ species signal can be detected, as it can be seen in Figure 4.6. Electron injection on non-treated films was found to take place predominantly in a sub-50 fs time scale, with a small

slower picosecond component (15%, 50 ps) being consistent with previous results.³⁰ A similar biphasic behavior was found in the case of the treated films, with a 60 ps component accounting for 20% of the total signal. This is also consistent with findings of Tiwana et al. who observed by terahertz measurements a biphasic charge injection with 50-70 ps component and no noticeable difference in charge injection for treated and non-treated samples.³² Samples were also measured with different fluences in order to ensure that the dynamics of electron injection is independent of the pump energy.

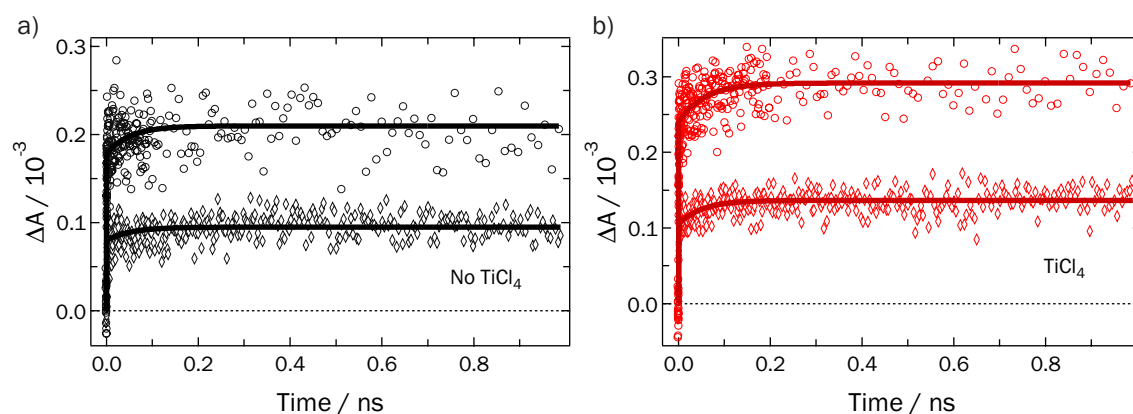


Figure 4.6 Time course of the transient absorption measured at 840 nm of samples following fs pulsed excitation at 590 nm

Signals mainly reflect the kinetics of appearance of the dye oxidized state S^+ and, therefore, of the electron injection process. a) Z907 | non-treated TiO_2 . Black circles: sample measured under an excitation fluence of $230 \mu\text{J}/\text{cm}^2$. Black diamonds: different sample measured at half the fluence. b) Z907 | TiCl_4 -treated TiO_2 at 70°C . Red triangles: sample measured under an excitation fluence of $230 \mu\text{J}/\text{cm}^2$. Red diamonds: different sample measured at half the fluence. Data were fitted with an analytical convolution function of a Gaussian instrument response and two exponentials (solid line).

4.3.4 Hole injection dynamics

The dye oxidized state S^+ signal of samples filled with *spiro*-MeOTAD HTM was monitored by probing its optical absorption at 840 nm as explained in 4.2.4. Typical transients are shown in Figure 4.7. The regeneration of the oxidized dye (Equation 2) was expected to occur on the ps-ns timescale¹⁹ and indeed a decrease in the dye oxidized signal can be observed over a range of 2 ns, very similarly to what observed in Chapter 3. At the probing wavelength of 840 nm, the observed signal includes contributions of the excited state, the oxidized state, the oxidized HTM and of conduction band electrons. Thus, it is hardly possible to extract quantitative kinetic information without a precise description of the time evolution of each species. A detailed model describing the time-dependence contribution of each species, weighted by the corresponding relative extinction coefficient, is derived in 4.2.4. As a brief reminder, the model considers two types of population of

oxidized dye, S_A^+ and S_B^+ , corresponding respectively to a dye population, A, where molecules are adsorbed in direct contact with the HTM and to a portion, B, of dye molecules not in direct contact with the HTM, and for which holes have to be transferred by lateral hopping until they reach the HTM.^{27,33} The fit equation derived with the model allowed obtaining quantitative values for the initial volumic concentrations on the probed spot and time constants for each species (respectively $S_{A,0}^+$ and k_A , $S_{B,0}^+$ and k_B) separated from the contributions of all the other absorbing species. Figure 4.7b) and c) shows transient absorption signals recorded in similar conditions with samples prepared with non-treated films. The fast component, with $k_A = 2.6 \cdot 10^9 \text{ s}^{-1}$ ($\tau_A = 380 \text{ ps}$) accounts for 52% of the total oxidized dye concentration, while the slow component $k_B = 2.6 \cdot 10^7 \text{ s}^{-1}$ ($\tau_B = 38 \text{ ns}$) accounts for 48% of the total oxidized dye concentration. Residues for all fits are presented in Figure 4.8.

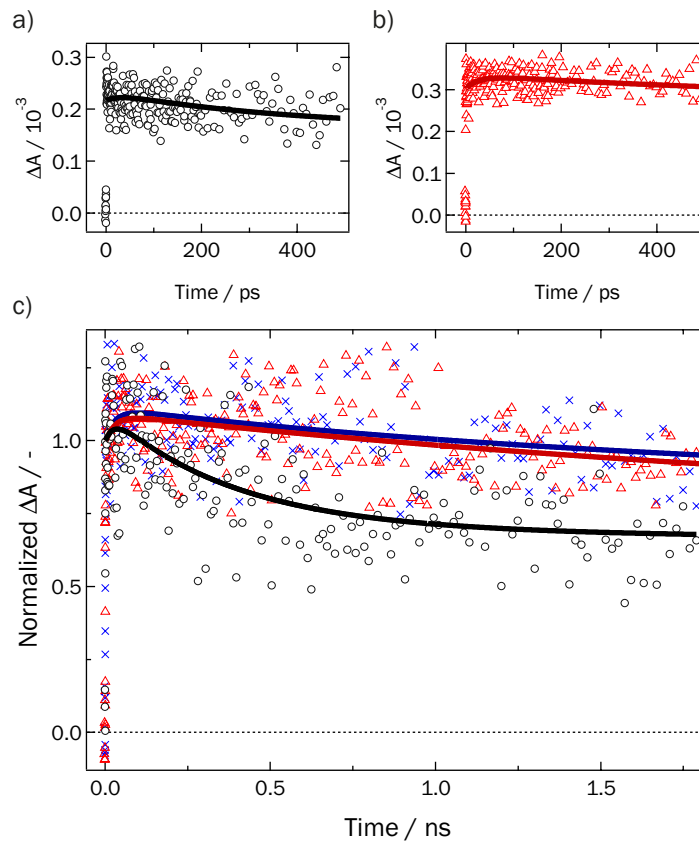


Figure 4.7 Hole injection dynamics probed at 840 nm following 590 nm fs pulsed excitation of dye-sensitized TiO_2 films

a) Z907 + *spiro*-MeOTAD | non-treated TiO_2 . b) Z907 + *spiro*-MeOTAD | TiCl_4 -treated TiO_2 at 70°C. c) Normalized absorbance changes of Figures a) (black dots) and b) (red triangles) are plotted together for direct comparison. Data obtained for a sample made of Z907 + *spiro*-MeOTAD | TiCl_4 -treated TiO_2 at RT are also shown (blue crosses).

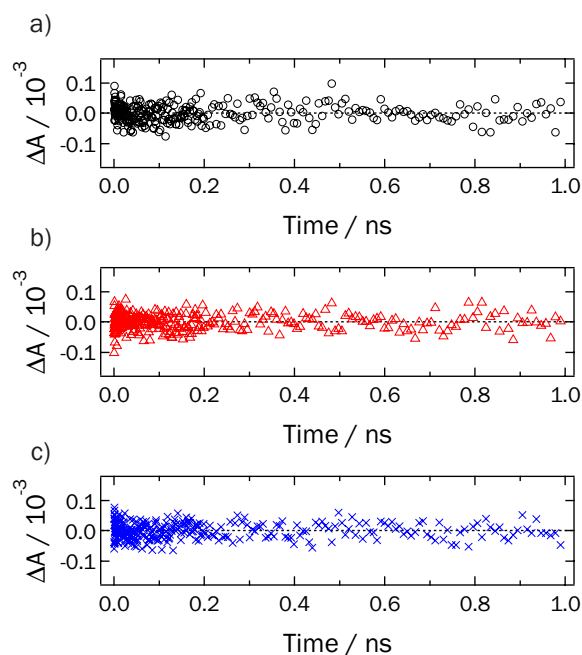


Figure 4.8 Residues of the fits presented in Figure 4.7

Residues of the fits of hole injection spectra monitored at 840 nm followed by excitation at 590 nm on a) Z907 + *spiro*-MeOTAD | non-treated TiO₂ (black dots), b) on Z907 + *spiro*-MeOTAD | 70°C treated TiO₂ (red triangles) and c) on Z907 + *spiro*-MeOTAD | RT treated TiO₂ (blue crosses).

4.3.5 Hole injection in TiCl₄-treated samples

Samples with different types of TiCl₄ treatment were prepared and hole injection dynamics was measured. Decrease of the dye oxidized state signal was observed to be slower in the case of both TiCl₄ treatments than with non-treated films (Figure 4.7). Similar to the previous case, the derived model provided an estimation of the proportion of the population A with respect to the population B without any contribution from the HTM absorption, the electrons, or the dye excited state. The fit equation derived also takes into account the small differences observed in the case of electron injection. Consequently it can be unambiguously determined if the observed decrease results from slower electron injection or if it is solely related to an effect due to different surface morphology. For a sample prepared with a TiCl₄-treated film, a fast component is still observable $k_A = 1.4 \cdot 10^9 \text{ s}^{-1}$, ($\tau_A = 710 \text{ ps}$), but this accounts for only 14% of the total oxidized dye concentration, while the slow component with $k_B = 5 \cdot 10^7 \text{ s}^{-1}$ accounts for 86% of the total oxidized dye concentration. This shows that the hole injection is markedly delayed when TiCl₄ treatment is implemented.

4.3.6 Hole injection with different TiCl_4 treatments

Empirical optimization of TiCl_4 treatment in our laboratory suggested that varying the conditions of the surface treatment leads to a change in the morphology of the film. In order to compare the effect of distinct types of TiCl_4 treatments and the related morphology of the TiO_2 films on the hole injection, samples with a different TiCl_4 treatment, done at 25°C for 6h, were tested. Electron injection on a Z907-sensitized TiO_2 film was first measured to extract the parameters needed for the fitting procedure, and it was found to be very similar to the previous 70°C TiCl_4 treatment. For samples Z907 + *spiro*-MeOTAD/ TiCl_4 -treated TiO_2 at RT, no noticeable difference for hole injection (Figure 4.7c) could be observed within the resolution of measurements. Fast components with $k_A = 8.1 \cdot 10^8 \text{ s}^{-1}$ ($\tau_A = 1.2 \text{ ns}$) and the slower one, $k_B = 5 \cdot 10^7 \text{ s}^{-1}$, accounted for 11% and 89% of the total oxidized dye concentration, respectively.

4.3.7 Charge recombination

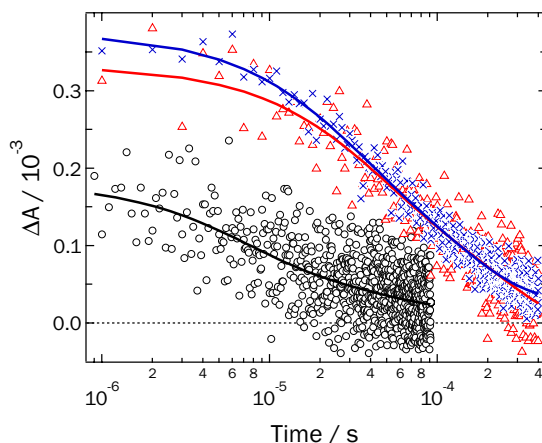


Figure 4.9 Charge recombination dynamics monitored at 1000 nm, for 590 nm excitation

Black dots represent Z907 + *spiro*-MeOTAD | non-treated TiO_2 , red triangles Z907 + *spiro*-MeOTAD | TiCl_4 -treated TiO_2 at 70°C and blue circles Z907 + *spiro*-MeOTAD | TiCl_4 -treated TiO_2 at RT. Experimental data points were fitted by double exponential decays (solid lines).

Charge recombination of oxidized *spiro*-MeOTAD with electrons in TiO_2 conduction band occurs on the μs timescale and can be monitored by flash photolysis technique. Measurements were performed on Z907 | *spiro*-MeOTAD samples prepared with and without TiCl_4 treatment. The dye was excited at 590 nm, and the *spiro*-MeOTAD oxidized state (HTM^+) was probed at 1000 nm, where the signal is mainly due to oxidized *spiro*-MeOTAD, with only a small contribution of conduction band electrons.³⁴ This

particular wavelength was chosen to exclude the contribution to the signal from possible remaining oxidized dye molecules. The decay of the absorption of HTM⁺ displayed in Figure 4.9 reflects the recombination of *spiro*-MeOTAD oxidized state species with injected conduction band electrons as described by Equation (4.4). A simple single exponential was not able to fit the decay kinetics. As excitation fluences were carefully limited to ensure that less than two electrons are injected per nanoparticle at a time, the observed complex kinetics could well indicate a kinetically inhomogeneous recombination mechanism. Non-treated films ($k_1 = 1.5 \cdot 10^5 \text{ s}^{-1}$ and $k_2 = 2.6 \cdot 10^4 \text{ s}^{-1}$) exhibit a faster recombination than samples treated according to the two different types of TiCl₄ application procedures ($k_1 = 2.8 \cdot 10^4 \text{ s}^{-1}$ and $k_2 = 4.3 \cdot 10^3 \text{ s}^{-1}$ for 70°C treatment and $k_1 = 4.2 \cdot 10^4 \text{ s}^{-1}$ and $k_2 = 7.8 \cdot 10^3 \text{ s}^{-1}$ for RT treatment). In order to exclude variation of the recombination rate due to a shift of the Fermi level caused by an increased dye loading and consequently an increased number of injected electrons per particle, the dye loading was determined by dye desorption experiments (refer to section 4.3.1). As already reported by Sommeling et al.,¹¹ the measured adsorbed dye surface concentration was found to be practically constant (with changes of the order of 4%). The difference observed between recombination rates cannot be ascribed, thus, to a different density of injected electrons.

4.4 Discussion

On the side of electron injection dynamics, this work confirms what was already observed using different techniques.^{12,32} No marked difference is observable in the kinetics of electron injection that could be ascribed to the surface treatment. Furthermore we cannot conclude on an effect of the treatment on the DOS of TiO₂. Here, the main interest of measuring electron injection is to determine a value for the biphasic injection to use as a parameter in the model developed for the hole injection.

Regarding hole injection, femtosecond TAS studies on ssDSCs were reported by Bach et al.¹⁹ They investigated the process of hole injection by monitoring the bleaching of the dye and the appearance of the oxidized state of the *spiro*-MeOTAD, corresponding to the hole injection from the dye to the HTM. As one of the main issues with ssDSC is partial pore filling that prevents part of the dye molecules to be in direct contact with the HTM, monitoring the signal of oxidized dye, instead of the one from oxidized *spiro*-MeOTAD, gives a direct measure of the fraction of the isolated dye molecules not in contact with the HTM, thus not being regenerated, at least not as fast as dye molecules in

direct contact to the HTM. On the other hand, when probing the appearance of oxidized *spiro*-MeOTAD, this information is missing and may underestimate the fact that part of the dye molecules in a segregated zone, not in contact with *spiro*-MeOTAD, will follow completely different kinetics. As discussed above, preliminary studies on hole injection in the absence of any TiCl_4 treatment showed that the dye oxidized state could be monitored at 840 nm with little contribution from the *spiro*-MeOTAD oxidized state – thus leading to the choice of this particular probe wavelength for the reported work.

In ssDSCs using *spiro*-MeOTAD, hole injection is a one-electron transfer process, unlike the case of liquid DSCs based on the I_3^-/I^- redox couple, where the oxidation of iodide implies a two-electron exchange.³¹ Hole injection in HTM is, thus, expected to be fast and indeed, the kinetic of dye regeneration is observed to take place in the ps-ns timescale. The experiments showed that 50% of the dye is regenerated in a timescale of a few hundreds of picoseconds, while the other half of dye is still present after 2 nanoseconds in its oxidized form. From extrapolation, the totality of the dye should be regenerated after a few tens of nanoseconds. This observation is in agreement with Bach's studies in 1999, where the appearance of the oxidized state of *spiro*-MeOTAD was monitored, and it was concluded that the multi-exponential kinetics arises from a distribution of separation distances between dye and HTM molecules. This is a further indication that with optimized conditions of *spiro*-MeOTAD deposition (spin coating, 180mg/ml, 65% pore filling fraction), nearly all dye molecules are able to transfer their hole to *spiro*-MeOTAD, via direct contact or via lateral hole hopping. We illustrate in Chapter 3 the effect of the pore filling fraction (PFF) on hole injection, showing that between 25% PFF and 65% PFF, the regeneration increases with increasing PFF. This confirms a direct mechanism of hole injection for dye directly in contact with *spiro*-MeOTAD, while some holes have to move laterally in order to attain the next *spiro*-MeOTAD molecule, thus explaining the slower part of the signal.

Having established the mechanism of hole injection in absence of TiCl_4 treatment, it was then possible to study the effect of TiCl_4 treatment on the same hole injection process. As pointed out by the results presented in Figure 4.7, hole injection is drastically slowed down by TiCl_4 treatment. A plausible hypothesis to explain this effect comes from a change in the morphology of the film observed as a result of a different necking between the particles, changing the pore size and the porosity. SEM pictures of the TiO_2 compact underlayer following the same type of TiCl_4 treatment the mesoporous TiO_2 film are presented in section 4.3.2 and show indeed that the TiCl_4 bath induces a surface

modification with deposition of additional material. In this sense, the penetration and/or wetting of the surface with *spiro*-MeOTAD could be more difficult after modification of the TiO₂ surface. This hypothesis is further supported by measurements carried out in the μ s timescale, where recombination of e^-_{cb} with oxidized *spiro*-MeOTAD is monitored. Charge recombination between injected electrons and *spiro*-MeOTAD shows a 10-fold decrease of rate constants for treated samples with respect to non-treated ones, both for the 70°C treatment and the RT treatment. This global decrease in both the hole injection and charge recombination processes rate could be well explained by a different penetration of *spiro*-MeOTAD into the pores and a different wetting of the surface, slowing down the two competing reactions. As the overall effect of TiCl₄ treatment on complete cells is a general increase in their efficiency, it is safe to assume that the decrease in hole injection kinetics is not as crucial for the system as the decrease in charge recombination kinetics. Increasing the recombination time constant for this unwanted back reaction markedly improves the performance of the system, and these measurements confirm that a major effort has to be invested in trying to minimize this loss pathway. Recent studies have shown evidence for differences in recombination kinetics for different types of TiO₂ facets.³⁵ Looking from a molecular picture, it is then worth noting that if the TiO₂ local facet and orientation of dye molecules at the surface is a parameter that has to be taken into account. This could well explain the difference observed in recombination kinetics and hole injection, as the contact with the oxidized hole transport material and the lateral hopping between dye molecules is most likely altered.

When comparing the two different TiCl₄ treatments (at 70°C and RT) on ps and μ s timescales, the following observation can be made: independently of which TiCl₄ treatment has been performed, hole injection is delayed in the same way with respect to a non-treated sample. As suggested by previous studies on the influence of PFF on the hole injection reported in Chapter 3, a noticeable difference in hole injection kinetics can be resolved only if the difference in PFF is greater than 10-20%. For small variations in PFF, as is assumed to be the case for samples prepared with the different TiCl₄ deposition methods, the change in hole injection dynamics must be too small to be observed within the sensitivity of our experiment.

While the effect of TiCl₄ treatment appears to be mitigated on the side of electron injection and, regarding hole injection, goes in an opposite direction from what is expected for a performing cell, charge recombination is slowed down substantially by the TiCl₄ treatment explaining the observed increase in cell performance. Interestingly, the

recombination of electrons and *spiro*-MeOTAD seems to be faster than the recombination of the electrons with the dye itself (usually a few hundreds of μ s). This could be an indication that *spiro*-MeOTAD contacts directly the surface in some parts of the pore leading to a preferential channel for recombination.

4.5 Conclusion

In conclusion, this study has focused on the effect of TiCl₄ treatment on both mechanisms of charge separation and charge recombination. TAS spectra of electron injection, hole injection and charge recombination have been recorded and a specific model was developed in order to treat the data obtained for hole injection from the oxidized dye to the HTM. This model allowed separating the contribution from the electrons, the oxidized HTM species and dye molecules that absorb in the same region of the spectrum. Our findings show that the kinetics of electron injection does not display a significant change upon TiCl₄ treatment. On the other hand, hole injection was found to be delayed by TiCl₄ treatment. This was rationalized by a different penetration/wetting of the pores by the HTM when deposited out of solution reducing the direct contact of dye and HTM. The most striking effect of this surface treatment was found to be on charge recombination being explained by the same rationale as the delayed hole injection. These findings are in good agreement with previous studies that already concluded that the effect of TiCl₄ treatment in liquid cells was mostly affecting charge recombination. Charge recombination in solid devices being a one-electron process, it is likely to compete efficiently with the overall charge separation. Therefore this work underlines the importance of controlling charge recombination with the HTM in order to improve photovoltaic devices performance.

4.6 References

1. Bach, U. *et al.* Solid-state dye-sensitized mesoporous TiO₂ solar cells with high photon-to-electron conversion efficiencies. *Nature* 395, 583–585 (1998).
2. Burschka, J. *et al.* Tris(2-(1H-pyrazol-1-yl)pyridine)cobalt(III) as p-type dopant for organic semiconductors and its application in highly efficient solid-state dye-sensitized solar cells. *J. Am. Chem. Soc.* 133, 18042–18045 (2011).

3. Yella, A. *et al.* Porphyrin-Sensitized Solar Cells with Cobalt (II/III)-Based Redox Electrolyte Exceed 12 Percent Efficiency. *Science* 334, 629–634 (2011).
4. Wang, P. *et al.* Charge Separation and Efficient Light Energy Conversion in Sensitized Mesoscopic Solar Cells Based on Binary Ionic Liquids. *J. Am. Chem. Soc.* 127, 6850–6856 (2005).
5. Snaith, H. J. in *Dye-sensitized Solar Cells* (Kalyanasundaram, K.) 163–206 (EPFL Press, 2009).
6. Cappel, U. B., Daeneke, T. & Bach, U. Oxygen-Induced Doping of Spiro-MeOTAD in Solid-State Dye-Sensitized Solar Cells and Its Impact on Device Performance. *Nano. Lett.* 12, 4925–4931 (2012).
7. Schmidt-Mende, L. & Grätzel, M. TiO₂ pore-filling and its effect on the efficiency of solid-state dye-sensitized solar cells. *Thin Solid Films* 500, 296–301 (2006).
8. Ding, I.-K. *et al.* Pore-filling of spiro-OMeTAD in solid-state dye sensitized solar cells: quantification, mechanism, and consequences for device performance. *Adv. Funct. Mater.* 19, 2431–2436 (2009).
9. Melas-Kyriazi, J. *et al.* The Effect of Hole Transport Material Pore Filling on Photovoltaic Performance in Solid-State Dye-Sensitized Solar Cells. *Adv. Energy Mater.* 1, 407–414 (2011).
10. Tétreault, N. *et al.* High-efficiency solid-state dye-sensitized solar cells: fast charge extraction through self-assembled 3D fibrous network of crystalline TiO₂ nanowires. *ACS Nano* 4, 7644–7650 (2010).
11. Sommeling, P. M. *et al.* Influence of a TiCl₄ post-treatment on nanocrystalline TiO₂ films in dye-sensitized solar cells. *J. Phys. Chem. B* 110, 19191–19197 (2006).
12. O'Regan, B. C., Durrant, J. R., Sommeling, P. M. & Bakker, N. J. Influence of the TiCl₄ treatment on nanocrystalline TiO₂ films in dye-sensitized solar cells. 2. Charge density, band edge shifts, and quantification of recombination losses at short circuit. *J. Phys. Chem. C* 111, 14001–14010 (2007).
13. Kambe, S., Nakade, S., Wada, Y., Kitamura, T. & Yanagida, S. Effects of crystal structure, size, shape and surface structural differences on photo-induced electron transport in TiO₂ mesoporous electrodes. *J. Mater. Chem.* 12, 723–728 (2002).
14. Wang, P., Klein, C., Humphry-Baker, R., Zakeeruddin, S. M. & Grätzel, M. A High Molar Extinction Coefficient Sensitizer for Stable Dye-Sensitized Solar Cells. *J. Am. Chem. Soc.* 127, 808–809 (2005).

15. Van Stokkum, H. I. Global and target analysis of time-resolved spectra, Lectures notes : 'Troisième Cycle de la Physique en Suisse Romande'. 1–88 (2005).
16. Teuscher, J. Dynamics of electron transfer processes at the surface of dye-sensitized mesoporous semiconductor films - EPFL Thesis n°4731. 1–161 (2010).
17. Tachibana, Y. Charge Separation and Recombination in Dye Sensitized Semiconductor Solar Cells - Imperial College Thesis. 1–242 (1999).
18. Kallioinen, J., Benkő, G., Sundström, V., Korppi-Tommola, J. & Yartsev, A. P. Electron Transfer from the Singlet and Triplet Excited States of Ru(dcbpy)₂(NCS)₂ into Nanocrystalline TiO₂ Thin Films. *J. Phys. Chem. B* 106, 4396–4404 (2002).
19. Bach, U. *et al.* Charge separation in solid-state dye-sensitized heterojunction solar cells. *J. Am. Chem. Soc.* 121, 7445–7446 (1999).
20. Nazeeruddin, M. K. *et al.* Stepwise assembly of amphiphilic ruthenium sensitizers and their applications in dye-sensitized solar cell. *Coord. Chem. Rev.* 248, 1317–1328 (2004).
21. Kay, A., Humphry-Baker, R. & Grätzel, M. Artificial Photosynthesis. 2. Investigations on the Mechanism of Photosensitization of Nanocrystalline TiO₂ Solar Cells by Chlorophyll Derivatives. *J. Phys. Chem.* 98, 952–959 (1994).
22. Boschloo, G. & Fitzmaurice, D. Spectroelectrochemical Investigation of Surface States in Nanostructured TiO₂ Electrodes. *J. Phys. Chem. B* 103, 2228–2231 (1999).
23. Boschloo, G. & Fitzmaurice, D. Electron accumulation in nanostructured TiO₂ (anatase) electrodes. *J. Phys. Chem. B* 103, 7860–7868 (1999).
24. Cappel, U. B., Gibson, E., Hagfeldt, A. & Boschloo, G. Dye Regeneration by Spiro-MeOTAD in Solid State Dye-Sensitized Solar Cells Studied by Photoinduced Absorption Spectroscopy and Spectroelectrochemistry. *J. Phys. Chem. C* 113, 6275–6281 (2009).
25. Olson, C., Veldman, D., Bakker, K. & Lenzmann, F. Characterization of the pore filling of solid state dye sensitized solar cells with photoinduced absorption spectroscopy. *Int. J. Photoenergy* 2011, 1–11 (2011).
26. Moser, J.-E. *et al.* Comment on 'Measurement of Ultrafast Photoinduced Electron Transfer from Chemically Anchored Ru-Dye Molecules into Empty Electronic States in a Colloidal Anatase TiO₂ Film'. *J. Phys. Chem. B* 102, 3649–3650 (1998).
27. Ardo, S. & Meyer, G. J. Characterization of Photoinduced Self-Exchange Reactions at Molecule–Semiconductor Interfaces by Transient Polarization Spectroscopy:

Lateral Intermolecular Energy and Hole Transfer across Sensitized TiO₂ Thin Films. *J. Am. Chem. Soc.* 133, 15384–15396 (2011).

28. Tachibana, Y., Moser, J.-E., Grätzel, M., Klug, D. R. & Durrant, J. R. Subpicosecond interfacial charge separation in dye-sensitized nanocrystalline titanium dioxide films. *J. Phys. Chem.* 100, 20056–20062 (1996).

29. Kallioinen, J. *et al.* Photoinduced ultrafast dynamics of Ru(dcbpy)₂(NCS)₂-sensitized nanocrystalline TiO₂ films: The influence of sample preparation and experimental conditions. *J. Phys. Chem. B* 108, 6365–6373 (2004).

30. Wenger, B., Grätzel, M. & Moser, J.-E. Rationale for kinetic heterogeneity of ultrafast light-induced electron transfer from Ru(II) complex sensitizers to nanocrystalline TiO₂. *J. Am. Chem. Soc.* 127, 12150–12151 (2005).

31. Moser, J.-E. in *Dye-sensitized Solar Cells* (Kalyanasundaram, K.) 403–456 (EPFL Press, 2009).

32. Tiwana, P., Parkinson, P., Johnston, M. B., Snaith, H. J. & Herz, L. M. Ultrafast Terahertz Conductivity Dynamics in Mesoporous TiO₂: Influence of Dye Sensitization and Surface Treatment in Solid-State Dye-Sensitized Solar Cells. *J. Phys. Chem. C* 114, 1365–1371 (2010).

33. Bonhote, P. *et al.* Efficient lateral electron transport inside a monolayer of aromatic amines anchored on nanocrystalline metal oxide films. *J. Phys. Chem. B* 102, 1498–1507 (1998).

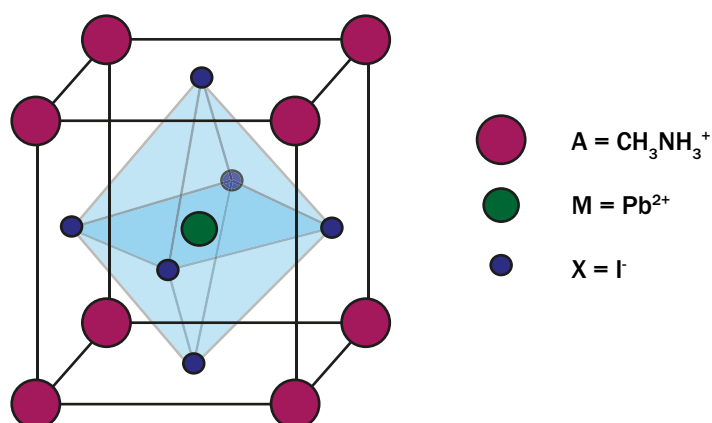
34. Snaith, H. J. *et al.* Charge collection and pore filling in solid-state dye-sensitized solar cells. *Nanotechnology* 19, 424003 (2008).

35. Laskova, B. *et al.* Voltage enhancement in dye-sensitized solar cell using (001)-oriented anatase TiO₂ nanosheets. *J. Solid State Electr.* 16, 2993–3001 (2012).

CHAPTER 5

Photophysical processes in $\text{CH}_3\text{NH}_3\text{PbI}_3$

This chapter will present the photophysics of a new and very promising light absorber, $\text{CH}_3\text{NH}_3\text{PbI}_3$. The main spectroscopic signatures of this material deposited on a mesoporous framework of Al_2O_3 , as obtained by transient absorption spectroscopy, will be introduced and analysed. The photophysical processes will be evidenced, enabling the study of interfacial processes with both a hole acceptor material and an electron acceptor material in Chapter 6.



5.1 Introduction

Recent advances in the solid-state dye-sensitized solar cell community have provided a major breakthrough for the development of cheap and upscalable hybrid solid-state solar cells. As described in Chapter 1, hybrid organic-inorganic all solid-state solar cells based on methylammonium lead halide perovskite absorbers have attracted attention because of their ease of fabrication and performances rivalling the best thin-film photovoltaic devices.¹⁻⁷ Among the various types of perovskite and morphologies reported to date, $\text{CH}_3\text{NH}_3\text{PbI}_3$ deposited on a mesoporous film of titanium dioxide through a sequential deposition method appears to yield the best certified conversion efficiency.⁸

Optical and electronic properties of the three-dimensional organic-inorganic systems have been studied thoroughly in the last decades.⁹⁻¹¹ Indeed, lead iodide based perovskites exhibit numerous properties that make them good candidates for being used as absorbers in solid-state sensitized solar cell, particularly because of their broadband absorption across the visible up to 800 nm, and their extinction coefficient one order of magnitude higher than the conventional N719 dye and Z907 dyes used in solid-state devices, rendering them particularly attractive for thinner cell architectures.^{12,13} An important spectral characteristic is the presence of an excitonic absorption peak at 750 nm for $\text{CH}_3\text{NH}_3\text{PbI}_3$, which translates in a sharp, gaussian-shaped versus wavelength photoluminescence with a maximum between 750 and 780 nm, depending on the impurities.^{1,14} Figure 5.1a shows the absorptance spectrum of a sample of $\text{CH}_3\text{NH}_3\text{PbI}_3 | \text{Al}_2\text{O}_3$ displaying the characteristic shoulder typical of exciton absorption. Excitation of $\text{CH}_3\text{NH}_3\text{PbI}_3$ might lead to exciton formation after carrier thermalisation. In this case, a Wannier-type exciton is formed, where the size of the exciton is larger than the respective unit cell and the binding energies reported are in the range of 30 to 50 meV.^{9-11,15,16} The photoluminescence occurring from exciton recombination, as observed by photoinduced absorption spectroscopy (PIA), is presented in Figure 5.1b.

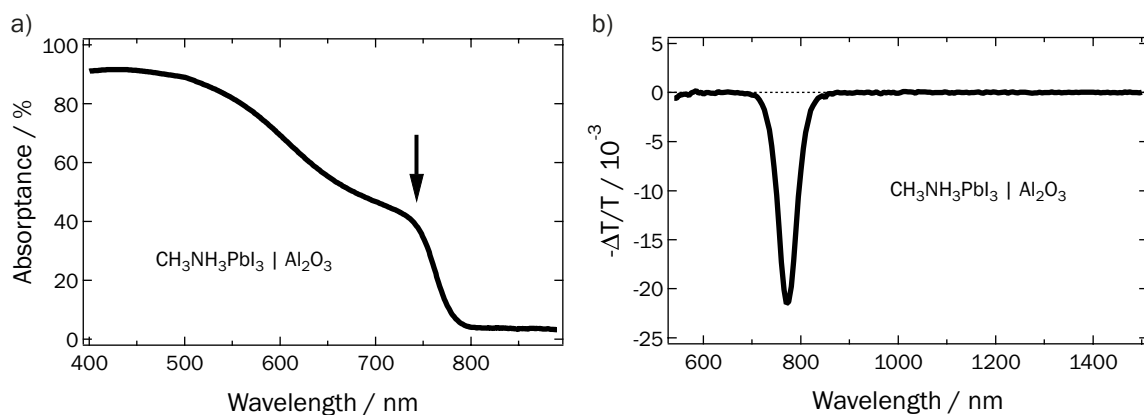


Figure 5.1 Optical characteristics of $\text{CH}_3\text{NH}_3\text{PbI}_3$

a) Absorbance spectrum of $\text{CH}_3\text{NH}_3\text{PbI}_3$ | Al_2O_3 deposited on a microscope glass slide. The arrow indicates the excitonic shoulder at 750 nm. b) Photoinduced absorption spectrum of a flat film of $\text{CH}_3\text{NH}_3\text{PbI}_3$ deposited on a 10-nm thin layer of Al_2O_3 on glass. The negative peak represents the photoluminescence of the material at 780 nm. The red-shift of the photoluminescence peak from the excitonic shoulder depends on the presence of impurities.

Throughout this thesis, comparison was made between samples containing the perovskite material deposited on Al_2O_3 and TiO_2 . Due to the mismatch of the energies of the conduction bands of $\text{CH}_3\text{NH}_3\text{PbI}_3$ (-3.93 eV vs. vacuum)⁵ and Al_2O_3 (-1 eV vs. vacuum),¹⁷ no electron transfer is expected between these two materials upon excitation of the light absorber. The only pathway for energy dissipation will then be radiative or non-radiative recombination within the perovskite material. The system on Al_2O_3 offers then the possibility to study the sole optical properties of the perovskite absorber while still depositing it on a mesoporous framework, rendering the comparison with the actual photovoltaic system based on mesoporous TiO_2 more relevant.

5.2 Methods

5.2.1 Samples preparation

Single-step deposition method

Hui-Seon Kim and Soo-Jin Moon (LPI, EPFL) prepared photoanodes for the transient absorption experiments in section 5.3.1 (excitation at 580 nm). A hydroiodic acid solution (30 ml, 0.227 mol, 57 wt.% in water, Aldrich) and methylamine (27.8 ml, 0.273 mol, 40% in methanol, TCI) were stirred in an ice bath. After stirring at 0°C for 2 h, the resulting solution was evaporated at 50°C for 1 h and produced $\text{CH}_3\text{NH}_3\text{I}$. The precipitate was

washed three times with diethyl ether, dried under vacuum, and used without further purification. To prepare $(\text{CH}_3\text{NH}_3)\text{PbI}_3$, $\text{CH}_3\text{NH}_3\text{I}$ (0.395 g) and PbI_2 (1.157 g, 99% Aldrich) were mixed in γ -butyrolactone (2 ml, 99% Aldrich) at 60°C , overnight with stirring. Homemade anatase Al_2O_3 nanoparticles were used.⁵ Thickness of the Al_2O_3 films was ca. 1 μm . The prepared films were coated with perovskite precursor solution, followed by heating at 100°C for 15 min. The composition of the hole transport material (HTM) solution was 0.170 M 2,2',7,7'-tetrakis-(N,N-di-p-methoxyphenylamine)-9,9'-spirobifluorene (*spiro*-MeOTAD, Merck KGaA), 0.064 M lithium bis(trifluoromethane sulfonyl)imide salt (LiTFSI, 99.95%, Aldrich) and 0.198 M 4-tert-butylpyridine (tBP, 96%, Aldrich) in the mixed solvent of chlorobenzene (99.8%, Aldrich) and acetonitrile (99.8%, Aldrich) (chlorobenzene : acetonitrile = 1:0.1 v/v). The perovskite | Al_2O_3 films were spin-coated with HTM solution at 4000 rpm.

Samples for transient absorption spectroscopy (TAS) measurements in section 5.3.1 (excitation at 510 nm) were prepared in a single-step deposition method analogous to the one employed above. Samples for photoinduced absorption spectroscopy (PIA, section 5.1) were prepared as flat films. 10-nm of Al_2O_3 was deposited on microscope glass slides by atomic layer deposition (ALD). The substrates were plasma-cleaned and then directly spin-coated with the perovskite solution prepared as described above.

Sequential deposition method

Samples for absorbance spectrum and TAS measurements in section 5.3.2 and 5.3.3 were deposited by sequential deposition method. A homemade alumina paste with 17 nm average nanoparticle diameter, was used diluted 1:3 in weight in EtOH, yielding films with 32 nm average pore size. 100 μl of the Al_2O_3 paste was spin-coated on 2×2 cm glass microscope slides (5000 rpm, 1000 rpm s^{-1} , 30 s). The films were then dried 15 min at 100°C and sintered for 30 min at 500°C . These conditions yielded an average thickness of 270 nm for the Al_2O_3 films, as measured by atomic force microscopy (Asylum Research, Cypher). PbI_2 (99%, Sigma-Aldrich) was dissolved in DMF at 70°C to yield a concentration of 1 M. 100 μl of the PbI_2 solution was spin-coated on the mesoporous substrates (6500 rpm, 5500 rpm s^{-1} , 30 s). The films were then dried for 15 min at 70°C . Methylammonium iodide was synthesized according to the procedure described above and a solution of 20 mg ml^{-1} of $\text{CH}_3\text{NH}_3\text{I}$ in isopropanol was prepared. PbI_2 substrates were immersed in this solution for 100 s, leading to a drastic color change of the film from

yellow to dark brown. The films were rinsed in isopropanol for 10 s. A solution of *spiro*-MeOTAD (Merck KGaA) was prepared by dissolving 90 mg in 1 ml chlorobenzene at 60°C. 8.75 μl of tBP (Sigma-Aldrich) was added to the latter chlorobenzene solution to yield a concentration of 0.06 M tBP. 17 mg of LiTFSI (Sigma-Aldrich) was dissolved in 100 μl of acetonitrile, and 18.75 μl of this solution was added to the same chlorobenzene solution to yield a concentration of 0.011 M LiTFSI. 80 μl of this solution was deposited onto the perovskite films and allowed to infiltrate for 10 s in order to maximize the penetration of the HTM prior to spin-coating (4000 rpm, 770 rpm s⁻¹, 30 s). All spin-coating operations were carried out in an argon glovebox. After preparation, samples were placed in vacuum for a few minutes and stored in argon until measurement, which were performed in a sealed cell under argon.

5.2.2 Femtosecond transient absorption

More details about the experimental setup can be found in Chapter 2. Transient absorption spectra were recorded using femtosecond pulsed laser pump-probe spectroscopy. The pump beam (510 or 580 nm) was generated with a two-stage non-collinear optical parametric amplifier (NOPA) from the 778 nm output of a Ti:Sa laser system with a regenerative amplifier providing 150 fs pulses at a repetition rate of 1 kHz. The pump beam was compressed with a pair of SF-10 prisms to sub-50 fs pulses. The probe consisted of a white light continuum (WLC) between 400 and 800 nm, generated by passing a portion of the 778 nm amplified Ti:Sa output through a 5 mm-thick sapphire plate (measurements in section 5.3.1). For measurements of section 5.3.2 and 5.3.3 the WLC scheme generation used a CaF₂ crystal as described in Chapter 2. The probe intensity was always less than the pump intensity and the spot size was much smaller. The probe pulses were time-delayed with respect to the pump pulses using a computerized translation stage. The probe beam was split before the sample into a signal beam (transmitted through the sample and crossed with the pump beam) and a reference beam. The signal and reference were detected with a pair of 163 mm spectrographs (Andor Technology, SR163) equipped with 512x58 pixels back-thinned cameras (Hamamatsu S07030-0906), assembled by Entwicklungsbüro Stresing, Berlin (measurements in section 5.3.1). For measurements of section 5.3.2 and 5.3.3, the signal and reference beams were detected with two spectrographs (Princeton instruments, SpectraPro 2150) equipped with the same cameras mentioned above, assembled by Entwicklungsbüro Stresing, Berlin. The

pump light was chopped at half the amplifier frequency, and the transmitted signal intensity was recorded shot by shot. It was corrected for intensity fluctuations using the reference beam. The transient spectra were averaged to the desired signal-to-noise ratio (typically 3000 acquisitions). The polarization of the probe pulses was at magic angle relative to that of the pump pulses. All spectra were corrected for the chirp of the white-light probe pulses.

5.3 Results

5.3.1 Overview of spectral signatures in $\text{CH}_3\text{NH}_3\text{PbI}_3$

Excitation at 580 nm, WLC probe

In this section, we provide a time-resolved spectroscopic characterization of $\text{CH}_3\text{NH}_3\text{PbI}_3$ | Al_2O_3 , in order to evidence the main spectral bands associated to the excitation of the perovskite. A brief comparison with a sample impregnated with the hole transport material *spiro*-MeOTAD will be made for the purpose of the discussion in section 5.4, but more details on the interfacial charge transfer processes will be provided in Chapter 6.

Figure 5.2a shows the transient absorption spectrum of a mesoscopic Al_2O_3 film where $\text{CH}_3\text{NH}_3\text{PbI}_3$ is deposited in a single-step deposition method. The perovskite films were measured in air, excited at $\lambda_{\text{exc}} = 580$ nm (fluence = $25 \mu\text{J}/\text{cm}^2$) and probed in the visible with a white-light continuum (440-740 nm). Due to the large absorption of probe light by the perovskites in the blue region (below 450 nm), it is difficult to obtain a clean transient spectrum, unless thin films are used.

A negative signal peaking at 480 nm is attributed to the bleaching of the perovskite ground state, while the positive absorption signal in the 630-700 nm region is ascribed to the perovskite excited state absorption. The negative peak starting after 700 nm on both samples could contain two contributions, from a stimulated emission and a ground state bleaching. From similarities with the results obtained by PIA (cf. section 5.1) and steady-state emission,⁵ as well as because of the relative intensity of this peak, it is likely that the stimulated emission is playing a major role in this region, especially because the probe light

generated with a 775 nm source can still have some residues of fundamental that could help stimulating the transition. Other groups observed similar spectral bands for the perovskite material using femtosecond transient absorption spectroscopy,¹⁸ and some similarities were also remarked in nanosecond transient absorption spectra;¹⁹ both studies attribute the band in the red region to a photobleaching rather than a stimulated emission contribution. This discrepancy will be addressed below in this chapter; here we infer that the major part of this signal is due to stimulated emission, and in the discussion for the model of the perovskite we will further prove by the analysis of various hypothetical cases that stimulated emission represents indeed the major part of the negative band in the 700-nm region. The early stimulated emission (before 1 ps) appears to be red-shifting and this effect will be extensively discussed in section 5.3.3.

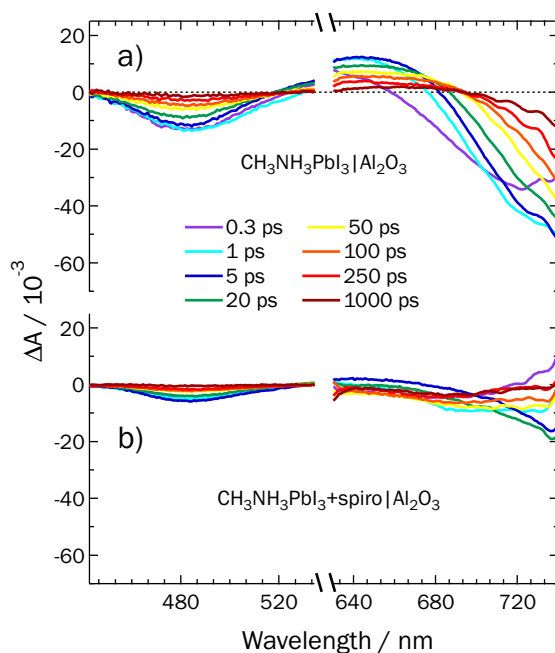


Figure 5.2 Transient absorption spectrum of $\text{CH}_3\text{NH}_3\text{PbI}_3$ | Al_2O_3 , excitation = 580 nm

a) $\text{CH}_3\text{NH}_3\text{PbI}_3$ | Al_2O_3 transient absorbance recorded at various time delays after excitation (color lines). The perovskite films were measured in air, excited at $\lambda_{\text{exc}} = 580$ nm (fluence = $25 \mu\text{J} / \text{cm}^2$) and probed with white-light continuum in the visible (440 – 740 nm). a) $\text{CH}_3\text{NH}_3\text{PbI}_3 + \text{spiro-MeOTAD}$ | Al_2O_3 transient absorbance recorded at various time delays after excitation (color lines). The perovskite films were measured in air, excited at $\lambda_{\text{exc}} = 580$ nm (fluence = $25 \mu\text{J} / \text{cm}^2$) and probed with white-light continuum in the visible (440 – 740 nm).

Figure 5.2b supports the assignment of the three spectral bands by comparison with a sample impregnated with *spiro*-MeOTAD, where it is expected to observe the hole extraction, and thus quenching of the excited state. All spectral bands are decreased within

the first picosecond after excitation, indicating regeneration of an initial ground state and quenching of an excited state, as well as reflecting the quenching of the stimulated emission.

Figure 5.3 shows the dynamics for positive signal and the ground state bleaching (640 and 480 nm) as fitted by the analytical convolution function of one Gaussian instrument response and three exponentials, a rising one and two decaying ones. The rising exponential, with a time constant of 0.35 ps will be described later in detail in section 5.3.3. Time constants for the first decaying exponential are comparable for 640 and 480 nm, and are respectively $\tau(480) = 25$ ps and $\tau(640) = 30$ ps. This is a further confirmation that the species associated with the positive band and the negative band must be related. The third exponential is associated with the decay to zero within the first nanosecond after excitation (the actual dynamics of the decay is influenced by the fluence as it will be shown in section 5.3.2).

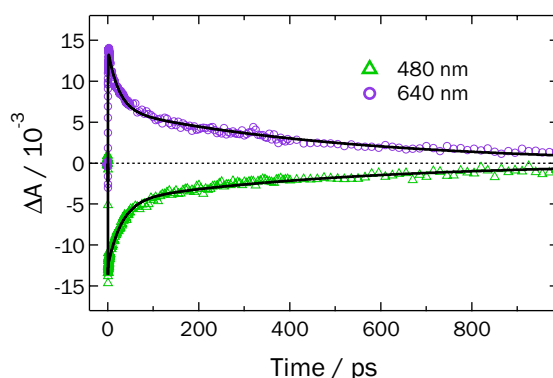
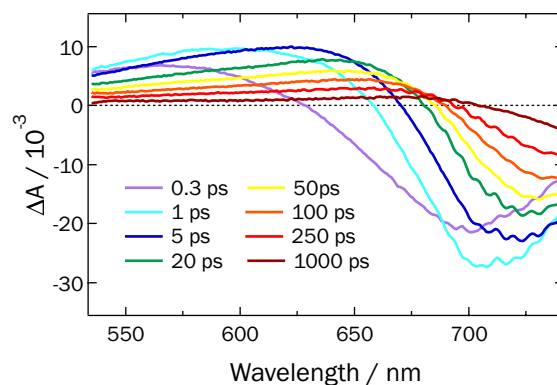


Figure 5.3 Dynamics of $\text{CH}_3\text{NH}_3\text{PbI}_3$ | Al_2O_3 , excitation = 580 nm

Dynamics extracted at 480 nm (green triangles) and 640 nm (purple circles) for the same sample as presented in Figure 5.2a. The solid lines represent fit of the data with an analytical convolution function of one Gaussian and three exponentials.

Excitation at 510 nm, WLC probe**Figure 5.4 Transient absorption spectrum of $\text{CH}_3\text{NH}_3\text{PbI}_3$ | Al_2O_3 , excitation = 510 nm**

$\text{CH}_3\text{NH}_3\text{PbI}_3$ | Al_2O_3 transient absorbance recorded at various time delays after excitation (color lines). The perovskite films were measured in air, excited at $\lambda_{\text{exc}} = 510$ nm (fluence = $50 \mu\text{J}/\text{cm}^2$) and probed with white-light continuum from 530-750 nm.

A different excitation wavelength ($\lambda_{\text{exc}} = 510$ nm) was used in order to examine whether the spectral bands reported for excitation at 580 nm were still observable. The transient absorbance spectrum (Figure 5.4) shows identical spectral features as in the case of the longer excitation wavelength. A positive absorption band is present from 540 nm to close to 700 nm, which was previously ascribed to the perovskite excited state absorption. The negative band in the red-region, attributed to stimulated emission, is again red-shifting in the initial phase, similarly to the data reported above. A difference can be noticed regarding the early stimulated emission (before 1 ps), which is blue shifted with respect to the data reported in Figure 5.2a.

This dependence on the excitation wavelength tends to be indicative of a process involving hot states, which are populated differently according to the pump wavelength used. The origin of this effect will be made clear in section 5.3.3.

5.3.2 Fluence effects

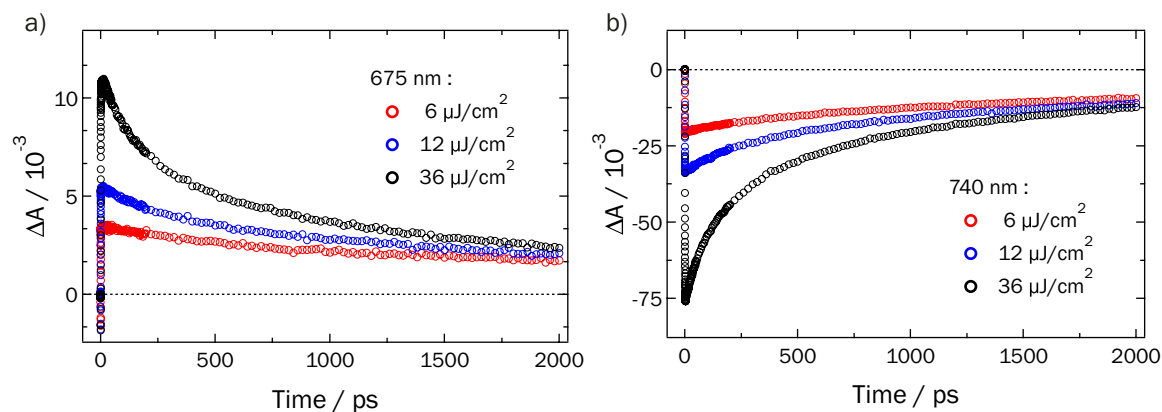


Figure 5.5 Transient dynamics in $\text{CH}_3\text{NH}_3\text{PbI}_3$ | Al_2O_3 as a function of the fluence

a) Dynamics extracted at 675 nm and b) Dynamics extracted at 740 nm for $\text{CH}_3\text{NH}_3\text{PbI}_3$ | Al_2O_3 at three different fluences (red: $6 \mu\text{J}/\text{cm}^2$, blue: $12 \mu\text{J}/\text{cm}^2$ and black: $36 \mu\text{J}/\text{cm}^2$).

In this section, results are obtained with a two-step sequential deposition method, as converted from an initial 1 M PbI_2 solution. This method is believed to yield more conformal films.¹ The effect of the fluence on the dynamics of the decays of the excited state signal has been examined. On an alumina framework, where we only expect recombination within the perovskite absorber, a higher fluence should lead to an increased non-geminate recombination.

Figure 5.5 shows the dynamics extracted from the transient absorption spectrum obtained on a sample of $\text{CH}_3\text{NH}_3\text{PbI}_3$ deposited on mesoporous Al_2O_3 and measured under inert conditions (in a sealed cell under argon). Figure 5.5a displays the dynamics in the positive absorption band (675 nm), while Figure 5.5b shows the stimulated emission dynamics at 740 nm. Three different fluences were used (6 , 12 and $36 \mu\text{J}/\text{cm}^2$). As expected, recombination kinetics increases with increasing fluence, showing that the recombination is affected by non-geminate recombination. However, only the initial dynamics is direct recombination of carriers, while in the long timescale (> 1.5 ns), the amount of remaining signal is equal for all the fluences, showing that charges can be rapidly delocalised, and thus recombine on much longer timescales.

5.3.3 Global analysis

In this section, results are obtained with a two-step sequential deposition method, similarly to samples in section 5.3.2. The photophysical processes in the perovskite absorber were further elucidated by global analysis of the transient absorption spectrum. Global analysis

is a powerful tool in order to determine which photoinduced processes correspond to related species (i.e. processes with an identical time constant), by giving the spectral amplitude associated to a given time constant.

Figure 5.6a shows the transient absorption spectrum of a $\text{CH}_3\text{NH}_3\text{PbI}_3$ sample deposited on mesoporous Al_2O_3 (Figure 5.6a) excited at $\lambda_{\text{exc}} = 580$ nm (fluence = $6 \mu\text{J}/\text{cm}^2$) and probed with white-light continuum between 450 to 750 nm. The dynamics in the first ps shows again a negative band from 600 to 700 nm which red-shifts with time. It is worth to mention that this band has been observed on *all* $\text{CH}_3\text{NH}_3\text{PbI}_3$ samples (cf. previous sections). A clearer picture of this process can be seen in Figure 5.6c, in which a view of the dynamics as a function of the wavelength can be seen. Figure 5.6c visibly illustrates the red-shifting effect occurring on the first ps after photoexcitation.

The corresponding associated spectrum is obtained by fitting the dynamics with the analytical convolution function of a Gaussian instrument response and three exponentials. Successive iterations of the global analysis fit give $\tau_1 = 0.35$ ps, $\tau_2 = 350$ ps and $\tau_3 = 3.6$ ns. The amplitudes associated to these three time constants are displayed in Figure 5.6b. The first, rapid component (0.35 ps) is negative in the blue region (450-550), as well as from 600 to 740 nm. A third, positive part after 740 nm is also noticeable. The first negative part is associated to the bleaching, since the following longer components remain negative. The negative part between 600 and 740 nm is responsible for the red-shift of the photoluminescence at longer timescales and could be related to hot states whose depopulation is stimulated by the probe. The hypothesis of hot states matches well with the observation of a positive region after 740 nm, corresponding in the dynamics to a build-up of the stimulated emission peak on the first picosecond.

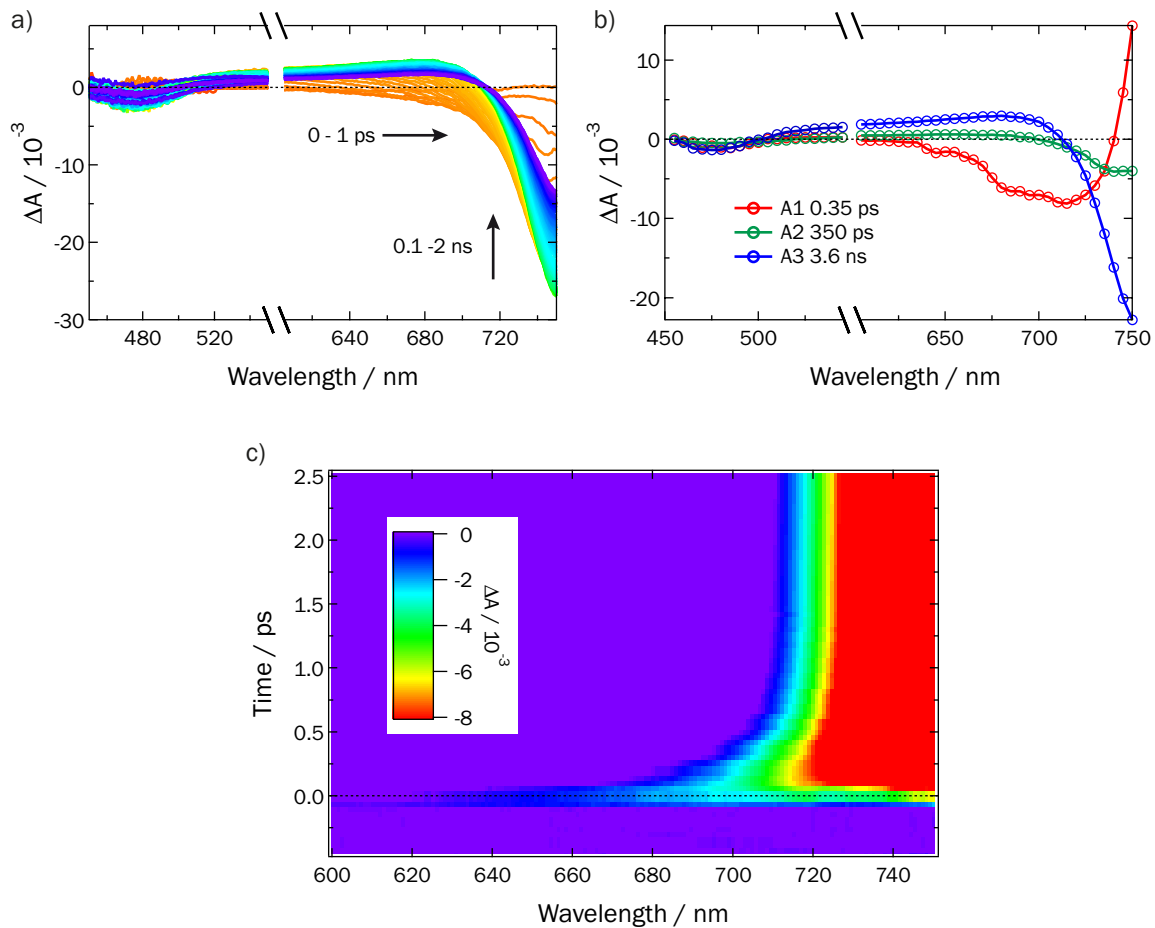


Figure 5.6 Transient absorption spectrum of $\text{CH}_3\text{NH}_3\text{PbI}_3 \mid \text{Al}_2\text{O}_3$ and associated spectra

a) $\text{CH}_3\text{NH}_3\text{PbI}_3 \mid \text{Al}_2\text{O}_3$ recorded at various time delays after excitation (color lines). The perovskite films were measured under argon, excited at $\lambda_{\text{exc}} = 580 \text{ nm}$ (fluence = $6 \mu\text{J} / \text{cm}^2$) and probed with white-light continuum from 450 – 750 nm. b) Associated spectra resulting from global fit analysis of the data in a). Three components can be extracted using the convolution of one Gaussian and three exponentials. Red: amplitude spectrum associated to the fastest component (0.35 ps). Green: amplitude spectrum associated to the 350 ps component. Blue: amplitude spectrum associated to the 3.6 ns component. c) Dynamics from -0.5 to 2.5 ps, in the 600-750 nm region. The red-shift from 640 to 710 nm is very clear and is completed within the first picosecond after excitation.

The second and third components (respectively 350 ps and 3.6 ns) are related to the deactivation processes in the perovskite. Both still have the signature of the ground state bleaching that is recovering (450-500 nm region), while the peak of the stimulated emission is clearly visible and shifted to longer wavelengths with respect to the 0.35 ps component, thus matching the steady-state photoluminescence. This is indicative of a relaxed emission, which occurs from the bottom of the conduction band, from cooled electrons, or alternatively from the top of the valence band, from cooled holes. The distinction between the two is not straightforward at this point. The processes occurring during the first 2.5 picoseconds, shown in the spectral domain in Figure 5.6c, are evidenced in the time domain in Figure 5.7.

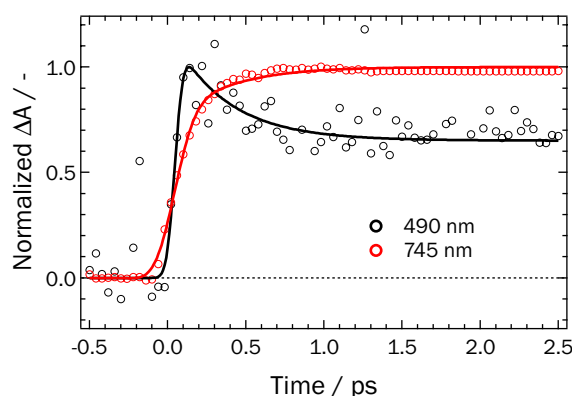


Figure 5.7 Comparison of initial dynamics

Dynamics extracted at 490 nm (black) and 745 nm (red) for $\text{CH}_3\text{NH}_3\text{PbI}_3 | \text{Al}_2\text{O}_3$ from sample shown in Figure 5.6. The solid lines represent convolution of one Gaussian and three exponentials (only the first, fastest exponential is visible here, corresponding to $\tau_1 = 0.35$ ps).

Figure 5.7 shows the normalized dynamics extracted at 490 nm (ground state bleaching) and 745 nm (stimulated emission) respectively, with the corresponding fits obtained through the global analysis. The dynamics are displayed until 2.5 ps in order to consider only the initial processes after photoexcitation. It is very clear that the initial bleaching is decaying while the stimulated emission is increasing, with a common lifetime of 0.35 ps. This confirms the hypothesis that part of the ground state is quickly recovered (by the stimulated emission induced by the probe). In the meantime, relaxed states from where the luminescence can occur are created, with the same time constant.

In fact, these three phenomena give the lifetime for the relaxation of the hot states: indeed, part of the bleaching is recovered in 0.35 ps. The early stimulated emission in the 600-740 nm spectral range is a way to *probe* the population of excited states present after photoexcitation. In the same temporal range, the stimulated emission in the red (from 740 nm) is increasing and reaches a plateau, indicating that the bottom of the conduction band/top of the valence band is reached. The relaxation from hot states is further confirmed by the data reported on Figure 5.4, where excitation is carried out at 510 nm. In this case, the early stimulated emission is blue shifted with respect to the data reported for the perovskite excited at 580 nm (Figure 5.1 and Figure 5.6a).

An identical figure has been reported in a recent publication.¹⁸ However, the situation of an initial decrease of the blue component while the red component still increases is only observed in the case of high-energy pump excitation (400 nm), and not observed for lower pump energies (600 nm). This might be an indication sample preparation has an influence on the reported photo-dynamics.

5.4 Band model for $\text{CH}_3\text{NH}_3\text{PbI}_3$

In this section, we will attempt to establish a general model for the photophysics of the perovskite. We will start by defining a simple band model to account for all transitions observed in the visible femtosecond transient absorption spectrum of the material. We will comment this band diagram based on our experimental results and the ones published in a recent paper by Xing et al.¹⁸ The authors measure the femtosecond transient absorption spectrum of 65 nm-flat films of $\text{CH}_3\text{NH}_3\text{PbI}_3$, and propose a band model with approximate energies to match their spectroscopic findings, that corresponds to the left part of Figure 5.8.

Figure 5.8 shows the situation for a hypothetical system with two valence bands VB1, VB2 and one conduction band CB1 (Figure 5.8, left), and compare it to the reverse hypothetical situation with two conduction bands CB1, CB2 and one valence band VB1 (Figure 5.8, right). This kind of 3-band models should be able to explain all spectral transitions observed experimentally. We will take the case of pump excitation at 600 nm, which is less than the energy gap of the negative “blue” band observed in the 450-500 nm region, for all samples probed with WLC.

In Figure 5.8a can be found the situation without any electron or hole extracting layer (pure $\text{CH}_3\text{NH}_3\text{PbI}_3$). On the left, upon pump excitation at 600 nm, which is less than the energy gap of the 450-500 nm band, one hole will be found in VB1 and one electron in CB1. Since the population in VB1 is depleted, a persistent bleaching will be observed upon the probe-induced transition from VB1 to CB1 (that will be referred to as **PB2**). Additionally, since CB1 is populated, the transition from VB2 to CB1 will be hindered as well, thus resulting in a persistent bleaching (that will be referred to as **PB1**). As mentioned above, this model with two valence bands and one conduction band is the one Xing et al. use to explain their results. PB1 thus corresponds experimentally to the ground state bleaching observed in the blue region (450-500 nm). PB2 corresponds to a ground state bleaching in the red-region (after 700 nm). However, we mentioned before that this negative “red” band could contain both stimulated emission and ground state bleaching. We will show through the analysis of various hypothetical cases that it is not possible to have solely a photobleaching in this region and that stimulated emission must be considered too. Xing et al. mention the presence of stimulated emission, but they further never take it into account in their discussion, thus just speaking about the photobleaching PB2.

Reversed scheme can be found on the right side of Figure 5.8a. Upon pump excitation at 600 nm, one hole will be in VB1 and one electron in CB1. The transition from VB1 to CB1 is therefore less probable: again, since the population in VB1 is depleted, a persistent bleaching will be observed upon the probe-induced transition from VB1 to CB1 (i.e. PB2). In this case CB2, which is not populated by the low energy pump would be available for a transition, but since VB1 has been depleted, the probability for transition from VB1 to CB2 will be decreased. This situation results again in a persistent bleaching PB1. We make the hypothesis that both the depletion of VB1 and the filling of CB1 can be responsible for a bleaching (the probe-beam induced transitions will involve electronic states with changed population, which could be either electrons or holes).

These two situations (Figure 5.8a, left and right) are both well suited to describe our results, presented earlier in this chapter for $\text{CH}_3\text{NH}_3\text{PbI}_3 \mid \text{Al}_2\text{O}_3$ (i.e. two bleachings that recover slowly, on ns timescale) as well as what is observed experimentally by Xing et al. Indeed, using a photoexcitation with lower energy than the transition associated to PB1 (600 nm excitation), they suggest that the transition at 480 nm (in the blue region) could only correspond to a situation where only one of the two energy states involving this transition is populated, that could be the higher energy valence band (VB1) or the lowest energy conduction band (CB1).

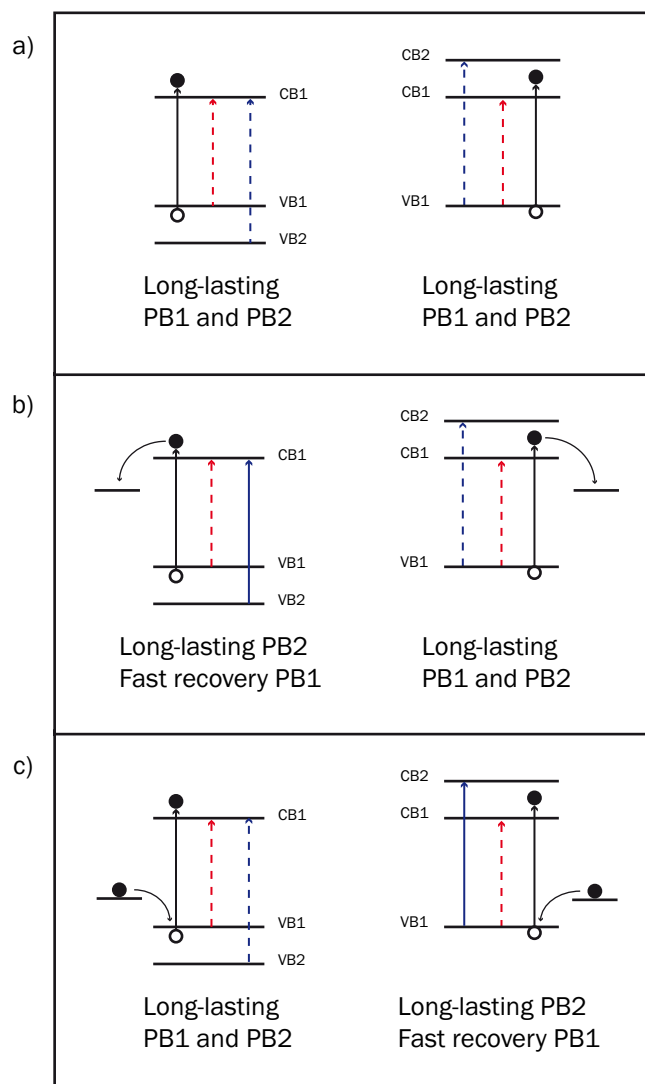


Figure 5.8 Schematic band diagram of the perovskite system in two hypothetical cases

a) Pure perovskite b) Perovskite with an electron acceptor c) Perovskite with a hole acceptor. Left case is a hypothetical situation with two conduction bands and one valence band as proposed by Xing et al. in ref.18, while right case shows two conduction bands and one valence band. Pump excitation, in black, is taken lower than the energy of PB1 (i.e. 600 nm). Red arrows correspond to low-energy probe transitions, while blue arrows correspond to higher energy probe transitions. Transitions that are less probable because of state filling/depletion are indicated as dashed arrows.

In order to understand the photophysics of the perovskite, we need to introduce here two interfaces that allow charge extraction, i.e. an electron extracting material (Figure 5.8b) and a hole extracting material (Figure 5.8c). The experimental evidences of these processes will be further shown in detail in Chapter 6.

In this frame, Xing et al. observe that upon presence of an electron quencher (PCBM), both bleachings PB1 and PB2 are recovered faster, while upon presence of a hole quencher (*spiro*-MeOTAD), only PB2 is recovered. A faster recovery of the bleaching can then be understood as a *quenching* of the excited state by charge transfer and the terms will

be used interchangeably in the discussion. They thus conclude that because PB1 and PB2 dynamics are both affected by the presence of an electron extraction layer, the probe must monitor the electron population in CB1. Additionally, since the hole extracting layer affects only the PB2 dynamics, it must be related with the hole population in VB1, and PB1, which corresponds to the transition between a lower energy valence band VB2 and CB1, must be only related to the electron population in CB1.

Figure 5.8b shows the situation where the electron-extracting layer is added to the perovskite system. On the left side, CB1 is depleted because of extraction of electrons, and holes remain in VB1. This implies that transition from VB1 to CB1 is hindered (depletion of states), while transition from VB2 to CB1 is recovered because additional states are available after electron extraction. This translates in a persistent PB2 bleaching, while a faster recovery of PB1 is possible. This is the model proposed by Xing et al. to explain their results, but does not match the observation they made of a fast recovery of both PB1 and PB2. On the right side of Figure 5.8b, CB1 is depleted because of extraction of electrons, and holes remain in VB1. As in the case above, the transition VB1 – CB1 is hindered because of depletion of states in VB1. However, the transition VB1 – CB2 is hindered too for the same reason. Thus, two persistent PB1 and PB2 bleachings must be observed, and this model is not suited to explain their experimental results observing fast recovery of both PB1 and PB2.

Last case shown in Figure 5.8c illustrates the presence of a hole extracting material such as *spiro*-MeOTAD. On the left, the recovery of states in VB1 is possible in presence of *spiro*-MeOTAD. However, since CB1 is now populated, the transitions either from VB1 to CB1 or from VB2 to CB1 are less susceptible to occur. This results in two persistent PB1 and PB2 bleachings. This band model would not explain the quenching of both bleachings PB1 and PB2 as it is visible in Figure 5.2b, furthermore this same model proposed by Xing et al. would also not explain their observations about the recover of PB2. On the right side, quenching of VB1 by the HTM allows recovering the possibility for the transition VB1 – CB2, thus effectively recovering the PB1 bleaching, while PB2 remains hindered. This condition would explain the quenching of PB1 we observe in Figure 5.2b, but would not explain the quenching of PB2. In the case of Xing et al., they do not observe the recovery of the PB1 bleaching, but the model is also unable to account for the fastest recovery of PB2 they observed, and which is similar to our case.

Interestingly, it seems that we need crossed models, more clearly two conduction bands and two valence bands to fully explain the results observed. Indeed, in our case, evidences of quenching for both blue and red bands for a sample of perovskite deposited on alumina and impregnated with *spiro*-MeOTAD (where the hole can be extracted but not the electron) are shown in Figure 5.2b, and will be discussed thoroughly in Chapter 6. Xing et al. observe the quenching of the two bleachings PB1 and PB2 by PCBM, while they observe only the quenching of PB2 by *spiro*-MeOTAD. Fast recovery of the two blue and red bands while in contact with either with PCBM or with *spiro*-MeOTAD can be explained by a situation where:

- 1) The band in the red-region contains a part of stimulated emission (SE): by quenching with either hole or electron acceptor material this peak will at least partially disappear. If this is not true, it would not be possible to explain the quenching of PB1 and PB2 by PCBM observed experimentally by Xing et al. and attributed to case b) left (it is worth noting that case b) right cannot account for the experimental results). Similarly, in the case of HTM, case c) left can account for experimental results of Xing et al. only if we take into account SE to explain the decrease of the red band. Case c) right, also considering SE, would account for the results presented in Figure 5.2b and in Chapter 6, where the blue and red bands are both quenched upon the addition of HTM. As additional evidence, if we had a significant contribution of photobleaching in this region, we would not observe the slow increase in the red region as illustrated by the dynamics presented in Figure 5.7. The bleaching at 480 nm presented in Figure 5.7 is clearly rapidly regenerated, while the 740 nm is still increasing. However, one must say that the bleaching contribution is likely to be negligible in amplitude compared to the stimulated emission, which would effectively mask it.
- 2) We take into account crossed-models. The fast recovery of PB1, observed by Xing et al. upon addition of PCBM is explained by case b) left. However, we observe it in Figure 5.2b upon addition of *spiro*-MeOTAD, situation which is explained by case c) right. Furthermore, case c) left will not explain the results observed in presence of an HTM, but can explain the results in presence of an electron acceptor (case b) left). Similarly, case b) right cannot explain the results in presence of an electron acceptor, but can explain the features observed in presence of a hole

acceptor (case c) right). Each situation (electron acceptor or hole acceptor) can thus be explained by one of the model proposed (left or right) in a crossed fashion.

Figure 5.9 summarizes the conclusions to draw from all these hypothetical cases: only a combination of the two models, together with the consideration of the presence of stimulated emission, would account for all experimental results. Figure 5.9a explains the long lasting blue and red bands always observed when no charge extracting material is present. Figure 5.9b explains the faster recovery of blue and red bands observed by Xing et al., and finally Figure 5.9c explains the results observed in Figure 5.2b, where both blue and red bands are decreased upon addition of HTM.

It appears difficult to explain why the decrease of PB1 in presence of *spiro*-MeOTAD is not observed in certain cases, as in the paper by Xing et al. A plausible explanation would be that the preparation conditions lead to a situation closer to Figure 5.8c left, with long-lasting blue and red bands. If then we take into account the stimulated emission, the red band only will decrease because of extraction of the carriers. The preparation conditions could also explain why in ref.18, the authors observe a rapid cooling at 480 nm for 400 nm excitation and not for 600 nm excitation, while in our case the cooling is observed for 580 nm excitation.

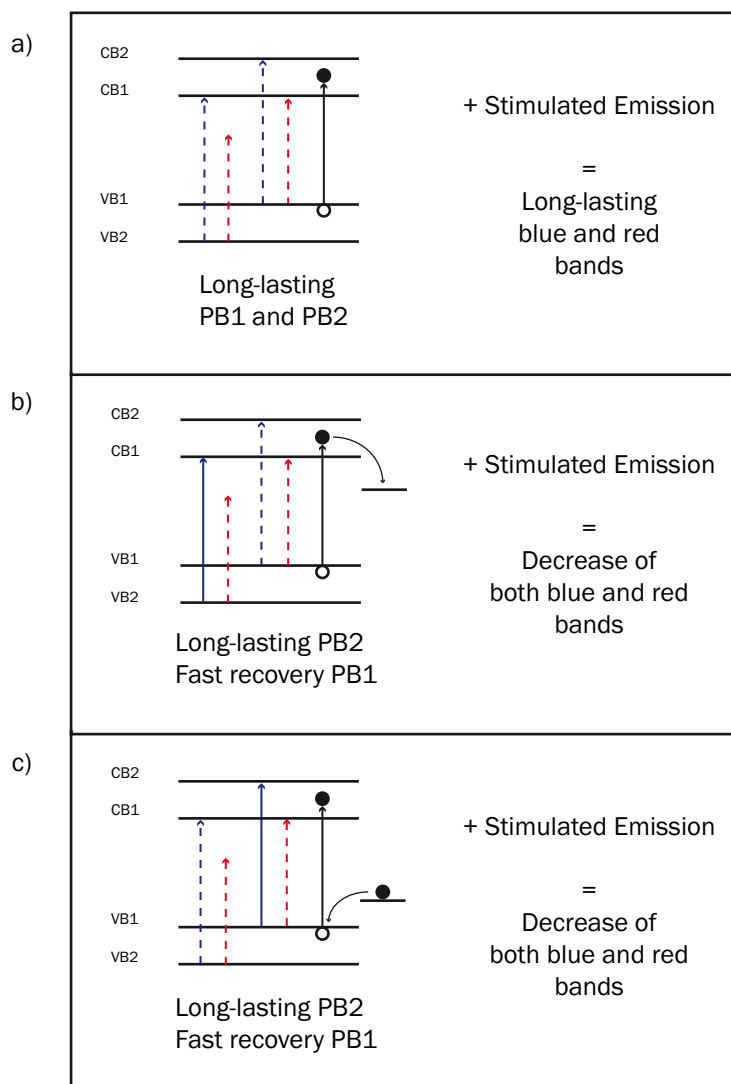


Figure 5.9 Schematic band diagram of the perovskite system with two conduction bands and two valence bands

a) Pure perovskite b) Perovskite with an electron acceptor c) Perovskite with a hole acceptor. Pump excitation, in black, is taken lower than the energy bandgap of PB1 (i.e. 600 nm vs. 480 nm). Red arrows correspond to low-energy transitions, while blue arrows correspond to higher energy transitions. Transitions that are less probable because of state filling/depletion are represented with dashed arrows.

Our band model, with two valence bands and two conduction bands, could also explain some of the conflicting results presented in the literature. In this past year, many reports have been published concerning the theoretical calculation of the band structure of perovskite and up to now, no clear unified model emerges from these studies. The main difficulty concerning the theoretical calculations concerns the inclusion of the spin-orbit coupling, which plays a major role because of the presence of lead. Mosconi et al. have reported the total density of states for $\text{CH}_3\text{NH}_3\text{PbI}_3$.²⁰ The calculations show two clear conduction bands and one valence band. The difference between the two conduction bands is interestingly of 1 eV, which corresponds exactly to the difference in energy

between the two negative bands observed by femtosecond transient absorption. A similar band structure is reported in a paper by Giorgi et al., where we can observe a calculated band structure with two distinct conduction bands and several close valence bands.²¹ Even et al. instead favour a model with two distinct valence bands and several close conduction bands, together with Yin et al. who report close conduction bands and at least two distinct valence bands.^{22,23}

Experimentally, electronic structure of perovskite studied by hard X-ray photoelectron spectroscopy rather indicates the presence of a single, broad valence band.²⁴ An earlier report by Umebayashi et al. favoured the presence of two valence bands distanced by 1 eV as studied by ultraviolet photoelectron spectroscopy.²⁵ Both theoretically and experimentally, it is not trivial to converge on a similar picture of the system, thus evidencing the need for further investigations.

Here, a speculative hypothesis on the nature of the excited-state absorption observed between 600 and 700 nm can also be made in the frame of the two-band models. Knowing that we observe absorption from photoinduced charges in the perovskite at 1400 nm (cf. Chapter 6), it is not unlikely that a double inter-band absorption of an IR photon of both electron and hole would give a transient absorption situated in the 600-700 nm region. Another speculation could concern the presence of down-conversion effects where the incoming photon from the probe beam (600-700 nm) is split into two IR photons exciting inter-band transitions.

5.5 Conclusion

In this chapter we describe the main spectral signatures obtained by femtosecond transient absorption spectroscopy of $\text{CH}_3\text{NH}_3\text{PbI}_3$ deposited on a mesoporous framework of Al_2O_3 . In this way, the only deactivation pathway possible is charge recombination within the perovskite itself, and thus the photophysical processes in the material can be evidenced. The visible transient absorption spectrum of $\text{CH}_3\text{NH}_3\text{PbI}_3$ for two different wavelengths of excitation (510 and 580 nm) shows three main spectral components: a first negative signal peaking at 480 nm (blue band), which is attributed to the bleaching of the ground state species of the perovskite. A positive absorption signal between 630 and 700 nm is ascribed to the excited state absorption. Then, a negative peak starting after 700 nm (red band) on both samples is attributed to stimulated emission.

The effect of the fluence on the dynamics is presented and shows increasing recombination with increasing fluence in the first nanosecond. The recombination at longer timescales (> 1.5 ns) is then similar for all samples, showing fast delocalisation of the carriers. Global analysis performed on a $\text{CH}_3\text{NH}_3\text{PbI}_3$ sample provides additional insight in the origin of the spectral features observed. It is inferred that the stimulated emission in the 700 nm-region is a way to probe the thermalisation of hot states to the bottom of the conduction band, or the top of the valence band. This thermalisation process occurs with a time constant of 0.35 ps, as shown by the partial recovery of the bleaching in the 480 nm-region and the increase of the stimulated emission on the same timescale.

An alternative proposition to the model presented by Xing et al. is given, with emphasis on the photophysical processes observed in three different cases: pure perovskite, with an electron acceptor and with a hole acceptor. By analysis of two hypothetical situations, with in a first case two valence bands and one conduction band, and a second case with two conduction bands and one valence band, it is inferred that these separate situations are not sufficient to fully explain all the photophysical processes observed. We propose a model with two conduction bands and two valence bands as an alternative proposition to the model presented by Xing et al., which allows to explain all observed spectral features and brings the confirmation that the negative spectral band in the 700-nm region must indeed contain a significant contribution from stimulated emission. Unravelling the photophysical processes of the perovskite light absorber $\text{CH}_3\text{NH}_3\text{PbI}_3$ enables us to study charge transfers at the interface with both a hole acceptor material and an electron acceptor material in Chapter 6.

5.6 References

1. Burschka, J. *et al.* Sequential deposition as a route to high-performance perovskite-sensitized solar cells. *Nature* 499, 316–319 (2013).
2. Heo, J. H. *et al.* Efficient inorganic-organic hybrid heterojunction solar cells containing perovskite compound and polymeric hole conductors. *Nature Photon.* 7, 486–491 (2013).
3. Noh, J. H., Im, S. H., Heo, J. H., Mandal, T. N. & Seok, S. I. Chemical management for colorful, efficient, and stable inorganic-organic hybrid nanostructured solar cells. *Nano. Lett.* 13, 1764–1769 (2013).

4. Qiu, J. *et al.* All-solid-state hybrid solar cells based on a new organometal halide perovskite sensitizer and one-dimensional TiO₂ nanowire arrays. *Nanoscale* 5, 3245–3248 (2013).
5. Kim, H.-S. *et al.* Lead iodide perovskite sensitized all-solid-state submicron thin film mesoscopic solar cell with efficiency exceeding 9%. *Sci Rep* 2, 591 (2012).
6. Lee, M. M., Teuscher, J., Miyasaka, T., Murakami, T. N. & Snaith, H. J. Efficient hybrid solar cells based on meso-superstructured organometal halide perovskites. *Science* 338, 643–647 (2012).
7. Im, J.-H. H., Lee, C.-R., Lee, J.-W., Park, S.-W. & Park, N.-G. 6.5% efficient perovskite quantum-dot-sensitized solar cell. *Nanoscale* 3, 4088–4093 (2011).
8. NREL Chart. *www.nrel.gov* (2014). at <<http://www.nrel.gov/ncpv/>>
9. Papavassiliou, G. C. Three- and low-dimensional inorganic semiconductors. *Prog. Solid State Ch.* 25, 125–270 (1997).
10. Ishihara, T. Optical properties of PbI₂-based perovskite structures. *J. Lumin.* 60, 269–274 (1994).
11. Mitzi, D. B. Templating and structural engineering in organic–inorganic perovskites. *J. Chem. Soc., Dalton Trans.* 1–12 (2000).
12. Kojima, A., Teshima, K., Shirai, Y. & Miyasaka, T. Organometal halide perovskites as visible-light sensitizers for photovoltaic cells. *J. Am. Chem. Soc.* 131, 6050–6051 (2009).
13. Kazim, S., Nazeeruddin, M. K., Grätzel, M. & Ahmad, S. Perovskite as Light Harvester: A Game Changer in Photovoltaics. *Angew. Chem. Int. Ed. (English)* n/a–n/a (2014). doi:10.1002/anie.201308719
14. Papavassiliou, G. C., Mousdis, G. A., Koutselas, I. B. & Papaioannou, G. J. Excitonic bands in the photoconductivity spectra of some organic-inorganic hybrid compounds based on metal halide units. *Int. J. Mod. Phys. B* 15, 3727–3731 (2001).
15. Tanaka, K. *et al.* Comparative study on the excitons in lead-halide-based perovskite-type crystals CH₃NH₃PbBr₃ CH₃NH₃PbI₃. *Solid State Commun.* 127, 619–623 (2003).
16. Hirasawa, M., Ishihara, T., Goto, T., Uchida, K. & Miura, N. Magnetoabsorption of the lowest exciton in perovskite-type compound (CH₃NH₃)PbI₃. *Phys. B* 201, 427–430 (1994).

17. Odier, P., Rifflet, J. C. & Loup, J. P. Electron emission measurements and the defect structure of α - Al_2O_3 . *J. Mater. Sci.* 19, 2121–2135 (1984).
18. Xing, G. *et al.* Long-Range Balanced Electron- and Hole-Transport Lengths in Organic-Inorganic $\text{CH}_3\text{NH}_3\text{PbI}_3$. *Science* 342, 344–347 (2013).
19. Stranks, S. D. *et al.* Electron-hole diffusion lengths exceeding 1 micrometer in an organometal trihalide perovskite absorber. *Science* 342, 341–344 (2013).
20. Mosconi, E., Amat, A., Nazeeruddin, M. K., Grätzel, M. & De Angelis, F. First-Principles Modeling of Mixed Halide Organometal Perovskites for Photovoltaic Applications. *J. Phys. Chem. C* 117, 13902–13913 (2013).
21. Giorgi, G., Fujisawa, J.-I., Segawa, H. & Yamashita, K. Small Photocarrier Effective Masses Featuring Ambipolar Transport in Methylammonium Lead Iodide Perovskite: A Density Functional Analysis. *J. Phys. Chem. Lett.* 4, 4213–4216 (2013).
22. Even, J., Pedesseau, L., Jancu, J.-M. & Katan, C. Importance of Spin–Orbit Coupling in Hybrid Organic/Inorganic Perovskites for Photovoltaic Applications. *J. Phys. Chem. Lett.* 4, 2999–3005 (2013).
23. Yin, W. J., Shi, T. & Yan, Y. Unusual defect physics in $\text{CH}_3\text{NH}_3\text{PbI}_3$ perovskite solar cell absorber. *Appl. Phys. Lett.* (2014).
24. Lindblad, R. *et al.* Electronic Structure of $\text{TiO}_2/\text{CH}_3\text{NH}_3\text{PbI}_3$ Perovskite Solar Cell Interfaces. *J. Phys. Chem. Lett.* 5, 648–653 (2014).
25. Umebayashi, T., Asai, K., Kondo, T. & Nakao, A. Electronic structures of lead iodide based low-dimensional crystals. *Phys. Rev. B* 67, 155405 (2003).

CHAPTER 6

Photoinduced processes at the heterojunction of $\text{CH}_3\text{NH}_3\text{PbI}_3$

The results in this chapter were adapted from two publications: Kim, H. et al., *Lead Iodide Perovskite Sensitized All-Solid-State Submicron Thin Film Mesoscopic Solar Cell with Efficiency Exceeding 9%*. Sci. Rep. 2, 591; DOI:10.1038/srep00591 (2012)¹ and Marchioro, A. et al., *Unravelling the mechanism of photoinduced charge transfer processes in lead iodide perovskite solar cells*, Nature Photon., 8, 250-255, DOI:10.1038/NPHOTON.2013.374 (2014).² In this chapter, perovskite samples were contacted either with an electron extraction layer such as TiO_2 , or deposited on an inert scaffold to resolve the electron injection step. Hole injection dynamics was also monitored by interfacing the perovskite material with the hole extracting layer spiro-MeOTAD. By using a combination of time-resolved techniques, including femtosecond and nanosecond transient absorption, terahertz spectroscopy and photoconductance measurements, both reactions were evidenced. Our findings allow determining a timescale and a mechanistic pathway for these reactions.

6.1 Introduction

As hybrid organic-inorganic lead halide perovskites can cumulate functions of light absorption, *n*-type conduction³ and *p*-type conduction⁴ as described in Chapter 1, the current picture for the hybrid *spiro*-MeOTAD | perovskite | TiO₂ cell could be seen in the following way (Figure 6.1): The perovskite absorbs light and electron-hole pairs are created in the material, which can possibly evolve towards the formation of excitons after thermalisation of the carriers. Charge separation can then occur through two possible primary reactions: injection of photogenerated electrons into TiO₂ nanoparticles (Equation 1a) and/or injection of holes (Equation 2a) into a hole transport material (HTM), such as *spiro*-MeOTAD. However, which electron or hole injection process occurs first and, in the latter case, whether electron injection into and transport within the oxide mesoporous film (Equation 2b) is playing any role is so far unclear. The precise role of titanium dioxide in efficient perovskite solar cells based on mesoporous films of this particular metal oxide has indeed not been clearly established. While evidence has been found for electron injection from the mixed halide CH₃NH₃PbI₂Cl into TiO₂,^{3,5} the same material was also reported to yield efficient photovoltaic conversion once dispersed on an insulating alumina framework, in which electron injection is not energetically feasible and where no *sensitization* of the oxide material can be invoked.³

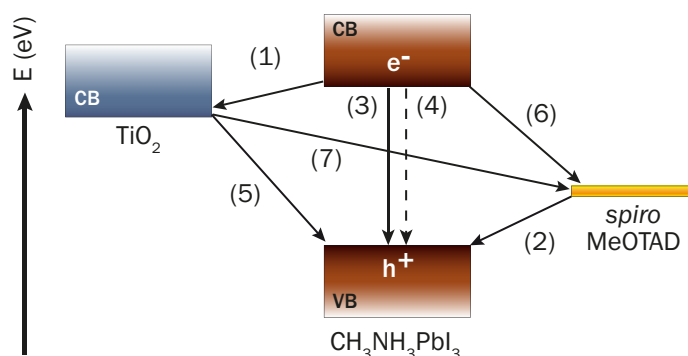
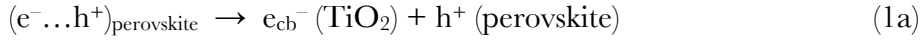
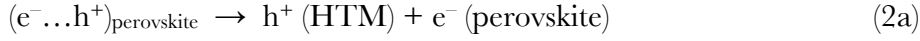


Figure 6.1 Schematic diagram of energy levels and electron transfer processes in a HTM | perovskite | TiO₂ cell

Electron injection as the primary charge separation step:



Hole injection as the primary charge separation step (the arrow is in the direction of electron transfer):



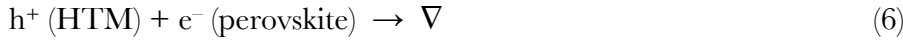
Exciton annihilation:



Back electron transfer at the TiO₂ surface:



Back charge transfer at the HTM surface:



Charge recombination at the TiO₂ | HTM interface:



Undesired reactions such as exciton annihilation, leading to photoluminescence (Equation 3) or to non-radiative recombination (Equation 4), as well as recombination of the charge carriers at the three interfaces (Equations 5-7) compete with the extraction of the photogenerated charges. Kinetics of these processes is thus expected to control to a large extent the overall photovoltaic conversion efficiency of the system. In this work, we applied time-resolved spectroscopy techniques to assess the individual dynamics of all occurring interfacial photoinduced charge transfer processes and to derive the effective mechanism for charge separation. This information is of paramount importance for the understanding of the functioning of the devices and eventually for the improvement of their photovoltaic performances.

All the measurements were always done comparatively on samples deposited on an electron injecting scaffold (TiO_2) and an electron insulating scaffold (Al_2O_3). Due to the mismatch of the energies of the conduction bands of Al_2O_3 and the perovskite, electron injection is not thermodynamically feasible in this oxide. On alumina, and in the absence of HTM, the only possible pathway for energy conservation after light absorption is electron-hole recombination, either through luminescence or non-radiative processes (Equations 3, 4). Comparison with TiO_2 samples thus allows evidencing electron injection (Equation 1a) and subsequent back charge transfer and recombination processes at the TiO_2 surface (Equations 5, 7) once the HTM is introduced in the system. A high power conversion efficiency of the photovoltaic device must obviously imply that the charge recombination processes (Equations 3-7) occur on a much slower timescale compared to charge separation and extraction processes (Equations 1, 2). It is therefore crucial to determine the kinetics of these reactions for ultimately improving the cell's performance.

6.2 Methods

6.2.1 Samples preparation

This section describes the two different ways of preparing the perovskite samples for laser spectroscopy measurements. The single-step deposition method was used for experiments reported in section 6.3 while the sequential deposition method, believed to yield more conformal films,⁶ was used for samples of section 6.4.

Single-step deposition method

Photoanodes for the transient absorption experiments in section 6.3 were prepared by Hui-Seon Kim and Soo-Jin Moon (LPI, EPFL). A hydroiodic acid (30 ml, 0.227 mol, 57 wt.% in water, Aldrich) and methylamine (27.8 ml, 0.273 mol, 40% in methanol, TCI) were stirred in an ice bath for 2 h. After stirring at 0°C for 2 h, the resulting solution was evaporated at 50°C for 1 h and produced ($\text{CH}_3\text{NH}_3\text{I}$). The precipitate was washed three times with diethyl ether, dried under vacuum, and used without further purification. To prepare (CH_3NH_3) PbI_3 , readily synthesized $\text{CH}_3\text{NH}_3\text{I}$ (0.395 g) and PbI_2 (1.157 g, 99% Aldrich) were mixed in γ -butyrolactone (2 ml, 99% Aldrich) at 60°C and left overnight with stirring. Home-made anatase TiO_2 and Al_2O_3 nanoparticles were

synthesized as previously described.¹ Thickness of the TiO_2 films was ca. 1 μm .

Sample preparation for THz experiments consisted in the following steps : a 10 nm TiO_2 layer was deposited on microscopic quartz slides by ALD to ensure adhesion of the mesoporous oxide films on quartz. TiO_2 and Al_2O_3 pastes were home made. For both oxides, a few drops of the paste were deposited on the ALD-treated quartz and spin-coated at 2000 rpm for 20 s. The TiO_2 film had an average thickness of ca. 500 nm. The procedure was repeated twice for Al_2O_3 and yielded films of ca. 200 nm thickness. The films were then dried at 125°C for 5 min and subsequently sintered at 500°C for 30 min. To prepare $\text{CH}_3\text{NH}_3\text{PbI}_3$, $\text{CH}_3\text{NH}_3\text{I}$ (0.1975 g, synthesized according to the procedure already reported and described above)¹ and PbI_2 (0.5785 g, 99% Aldrich) were mixed in 1 ml γ -butyrolactone at 60° C and left with stirring overnight. The preparation of the hole transport material solution was achieved as follows : 218 mg of *spiro*-MeOTAD (Merck KGaA) was dissolved in 1 ml chlorobenzene (99,8%, Aldrich). 30.4 μl of 4-tert butylpyridine (tBP) was added. 197 mg of bis(trifluoromethane)sulfonimide lithium salt solution (LiTFSI, 99.95%, Aldrich) were predissolved in 1 ml acetonitrile (99.8%, Aldrich). 100 μl of this solution was added to the *spiro*-MeOTAD solution. 35 μl of the perovskite solution was spin-coated on the substrates (20 s infiltration time, 2000 rpm for 30 s). Substrates were then dried for 15 min at 100°C. Samples containing HTM were prepared by spin-coating 30 μl of the *spiro*-MeOTAD solution (15 s infiltration time, 4000 rpm for 30 s) on top of the perovskite film.

Sequential deposition method

Photoanode preparation for microwave conductivity experiments of section 6.4 was performed by Thomas Moehl (LPI, EPFL). TiO_2 and Al_2O_3 pastes for the preparation of substrate films were chosen as similar as possible with regard to porosity and particle size. A commercial TiO_2 paste (Dyesol 18 NR-T, 18 nm average nanoparticle diameter) was used diluted 1: 3 in weight in EtOH, and yielded mesoporous films with 24 nm average pore size. A home-made alumina paste, with 17 nm average nanoparticle diameter, was used diluted 1: 3 in weight in EtOH, yielding films with 32 nm average pore size.

100 μl of the TiO_2 and Al_2O_3 pastes were spin-coated on 2 x 2 cm glass microscope slides (5000 rpm, 1000 rpm s^{-1} , 30 s). The films were then dried 15 min at 100°C and sintered

for 30 min at 500°C. These conditions yielded an average thickness of 400 nm for the TiO₂ and 270 nm for the Al₂O₃ films, as measured by AFM (Asylum Research Chypher). PbI₂ (99%, Sigma-Aldrich) was dissolved in DMF at 70°C to yield a concentration of 1 M. 100 ml of the PbI₂ solution was spin-coated on the mesoporous substrates (6500 rpm, 5500 rpm s⁻¹, 30 s). The films were then dried for 15 min at 70°C. Methylammonium iodide was synthesized according to a reported procedure⁷ and a solution of 20 mg/ml of CH₃NH₃I in isopropanol was prepared. PbI₂ substrates were immersed in this solution for 100 s, leading to a drastic color change of the film from yellow to dark brown. The films were rinsed in isopropanol for 10 s.

A solution of *spiro*-MeOTAD (Merck KGaA) was prepared by dissolving 90 mg in 1 ml chlorobenzene at 60°C. 8.75 µl of 4-tert-butylpyridine (tBP, Sigma-Aldrich) was added to the latter chlorobenzene solution to yield a concentration of 0.06 M tBP. 17 mg of lithium bis(trifluoromethylsulfonyl)imide (LiTFSI) (Sigma-Aldrich) was pre-dissolved in 100 µl of acetonitrile, and 18.75 µl of this solution was added to the same chlorobenzene solution to yield a concentration of 0.011 M LiTFSI. 80 µL of the *spiro*-MeOTAD solution with tBP and LiTFSI added was deposited onto the perovskite films and allowed to infiltrate for 10 s in order to maximize the penetration of the HTM prior to spin-coating (4000 rpm, 770 rpm s⁻¹, 30 s). All spin-coating operations were carried out in a dry glovebox under Ar atmosphere. After preparation, samples were placed under vacuum for a few minutes, stored in the glovebox and finally encased in a sealed cell containing Ar to avoid contact with air and oxygen during measurements.

6.2.2 Spectroscopic characterization

Femtosecond transient absorption with WLC probe

More details about the experimental setup can be found in Chapter 2. Transient absorption spectra were recorded using femtosecond pulsed laser pump-probe spectroscopy. The pump beam (580 nm) was generated with a commercial two-stage non-collinear optical parametric amplifier (NOPA) from the 778 nm output of a Ti:Sa laser system with a regenerative amplifier providing 150 fs pulses at a repetition rate of 1 kHz. The pump beam was compressed with a pair of SF-10 prisms to sub-50 fs pulses and the pump energy at the sample was at 200 nJ with a spot size diameter of 1 mm. The probe consisted of a white light continuum (400-800 nm), generated by passing a portion of the

778 nm amplified Ti:Sa output through a 5 mm-thick sapphire plate. The probe intensity was always less than the pump intensity and the spot size was much smaller. The probe pulses were time delayed with respect to the pump pulses using a computerized translation stage. The probe beam was split before the sample into a signal beam (transmitted through the sample and crossed with the pump beam) and a reference beam. The signal and reference were detected with a pair of 163 mm spectrographs (Andor Technology, SR163) equipped with 512x58 pixels back-thinned cameras (Hamamatsu S07030-0906), assembled by Entwicklungsbüro Stresing, Berlin. The pump light was chopped at half the amplifier frequency, and the transmitted signal intensity was recorded shot by shot. It was corrected for intensity fluctuations using the reference beam. The transient spectra were averaged until the desired signal-to-noise ratio was achieved (typically 3000 acquisitions). The polarization of the probe pulses was at magic angle relative to that of the pump pulses. All spectra were corrected for the chirp of the white-light probe pulses.

Optical-pump THz-probe measurements

Optical-pump THz-probe spectroscopy is a purely optical technique to measure charge dynamics on an ultrafast time scale. The experimental setup can briefly be described as follows. The initial pulsed laser beam (1 kHz repetition rate, 45 fs pulse duration, 4.5 mJ/ pulse energy, 800 nm wavelength) provided by an amplified Ti:Sa laser (Coherent Libra USP HE) is split into different paths. Approximately 1.4 mJ/ pulse is used to pump an OPerA-Solo optical parametric amplifier (Coherent), which is used as an optical pump to photo-generate carriers in the sample. A second part of the beam with approximately 0.9 mJ/ pulse energy is used to generate single cycle THz pulses by optical rectification in a 1 mm-thick ZnTe crystal. The THz beam is focused by gold mirrors on the sample and used as a probe. The transmitted THz pulses are detected in the time-domain through free space electro-optic sampling. A third part of the initial laser beam is used as a gating beam and guided over a delay line onto a 0.5 mm-thick ZnTe detector crystal. By varying the time delays between the optical pump, the THz probe pulse and the gating, amplitude and phase changes of the THz single-cycle pulses can be recorded. Changes of the amplitude of the THz pulses upon photo-excitation were measured in this work on a time scale of up to 1 ns with sub-ps time resolution. The pump beam was set at 580 nm and the typical power at the sample was 0.5 mW for a pump diameter of 2.7 mm corresponding to a fluence of ca. 9 $\mu\text{J}/\text{cm}^2$.

Monochromatic femtosecond transient absorption

More details about the experimental setup can be found in chapter 2. Transient absorption spectra were recorded using femtosecond pump-probe spectroscopy. The pump beam ($\lambda_{\text{exc}} = 580 \text{ nm}$) was generated by pumping a two-stage non-collinear optical parametric amplifier (NOPA) by the 778 nm output of an amplified Ti:Sa laser system providing 150 fs duration pulses at a repetition rate of 1 kHz. The pump beam was compressed with a pair of SF-10 prisms to sub-50 fs pulses. The probe beam ($\lambda_{\text{probe}} = 1.4 \mu\text{m}$) was generated by a second OPA (Light Conversion, TOPAS model 4/800) and used without any compression (pulse duration ca. 150 fs). The change in transmittance of the sample, i.e. change in intensity of the probe beam, was measured by an InGaAs photodiode (New Focus, model Nirvana 2017) protected by cut-off filters to avoid any scattered light from the pump. The low-amplitude signal was extracted by a lock-in amplifier (SR-830, Stanford Research) referenced to the chopper frequency. The pump energy at the sample was 360 nJ/pulse with a spot size diameter of ca. 560 μm . Temporal overlap between the pump and probe pulses at the sample position was measured with a Kerr gating technique and gave typical instrument response function (IRF) of 180 fs.

Time-resolved microwave conductivity measurements

Time-resolved microwave conductivity measurements were conducted by Dennis Friedrich and Marinus Kunst at the Institute for Solar Fuels in Berlin. Transient photoconductance measurements in the microwave frequency range were performed by using a Ka-band (28.5 - 40 GHz) apparatus as described previously.⁸ Samples were excited by 10 ns (FWHM) pulses of a frequency-doubled Q-switched Nd:YAG laser at a wavelength of 532 nm with a beam diameter of about 1.6 mm. The excitation intensity was adjusted by the use of calibrated filters and set to 1.2 mJ/cm² for samples on mesoporous films, while 7 $\mu\text{J}/\text{cm}^2$ were used for samples deposited on glass, that contained more perovskite material.

Nanosecond flash photolysis

More details about the experimental setup can be found in Chapter 2. Transmission-mode transient absorption spectroscopy experiments were conducted using a frequency-tripled,

Q-switched Nd:YAG laser (Continuum, 20 Hz repetition rate) pumping an optical parametric oscillator (OPO-355, GWU). The output wavelength of the OPO was tuned at $\lambda_{\text{exc}} = 580$ nm (7 ns pulse duration) and attenuated to $70 \mu\text{J}/\text{cm}^2$. The cw probe light from a Xe arc lamp was passed through various optical elements, the sample, and a monochromator ($\lambda_{\text{probe}} = 1.4 \mu\text{m}$) before being detected by an InGaAs photodiode with $1 \text{ k}\Omega$ load (SM05PD5A, Thorlabs). Averaging over at least 2,000 laser shots was used. Dynamics were recorded over 10,000 points and a 2nd order Savitzky-Golay smoothing algorithm on 45 points was applied.

6.3 Hole injection into *spiro*-MeOTAD

6.3.1 Femtosecond transient absorption

Femtosecond transient absorption studies have been performed in order to elucidate the mechanism of charge separation in the device. Four different samples, $\text{CH}_3\text{NH}_3\text{PbI}_3 \mid \text{TiO}_2$, with and without *spiro*-MeOTAD, as well as $\text{CH}_3\text{NH}_3\text{PbI}_3 \mid \text{Al}_2\text{O}_3$, with and without *spiro*-MeOTAD, have been measured with 580 nm pulsed fs laser excitation and white light continuum (WLC) probing between 440 and 740 nm. The photophysical properties $\text{CH}_3\text{NH}_3\text{PbI}_3$ have been extensively discussed in Chapter 5, and thus the spectral features will only be briefly reminded here. Figure 6.2a shows results obtained for the samples deprived from HTM. Similar spectral signatures can be observed: negative signal peaking at 480 nm is attributed to the bleaching of the ground state species of the perovskite, while the positive absorption signal in the 630-700 nm region is ascribed to the excited state absorption. Furthermore, the negative peak starting after 700 nm on both samples is attributed to stimulated emission and matched the results obtained by steady-state emission.¹ The possible contribution of a photobleaching to the stimulated emission is discussed in Chapter 5 and will not be referred to here. The spectra recorded at 300 fs time-delay shows the progressive shift of the stimulated emission peak while the bleaching in the blue region is already present.

The small differences observed between TiO_2 and Al_2O_3 are not significant enough to draw any conclusion regarding the electron injection process; the recovery of the initial state in 1 ns for both samples shows that no electron injection can be evidenced on these

samples, thus matching very well the observed stimulated emission, fingerprint of an excited state living over 1 ns.

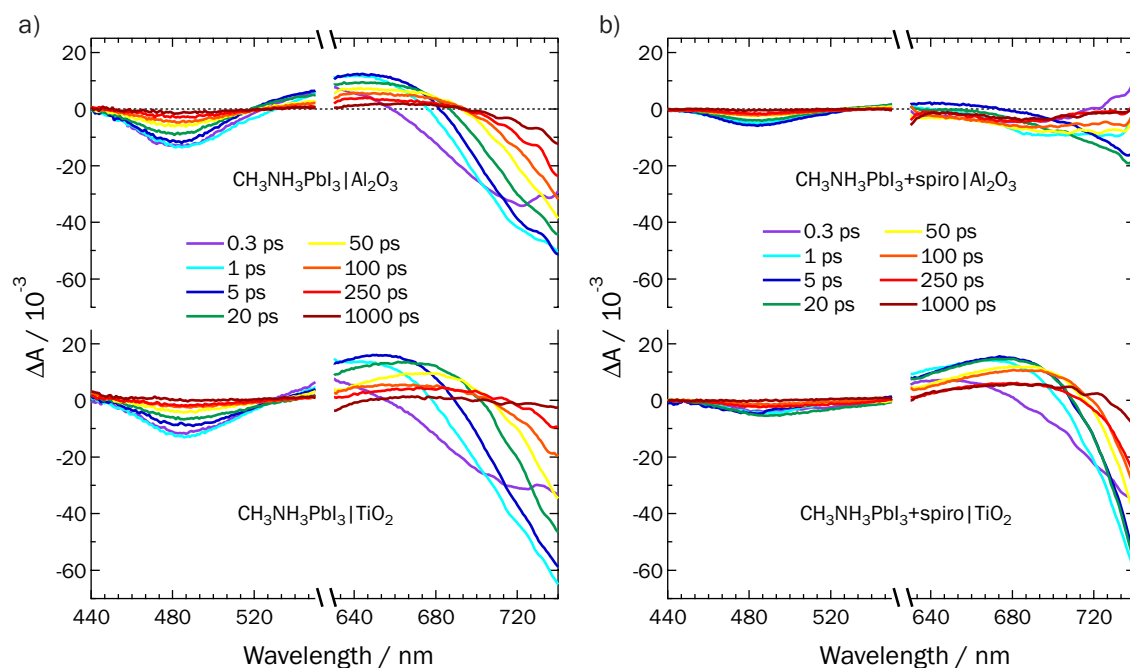


Figure 6.2 Femtosecond transient absorbance spectra with white light continuum probe and pulsed fs laser excitation at 580 nm

a) $\text{CH}_3\text{NH}_3\text{PbI}_3 | \text{Al}_2\text{O}_3$ and $\text{CH}_3\text{NH}_3\text{PbI}_3 | \text{TiO}_2$, b) *spiro*-MeOTAD | $\text{CH}_3\text{NH}_3\text{PbI}_3 | \text{Al}_2\text{O}_3$, and *spiro*-MeOTAD | $\text{CH}_3\text{NH}_3\text{PbI}_3 | \text{TiO}_2$, recorded at various time delays after excitation (color lines). Bleaching is evident with maximum at 480 nm, while the positive absorption signal in the 630 to 700 nm region corresponds to the excited state absorption. Negative feature in the red part of the spectra is attributed to stimulated emission. All features are quenched upon addition of the HTM.

Samples with hole conductor give another interesting insight on the working mechanisms of the perovskite-based cell (Figure 6.2b). WLC spectrum of *spiro*-MeOTAD | $\text{CH}_3\text{NH}_3\text{PbI}_3 | \text{TiO}_2$ shows the same spectral features of the one without *spiro*-MeOTAD, with the bleaching peak in the blue region being less pronounced than in the case of $\text{CH}_3\text{NH}_3\text{PbI}_3 | \text{TiO}_2$ sample. This could be either due to a fast recovery of the ground state, or absorption of the oxidized *spiro*-MeOTAD that has spectral signatures in the visible region.⁹ Either ways, the result is that quenching of the excited state of the perovskite by the HTM has occurred. Moreover, the stimulated emission peak appears to be less pronounced than in the aforementioned case, suggesting that a quenching of the stimulated emission is occurring.

In the case of *spiro*-MeOTAD | $\text{CH}_3\text{NH}_3\text{PbI}_3 | \text{Al}_2\text{O}_3$, the amplitude of the 480 nm bleaching was found to be smaller than on a sample without hole conductor, as discussed previously for the *spiro*-MeOTAD | $\text{CH}_3\text{NH}_3\text{PbI}_3 | \text{TiO}_2$ sample. More interestingly, the

positive peak in the 630-700 nm region completely disappeared, concomitantly with a net decrease of the stimulated emission negative peak. The results indicates a rapid quenching of the excited state by the *spiro*-MeOTAD through hole injection (Equation 2), occurring in less than 1 ps. Indeed, Figure 6.3 compares the dynamics obtained for $\text{CH}_3\text{NH}_3\text{PbI}_3 | \text{Al}_2\text{O}_3$ and *spiro*-MeOTAD | $\text{CH}_3\text{NH}_3\text{PbI}_3 | \text{Al}_2\text{O}_3$. The results clearly indicates that the quenching occurs very fast, as the amplitude is greatly decreased in the laser pulse resolution (< 150 fs), and the sample with HTM shows the competition between a positive and a negative signal in the first ps, also denoting the complex spectral overlap of the absorption bands of these materials. This reductive quenching by the HTM (as described by equation 2a, in absence of an electron acceptor) thus extracts a hole from the perovskite and leaves behind an electron, thus effectively decreasing the photoluminescence. The kinetics of hole injection in the *spiro*-MeOTAD can then be estimated to be inferior than our current 150 fs temporal resolution.

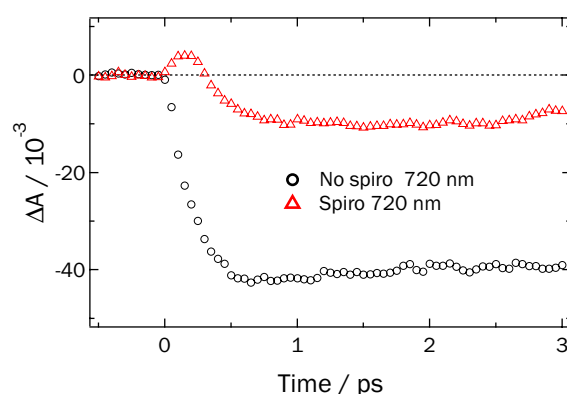


Figure 6.3 Dynamics extracted at 720 nm for $\text{CH}_3\text{NH}_3\text{PbI}_3 | \text{Al}_2\text{O}_3$

Black circles: sample without *spiro*-MeOTAD; Red triangles: sample with *spiro*-MeOTAD. The initial amplitude is decreased upon addition of HTM and shows a first positive feature that is not visible in the case of the sample without HTM, when a large amount of stimulated emission is present.

The difference in the amplitude of the quenching observed between TiO_2 and Al_2O_3 films might be related to the morphology, as for these experiments, the porosity of the films used was not the same and a difference in homogeneity of the films could be noticed (perovskite film deposited on Al_2O_3 being always more homogeneous). This difference in morphology is likely to be linked to a better pore filling by *spiro*-MeOTAD in the case of Al_2O_3 , explaining thus why the reductive quenching by *spiro*-MeOTAD (Equation 2a) seems to be more efficient in this case. Further studies showed that the amount of quenching is highly variable, and indeed, samples prepared according to the same experimental conditions as above were found to have the inverse behavior, i.e. quenching was more efficient on a

TiO₂ sample (data not shown). This indicates that a fundamental parameter governing the contact between the perovskite and the HTM is not yet fully understood, at least while using the spin-coating deposition method for the perovskite.

6.3.2 THz spectroscopy

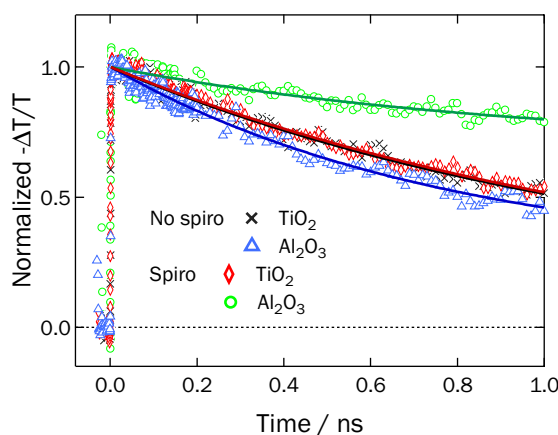


Figure 6.4 Terahertz measurements of the CH₃NH₃PbI₃ deposited on various substrates

Terahertz transient signal following fs laser pulsed excitation at 580 nm. Signals reflect the time-evolution of electrons and holes population in the active layer. Black crosses: CH₃NH₃PbI₃ on TiO₂; blue triangles: CH₃NH₃PbI₃ on Al₂O₃; red diamonds: CH₃NH₃PbI₃ and *spiro*-MeOTAD on TiO₂; green circles: CH₃NH₃PbI₃ and *spiro*-MeOTAD on Al₂O₃. Thick lines are shown as guide to the eye.

Preliminary THz experiments are shown to support results found by TAS. THz probes the photoconductivity of the samples, i.e. the product of the mobility and the concentration of charge carriers. The photoconductivity in the active layer arises mainly from the charges in the perovskite material and not from electrons injected in TiO₂. This is inferred from the observation that the observed signal is very similar in amplitude both on TiO₂ and on Al₂O₃, where no signal from carriers injected in the metal oxide can contribute to the photoconductivity. Figure 6.4 shows normalized transient THz signal for TiO₂ and Al₂O₃ mesoporous films, with and without the hole transport material *spiro*-MeOTAD. Thus, following pulsed laser excitation at 580 nm, decay of THz signal reflects the time-evolution of the population of mobile charge carriers. Decays were acquired over 1 ns and were qualitatively compared, thick lines are shown as a guide to the eye. Normalized dynamics for TiO₂ with and without HTM as well as Al₂O₃ sample without HTM were found to be in the same range, slightly slower in the case TiO₂ without HTM. This tends to indicate that charge separation occurs through electron injection (Equation 1), but once again the effect is not as striking as in the case of Al₂O₃ sample impregnated with HTM. In this latter case, the dynamics appears to be much slower, thus

suggesting that charge separation through hole injection (Equation 2) is taking place at the heterojunction, which is less evident in the case of the TiO_2 sample with HTM. This result matches what is observed in transient absorption data reported above, as the efficiency of the quenching by *spiro*-MeOTAD is more efficient in the case of the Al_2O_3 sample impregnated with HTM. Hence, in the case of THz signal, no clear conclusion on the electron injection pathway can be drawn with regard to TiO_2 samples, however this might be related to the sensitivity of the measurement itself, or as in the case of the section 6.3.1, an insufficient contact between TiO_2 , perovskite, and the HTM.

While revealing the hole injection pathway (Equation 2), these studies do not allow to highlight the pathway of electron injection (Equation 1). The next paragraphs will bring evidence for this first mechanism, as well as confirming the hole injection pathway already observed.

6.4 Electron injection into TiO_2

The dynamics of the various charge transfer processes were first assessed through probing optical transient absorption signals in the near-infrared with $\text{CH}_3\text{NH}_3\text{PbI}_3$ deposited either in mesoporous TiO_2 or Al_2O_3 films in the absence of HTM. Pairs of samples prepared on Al_2O_3 and TiO_2 films with *spiro*-MeOTAD impregnating the mesoporous oxides were also measured. To support and complement the mechanistic picture of the processes, time-resolved photoconductance measurements in the microwave frequency range were also performed. Additional information on the recombination reactions (Equations 6 and 7) is then provided by nanosecond transient absorption experiments.

6.4.1 Ultrafast transient optical absorption spectroscopy

Femtosecond pump-probe transient absorption experiments were carried out at a probe wavelength of 1.4 μm and an excitation wavelength of 580 nm for $\text{CH}_3\text{NH}_3\text{PbI}_3$ samples deposited on TiO_2 and on Al_2O_3 films, with and without HTM. Resulting transient absorption was found in all cases to rise within the first ps (Figure 6.5). The decay of the signal traces was observed to be multi-exponential for all samples and was fitted with a double exponential starting at $t = 1$ ps. The corresponding fast component developed within 40-60 ps for all samples, while a slower component appeared in the 140-270 ps time

range. The 1.4 μm probe wavelength was initially selected to probe oxidized *spiro*-MeOTAD, which absorbs in the near-IR.^{9,10} However, samples deprived of HTM yielded an important transient absorption signal originating from the perovskite itself. Comparing the signals obtained on the two different metal oxides, it is inferred that they reflect the time-evolution of the $\text{CH}_3\text{NH}_3\text{PbI}_3$ photoexcited states population. These excited states correspond to photogenerated electrons and holes, which can either be paired in excitons or exist in the form of free or even trapped charge carriers. In systems prepared on TiO_2 films, a small contribution to the transient absorption signal of conduction band electrons injected in TiO_2 cannot be excluded. Similarly, for all systems containing *spiro*-MeOTAD HTM, contributions to the transient absorption signal of oxidized HTM species cannot be omitted and will be discussed later.

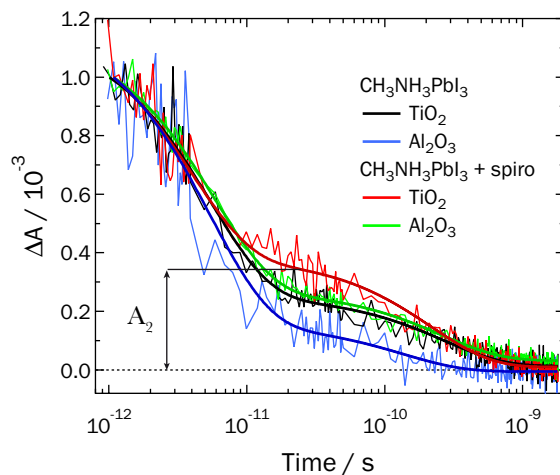


Figure 6.5 Time-evolution of electrons and holes population in photoexcited $\text{CH}_3\text{NH}_3\text{PbI}_3$ perovskite in various systems

Transient absorption signals were measured at a probe wavelength of 1.4 μm following fs laser pulsed excitation at 580 nm. — $\text{CH}_3\text{NH}_3\text{PbI}_3$ on TiO_2 ; — $\text{CH}_3\text{NH}_3\text{PbI}_3$ on Al_2O_3 ; — $\text{CH}_3\text{NH}_3\text{PbI}_3$ and *spiro*-MeOTAD on TiO_2 ; — $\text{CH}_3\text{NH}_3\text{PbI}_3$ and *spiro*-MeOTAD on Al_2O_3 . Thick solid lines represent bi-exponential fits of experimental points starting at $t = 1$ ps. A_2 represents the normalized absorbance change at 25 ps, used as a metrics to compare the various samples.

In the case of samples without HTM, a transient signal arising from the perovskite deposited on Al_2O_3 was observed and attributed to the decay of the carriers' population through recombination within the absorber material (blue trace on Figure 6.5) as no interfacial reaction can take place in this case. Transient absorbance of a perovskite | TiO_2 sample shows that the relative signal amplitude of the slower part, defined as the normalized absorbance change at 25 ps, is larger than on Al_2O_3 (Table 6.1, 24 % and 14 %, respectively). This relative signal amplitude is subsequently used as a

metrics to compare the various samples. We will assume in the following discussion that charge recombination within the perovskite is similar on TiO_2 and on Al_2O_3 samples. This assumption is corroborated by the observation in the transient photoconductance (TPC) measurements (Figure 6.6), that the charge decay within the perovskite is not influenced by deposition on a mesoporous framework with respect to perovskite deposited as a flat film on glass. For reasons that will be discussed later in the text, the contribution to the transient absorption signal of electrons injected in TiO_2 conduction band is believed to be negligible. In this perspective, the larger relative amplitude for the slower part of the decay observed for the perovskite in contact with titania indicates that some of the charges have already been separated through ultrafast electron injection (Equation 1a). The latter process leaves then an excess of holes in the perovskite that take longer to recombine with remaining electrons, whose population has been depleted. Accordingly, the presence of a minor plateau after 300 ps is then attributed to remaining carriers, in this case holes, that have not yet been able to recombine with electrons that have been injected into TiO_2 . As the decay curves for the TiO_2 case starts lagging behind that of the Al_2O_3 case at delay times ≥ 3 ps (Figure 6.5, black and blue curves, respectively), it is inferred that charge separation must occur at the perovskite | titania junction on a similar or shorter time scale.

Table 6.1 Ratio of the amplitude A_2 measured on data displayed in Figure 6.5

Values taken at $t = 25$ ps relative to the total normalized amplitude ΔA_0 at 1 ps, for $\text{CH}_3\text{NH}_3\text{PbI}_3$ on TiO_2 and Al_2O_3 , with and without *spiro*-MeOTAD HTM.

$A_2 / \Delta A_0$	without HTM	with HTM
TiO_2	0.24	0.34
Al_2O_3	0.14	0.26

Pairs of samples prepared on Al_2O_3 and TiO_2 films were also measured with *spiro*-MeOTAD impregnating the mesoporous oxides. Interestingly, for a sample of Al_2O_3 with HTM, the relative amount of remaining charges at a delay time of 25 ps is similar to what we observed on the previously discussed sample prepared on TiO_2 and deprived from *spiro*-MeOTAD (Table 6.1, 26 % relative amplitude). This indicates that hole injection into the HTM (Equation 2a) must be completed within a comparable timescale as electron injection into TiO_2 (Equation 1a). In the case of perovskite in contact with both TiO_2 and the HTM, the amount of longer-lived charges is higher (Table 6.1, 34 % relative

amplitude). This result shows that the most efficient charge separation is obtained when using TiO_2 and HTM together, and is rationalized by the fact that the recombination of the remaining charges in the perovskite must account for charges that are injected at both separate junctions (TiO_2 | perovskite and perovskite | HTM). Here, contrary to the case of the perovskite deposited on alumina and in contact with the HTM, no residual absorption is observable on the ns time scale, as every carrier in the perovskite should have found an opposite charge to recombine with. It could be argued that the long-lived absorption actually results from the contribution of oxidized *spiro*-MeOTAD molecules – $\text{h}^+(\text{HTM})^-$, as well as that of conduction band electrons in TiO_2 , as both species absorb at 1.4 μm .⁹⁻¹¹ However, this statement would not change the conclusion, as it would also provide a direct evidence of charges having been separated at the junctions. Yet, we believe that these contributions are negligible in our measurements. Indeed, the reactions of recombination of $\text{e}_{\text{cb}}^- (\text{TiO}_2)$ or $\text{h}^+(\text{HTM})$ with carriers in the perovskite (Equations 5, 6) are likely to be slower than a nanosecond (we show hereafter that this second reaction actually lies in the microsecond timescale), and thus this would appear as a long-lived plateau in the dynamics of the $\text{TiO}_2 + \text{HTM}$ sample, that we do not observe in this case.

6.4.2 Time-resolved microwave photoconductance measurements

As a complementary technique, we used time-resolved photoconductance (TPC) measurements in the microwave frequency range to monitor directly mobile charge carriers' population within the perovskite material. The effect of electron injection from the perovskite into the mesoporous TiO_2 and the resulting increase in charge carrier lifetime was observed with a 10 ns time-resolution (Figure 6.6). No TPC signal was detected for pure TiO_2 or Al_2O_3 films at the light intensities and excitation wavelength (532 nm) used in these experiments, showing that the observed photoconductance phenomena are induced only by photon absorption in the perovskite. As a result of charge separation or exciton splitting, an increase in the lifetime of the separated charge carriers can normally be observed. In case that the perovskite is deposited on Al_2O_3 without any HTM present, one can expect an annihilation of the absorbed photon energy by luminescence or thermalisation. This can be clearly seen in Figure 6.6, where no significant difference between a pure perovskite film on glass and the perovskite deposited on Al_2O_3 can be observed. In the case where the perovskite is deposited on TiO_2 , an

extension of the decay time is observed, evidencing the separation of the electron-hole pair and therefore the injection of electrons into titanium dioxide.

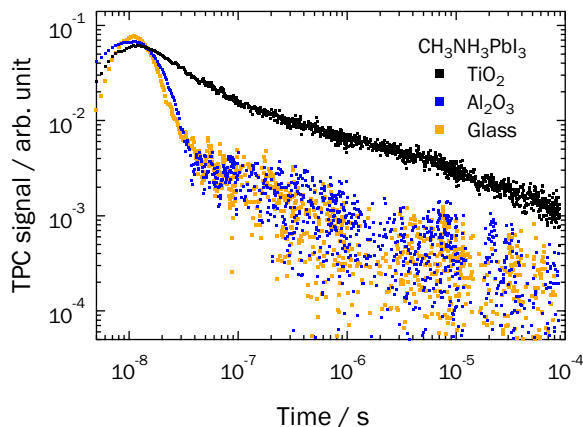


Figure 6.6 Transient microwave photoconductance measurements of the perovskite material deposited on various substrates

Black dots: $\text{CH}_3\text{NH}_3\text{PbI}_3$ on mesoporous TiO_2 ; Blue dots: $\text{CH}_3\text{NH}_3\text{PbI}_3$ on mesoporous Al_2O_3 ; Orange dots: $\text{CH}_3\text{NH}_3\text{PbI}_3$ on flat glass. The build-up rate of the TPC signal is here limited by the excitation laser pulse duration (~ 10 ns).

6.4.3 Nanosecond transient optical absorption spectroscopy

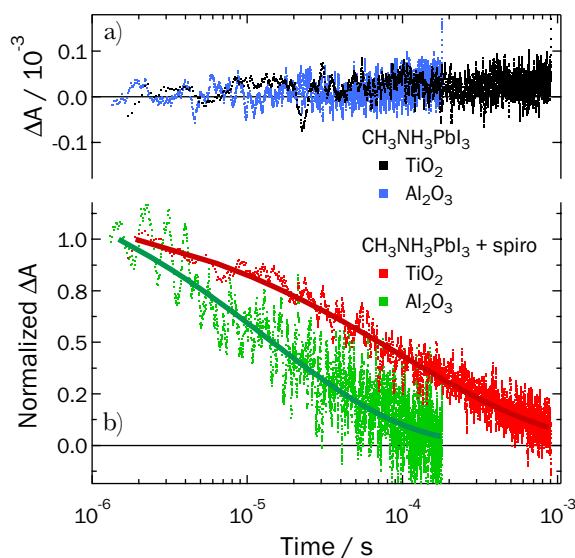


Figure 6.7 Charge recombination dynamics obtained from ns-laser flash photolysis of the various systems

Transient absorption signals were monitored at $\lambda = 1.4$ μm following excitation at 580 nm. a) Samples without HTM. — $\text{CH}_3\text{NH}_3\text{PbI}_3$ on TiO_2 ; — $\text{CH}_3\text{NH}_3\text{PbI}_3$ on Al_2O_3 ; b) Samples with HTM. Signals mainly reflect the decay of h^+ (HTM) population. — $\text{CH}_3\text{NH}_3\text{PbI}_3$ and *spiro*-MeOTAD on TiO_2 ; — $\text{CH}_3\text{NH}_3\text{PbI}_3$ and *spiro*-MeOTAD on Al_2O_3 . Thick lines represent stretched exponential fit of data.

Flash photolysis experiments were carried out over an extended μs -ms time domain at a probe wavelength of 1.4 μm and an excitation wavelength of 580 nm, similarly to

femtosecond experiments. The expected transient signal in the microsecond timescale results from the absorption of the oxidized form of the *spiro*-MeOTAD – h^+ (HTM) –. Indeed, spectral overlap with charge absorption of the perovskite could be avoided at this wavelength, as the decay of these charges should be completed much earlier within the nanosecond time span. This is confirmed by transient absorption showing no signal on the microsecond domain for $CH_3NH_3PbI_3$ samples without HTM, both on TiO_2 and on Al_2O_3 (Figure 6.7a). Although we expected to observe a transient signal corresponding to conduction band electrons in the TiO_2 that do absorb at this wavelength, this contribution to the signal appears to be below the detection limit of this particular experiment. Time-evolution of transient absorbance signals at $1.4 \mu m$ for $CH_3NH_3PbI_3$ samples with HTM (Figure 6.7b) on TiO_2 and on Al_2O_3 can, therefore, be assigned to the decay of oxidized *spiro*-MeOTAD population through recombination processes. On Al_2O_3 , we observe the recombination between h^+ (HTM) and e^- (perovskite) (Equation 6), while on TiO_2 recombination occurs between h^+ (HTM) and e_{cb}^- (TiO_2) (Equation 7). The signal trace decay could be fitted with a stretched exponential (stretching exponent $\beta = 0.5$). Excitation energy fluence in this particular experiment being rather low ($70 \mu J / cm^2$, corresponding to approximately 40 photons/ nanoparticle), the stretched exponential reflects a broad distribution of distances between recombining charges. The comparison between the time constants for the decay on TiO_2 and on Al_2O_3 is quite evident and shows that recombination is slower when TiO_2 is used ($99 \mu s$ vs. $15 \mu s$ on Al_2O_3). This demonstrates that process (6) is faster than process (5). It provides therefore additional evidence that electron injection has taken place and that recombination occurs via a mechanism that involves diffusion of carriers on a larger distance.

6.5 Discussion

Intrinsic physical properties of the perovskite material, such as exciton diffusion length, carriers' mobility, nature and density of trap states, and the energetics of the bands, are obviously important to explain why this exceptional material appears to be working in a variety of configurations. Rather than dealing with the intrinsic properties of the perovskite semiconductor, the present work focuses on interfacial charge transfer processes occurring at the junctions between the light-absorber and the electron- and/or hole conducting materials. A sequence of interfacial electron transfer steps is derived from the

kinetics determined experimentally in configurations that have already proved to function efficiently in solar cells. We can then take for granted that exciton diffusion length and carriers' mobility within the perovskite are amply sufficient and that all energy levels are conveniently aligned.^{18, 19}

In samples containing the perovskite absorber deposited on the titanium dioxide electron acceptor with HTM infiltrated in the pores of the mesoscopic film, non-ideal morphologies obtained during the preparation will lead to various punctual situations within the same sample, where perovskite domains could be either insulated, contacted with the sole TiO_2 or the sole HTM, or form two junctions with both the TiO_2 and the HTM. All the different situations are now encountered in solar energy conversion devices of various architectures. The interest of the discussion on the charge transfer mechanism taking place in TiO_2 | perovskite | *spiro*-MeOTAD solid state solar cell then extends beyond this particular example to other types of perovskite-based photovoltaic systems.

Four different cases related to the morphology of the sample could coexist in perovskite-based devices:

- a) All the perovskite is conformally deposited on top of the metal oxide (be the insulating Al_2O_3 or the TiO_2 electron acceptor) as a thin light harvesting film, which thickness is at most of a few nanometres.
- b) Part of the perovskite is not in direct contact with the oxide substrate but is present in the form of isolated crystalline domains in the pores and/or of a capping layer on top of the mesoporous network.

All perovskite-based devices deposited on a mesoporous structure, regardless of the type of preparation, should fit in one of the two categories, (a) or (b). When adding an HTM, both cases can be coupled with two additional cases regarding the junction:

- c) All the HTM is conformally deposited into the pores forming a continuous junction with the perovskite material.
- d) Not enough HTM is present in the pores, or the interfacial contact between the perovskite and the HTM is only partial due to infiltration problems.

We will rationalize for each case what could be observed by time-resolved laser spectroscopy, keeping in mind what could be the influence of the contact at the various heterojunctions. In case (a), the intimate contact between the two semiconductors allows resolving unequivocally the electron injection process by direct comparison between TiO₂- and Al₂O₃-based samples. In case (b), a capping layer of perovskite that is not in direct contact with the mesoporous oxide can be found and optical features of isolated perovskite material could be observed. In the specific case of TiO₂, where we expect electron injection to take place, the presence of a capping layer would result in strong light absorption within this layer and consequently poor quenching by TiO₂ due to lacking of a good TiO₂ | perovskite interface. Consequently, a strong photoluminescence will be observed. In the absence of a good intimate contact with TiO₂, the device can still work with the perovskite playing the role of the electron transporting material, in the same way as in the so-called meso-superstructured cells built on an insulating alumina framework.³ In case (c), a hole is easily extracted at the perovskite | HTM interface, according to measurements already discussed in the beginning of this chapter (section 6.3) where the *spiro*-MeOTAD was shown to quench very efficiently perovskite's photoluminescence within a sub-ps time frame, more precisely in the laser resolution (< 150 fs). In case (d), the absence of an intimate contact between the light absorber and *spiro*-MeOTAD is likely to end up in a situation where the device resembles a *p*-type perovskite cell, where the CH₃NH₃PbI₃ works as the hole transport material.⁴ For a perovskite | HTM bilayer, in which holes have to diffuse across a 65 nm-thick absorber layer to reach the HTM junction, extraction time extends in the ps-ns timescale, much longer than in case (c).¹² Case (d) will often occur in type (b) samples, because a capping layer of perovskite tends to prevent a good infiltration of the HTM in the pores. Deposition of *spiro*-MeOTAD on a case (a) sample will on the contrary favour case (c), resulting in an optimum device.⁶

Part of the charge recombination observed in TiO₂ | perovskite | *spiro*-MeOTAD samples can still occur from electrons in the perovskite (Equation 6), if they have not been efficiently injected into the titania. This would be the case if there were insufficient contact between TiO₂ and perovskite – case (b) –. The time constant measured by flash photolysis experiments for a TiO₂ + HTM sample thus might include contributions of the recombination reactions (Equations 6, 7).

Time-resolved measurements reported in the present work highlight for the first time some of the important processes in CH₃NH₃PbI₃-sensitized samples and corresponding samples

built on an Al_2O_3 scaffold. Probing in the near infrared provided a way to circumvent the spectral overlap due to different types of morphological issues – case (a) or (b) – by observing only the carriers' population decay inside the perovskite itself rather than the bulk luminescence that constitutes the main spectral feature observed in the visible range. In the work presented in section 6.3, electron injection could not be evidenced by monitoring the stimulated emission of the perovskite, nor by THz measurements, most likely because the observed transient was originating from a capping layer of the material. The method consisting in spin-coating a mixed solution of $\text{CH}_3\text{NH}_3\text{I}$ and PbI_2 in γ -butyrolactone, originally used to produce the samples, has now been replaced by a sequential deposition method yielding more conformal films (cf. the methods in section 6.2.1). Near-infrared optical probing, which monitors the decay of the population of charges remaining in the photoexcited perovskite, is key in evidencing charge separation processes taking place through both electron and hole injection.

Comparable kinetics for the decay of the remaining recombining charges in perovskite | TiO_2 sample and *spiro*-MeOTAD | perovskite | Al_2O_3 sample reveal that both electron and hole injection occur on a similar timescale. Furthermore, it is possible to conclude that both charge separation processes happen in the fs-ps timescale as our previous study showed that hole injection, observed through stimulated emission quenching, has already taken place within the first picosecond following excitation (cf. Figure 6.2 and Figure 6.3). Direct monitoring of the dynamics of the primary charge separation is beyond the scope of this study.

The efficiency of charge extraction in a perovskite solar cell depends on the ratio between rate constants for charge recombination and charge separation. It is thus important to determine the timescale for charge recombination processes in the cell. Results obtained by flash photolysis first show that the recombination reaction for electrons and oxidized *spiro*-MeOTAD (Equations 6, 7) is slow, taking place in the microsecond range. This warrants at least a factor of 10^6 between charge separation and recombination rate constants at the HTM interface, ensuring a quantitative yield for the sustained charge separation. Additionally, reaction (7) being slower than reaction (6) proves that the use of TiO_2 as electron acceptor and transporter in conjunction with an organic HTM in contact with the perovskite is indeed quite beneficial.

6.6 Conclusion

Results presented in this chapter unravel the mechanisms of photoinduced processes in $\text{CH}_3\text{NH}_3\text{PbI}_3$ solid-state solar cells. Time-resolved techniques were applied to $\text{CH}_3\text{NH}_3\text{PbI}_3$ deposited as a conformal film on TiO_2 and Al_2O_3 samples to study the kinetics of interfacial electron transfer processes. The timescales of these processes are summarized in Figure 6.8:

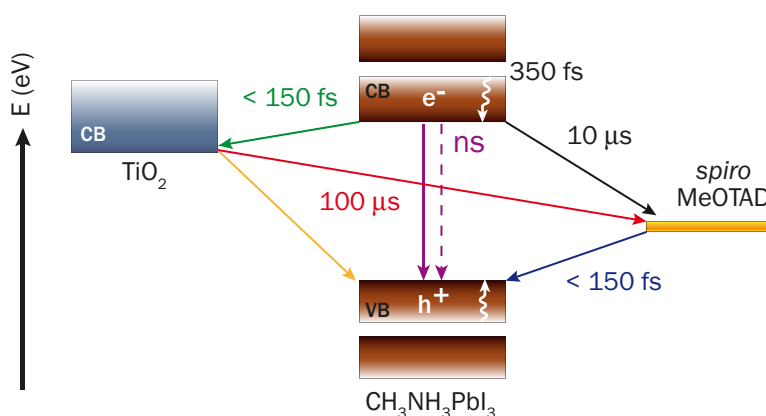


Figure 6.8 Summary of the timescales for electron transfer processes in $\text{CH}_3\text{NH}_3\text{PbI}_3$ | TiO_2

From the conclusions obtained in Chapter 5, a double-band model and thermalisation processes in 350 fs can be hypothesized. Femtosecond transient absorption spectroscopy in the visible range applied to $\text{CH}_3\text{NH}_3\text{PbI}_3$ films on TiO_2 and Al_2O_3 photoanodes reveals characteristic spectral features of this material, with the presence of a bleaching in the blue region, an excited state absorption in the 550-650 nm range and a large stimulated emission in the 700 nm region that is associated with the steady-state luminescence at 780 nm. These characteristic spectral features were not sufficient to unambiguously evidence electron injection through comparison between TiO_2 and Al_2O_3 photoanodes. However, quenching of the luminescence for samples impregnated with HTM could be correlated with the efficiency of the charge separation, and revealed that hole injection process (Equation 2) is happening on a very short timescale (< 150 fs). The apparent weaker quenching of the $\text{CH}_3\text{NH}_3\text{PbI}_3$ excited state by the HTM in the TiO_2 sample compared to the Al_2O_3 -based layer might be rationalized by a different morphology obtained on the different oxides mesoporous films. In Al_2O_3 films, a better pore filling by the *spiro*-MeOTAD could offer a better contact between the perovskite and the HTM and consequently yield a stronger reductive quenching of the photoexcited state. THz

spectroscopy data, that observes transient photoconductivity corresponding to free and excitonic charges, support this hypothesis. Transient decay of mobile charges is observed on all perovskite samples, either on TiO_2 or Al_2O_3 framework. No major difference in the two layers is noticeable for samples that were not impregnated with HTM, as already observed in the visible transient absorption measurements. In the case of the HTM infiltrated samples, charge decay appears to be markedly slower on the Al_2O_3 samples. This reveals that mobile charges are separated mainly at the *spiro*-MeOTAD interface, while the remaining charges thus recombine more slowly. The difference in the observed dynamics for TiO_2 and Al_2O_3 samples is thus mainly attributed to inhomogeneity of prepared samples.

In the second part of this chapter, we were able to evidence the electron injection pathway and confirm the hole injection pathway. Using ultrafast spectroscopy in the near infrared, we were able to monitor transient absorption by photogenerated charges in the perovskite. Results showed that the decay of the charge population is delayed upon infiltration of the hole-transporting material *spiro*-MeOTAD, which is consistent with previous evidences of primary hole injection from the photoexcited perovskite into the HTM. Moreover, evidence for electron injection from $\text{CH}_3\text{NH}_3\text{PbI}_3$ into the TiO_2 film is presented. The latter process appears to lie in a similar timescale as the hole injection. Further evidences were brought by transient photoconductance measurements where slower charge decay in the presence of TiO_2 was monitored by transient photoconductance measurements in the microwave frequency range. Additionally, transient absorbance decay of oxidized *spiro*-MeOTAD was monitored in the near infrared. Experimental data showed that charge recombination with oxidized HTM species, which occurs in the microsecond timescale, is delayed on TiO_2 films with respect to Al_2O_3 , thus indicating that the mechanism involves recombination of charges separated by a longer distance. Observation of charge separation and charge recombination reactions is closely related to the morphology, and hence to the preparation method of the samples. Optical signals can be largely influenced by the presence of a capping layer of perovskite that is not conformally deposited on the mesoporous oxide film. Conformal coating of the TiO_2 surface by $\text{CH}_3\text{NH}_3\text{PbI}_3$ facilitates charge separation by ensuring direct electron injection into the oxide. These findings highlight the advantage of employing two heterojunctions with titanium dioxide and the HTM while using perovskite as a solid-state light absorber.

6.7 References

1. Kim, H.-S. *et al.* Lead iodide perovskite sensitized all-solid-state submicron thin film mesoscopic solar cell with efficiency exceeding 9%. *Sci Rep* 2, 591 (2012).
2. Marchioro, A. *et al.* Unravelling the mechanism of photoinduced charge transfer processes in lead iodide perovskite solar cells. *Nature Photon.* 8, 250–255 (2014).
3. Lee, M. M., Teuscher, J., Miyasaka, T., Murakami, T. N. & Snaith, H. J. Efficient hybrid solar cells based on meso-superstructured organometal halide perovskites. *Science* 338, 643–647 (2012).
4. Etgar, L. *et al.* Mesoscopic $\text{CH}_3\text{NH}_3\text{PbI}_3/\text{TiO}_2$ heterojunction solar cells. *J. Am. Chem. Soc.* 134, 17396–17399 (2012).
5. Liu, M., Johnston, M. B. & Snaith, H. J. Efficient planar heterojunction perovskite solar cells by vapour deposition. *Nature* 501, 395–398 (2013).
6. Burschka, J. *et al.* Sequential deposition as a route to high-performance perovskite-sensitized solar cells. *Nature* 499, 316–319 (2013).
7. Im, J.-H. H., Lee, C.-R., Lee, J.-W., Park, S.-W. & Park, N.-G. 6.5% efficient perovskite quantum-dot-sensitized solar cell. *Nanoscale* 3, 4088–4093 (2011).
8. Friedrich, D. & Kunst, M. Analysis of charge carrier kinetics in nanoporous systems by time resolved photoconductance measurements. *J. Phys. Chem. C* 115, 16657–16663 (2011).
9. Snaith, H. J. *et al.* Charge collection and pore filling in solid-state dye-sensitized solar cells. *Nanotechnology* 19, 424003 (2008).
10. Olson, C., Veldman, D., Bakker, K. & Lenzmann, F. Characterization of the pore filling of solid state dye sensitized solar cells with photoinduced absorption spectroscopy. *Int. J. Photoenergy* 2011, 1–11 (2011).
11. Rothenberger, G. & Fitzmaurice, D. Spectroscopy of conduction band electrons in transparent metal oxide semiconductor films: optical determination of the flatband potential of colloidal titanium dioxide films. *J. Phys. Chem.* (1992).
12. Xing, G. *et al.* Long-Range Balanced Electron- and Hole-Transport Lengths in Organic-Inorganic $\text{CH}_3\text{NH}_3\text{PbI}_3$. *Science* 342, 344–347 (2013).

CHAPTER 7

Conclusions and outlook

The work conducted in this thesis aimed at uncovering the mechanisms of charge transfer processes in solid-state solar cells based on hybrid organic-materials. Chapter 3 and 4 were devoted to solid-state dye-sensitized cells, with ruthenium-based sensitizer and the hole transport material *spiro*-MeOTAD. Chapter 5 and 6 were then focused on an organic-inorganic semiconductor, $\text{CH}_3\text{NH}_3\text{PbI}_3$, first considered only as light absorber but where recently the peculiar charge transporting properties have started to attract lot of attention. As these systems are based on the kinetic competition between charge separation and charge recombination, knowledge of the dynamics of heterogeneous charge transfer reactions at the surface of semiconductors is critical for the improvement of solar energy conversion devices. Experimental data obtained by time-resolved spectroscopic techniques proved to be powerful tools in order to give an insight on the parameters governing these charge transfer reactions.

Chapter 3 introduced the concept of hole injection in solid-state dye-sensitized solar cells. The main issues related with solid-state DSCs were discussed: hole mobility and pore filling appears to be the key factors influencing these devices, which still need further understanding in order to obtain better power conversion efficiencies. Time-resolved absorption spectroscopy allowed investigating the intricate kinetic processes that occur at the interfaces of such a system. Femtosecond transient absorption measurements with probe in the visible confirmed the multiexponential dynamics spanning from the picosecond to the nanosecond for the regeneration of the oxidized dye by the hole transport material *spiro*-MeOTAD already reported in the literature, thus indicating a large distribution of distances in the system. The optical signals in this region contain a mixture of the ground state bleaching and the oxidized *spiro*-MeOTAD, thus rendering more difficult the analysis of the dynamics. We showed herein that probing in the near-infrared gives access to the quenching of the oxidized state of the dye by the HTM *spiro*-MeOTAD, which is a direct information of the hole injection yield. Kinetic decay of the oxidized form of the sensitizer in the picosecond regime helped establishing a model for the morphology of the nanoporous structure filled with HTM. It was further shown that the pore filling fraction parameter is of crucial importance for the dynamics of hole injection in the first picoseconds after photoexcitation.

Chapter 4 focused on the effect of TiCl_4 treatment on both mechanisms of charge separation and charge recombination. Transient absorption spectra of electron injection, hole injection and charge recombination were recorded and a specific model was developed in order to treat the data obtained for hole injection from the oxidized dye to the HTM. This model allowed separating the contribution from the electrons, the oxidized HTM species and dye molecules that absorb in the same region of the spectrum. We showed that the kinetics of electron injection does not display a significant change upon TiCl_4 treatment, while hole injection is delayed. This was rationalized by a different penetration/wetting of the pores by the HTM when deposited out of solution, thus reducing the direct contact of dye and HTM. Interestingly, the largest effect of this surface treatment appears to be on charge recombination. This delayed charge recombination between electron injected in TiO_2 and oxidized *spiro*-MeOTAD can be explained by the same rationale as for the hole injection. These findings are in good agreement with previous studies showing that the effect of TiCl_4 treatment in liquid cells was mostly affecting charge recombination. Charge recombination in solid devices being a one-step

process, contrarily to recombination with liquid redox mediators based on iodide, it is likely to compete efficiently with the overall charge separation. Therefore this work underlines the importance of controlling charge recombination with the HTM in order to improve photovoltaic devices performance.

Future work should target a better controlling of the hole injection process through the monitoring of the pore wetting/filling. As it was shown, the amount of hole injection in the first picoseconds is crucially dependent on the pore filling fraction. Thus, a question that naturally arises is if the hole can be efficiently laterally transferred to the closest HTM molecule through lateral hole transfer. This process has been evidenced in liquid-based cells, and an interesting axis of research would then be to determine what is the minimal covering of the pore to still have efficient hole injection. This issue could be addressed through polarized transient absorption. Indeed, this polarization-sensitive technique would look at the oxidized state of the dye and how the initial polarized excitation would change orientation with time: this would be a direct measurement of the hole transfer between dyes, and subsequently their injection into *spiro*-MeOTAD.

In Chapter 5, we described the main spectral signatures obtained by femtosecond transient absorption spectroscopy of $\text{CH}_3\text{NH}_3\text{PbI}_3$ deposited on a mesoporous framework of Al_2O_3 . In this way, the only deactivation pathway possible is charge recombination within the perovskite itself, thus evidencing the photophysical processes in the material. The visible transient absorption spectrum of $\text{CH}_3\text{NH}_3\text{PbI}_3$ for two different wavelengths of excitation (510 and 580 nm) showed three main spectral components: a first negative signal peaking at 480 nm (blue band), which was attributed to the bleaching of the ground state species of the perovskite. A positive absorption signal between 630 and 700 nm was ascribed to the excited state absorption. Then, a negative peak starting after 700 nm (red band) on both samples was attributed mainly to stimulated emission. The effect of the fluence on the dynamics was presented and showed increasing recombination with increasing fluence in the first nanosecond. The recombination at longer timescales (> 1.5 ns) is then similar for all samples, showing fast delocalisation of the carriers. Global analysis performed on a $\text{CH}_3\text{NH}_3\text{PbI}_3$ sample provided additional insight in the origin of the spectral features observed. It was inferred that the stimulated emission in the 700 nm-region is a way to probe the thermalisation of hot states to the bottom of the conduction band, or to the top of the valence band. This thermalisation process occurs with a time constant of 0.35 ps, as shown by the partial recovery of the bleaching in the 480 nm-region and the increase of

the stimulated emission on the same timescale. A model for the photophysical processes in $\text{CH}_3\text{NH}_3\text{PbI}_3$ was proposed and differs from what can be found in the literature. This model, by analysis of two hypothetical situations, with in a first case two valence bands and one conduction band, and a second case with two conduction bands and one valence band, showed that neither case is adapted to describe the spectral signatures observed in the transient absorption spectra. Thus, we suggested a model with two valence bands and two conduction bands. This model could also reconcile the many different results found theoretically and experimentally in these last months.

Results presented in Chapter 6 unravelled the mechanisms of photoinduced processes in $\text{CH}_3\text{NH}_3\text{PbI}_3$ solid-state solar cells. Time-resolved techniques were applied to $\text{CH}_3\text{NH}_3\text{PbI}_3$ deposited as a conformal film on TiO_2 and Al_2O_3 samples to study the kinetics of interfacial electron transfer processes. Femtosecond transient absorption spectroscopy in the visible range applied to $\text{CH}_3\text{NH}_3\text{PbI}_3$ films on TiO_2 and Al_2O_3 photoanodes was not sufficient to unambiguously point out electron injection through comparison between TiO_2 and Al_2O_3 photoanodes. However, quenching of the luminescence for samples impregnated with HTM could be correlated with the efficiency of the charge separation, and revealed that hole injection process is happening on a very short timescale (< 150 fs). Similar results could be obtained by THz spectroscopy. The apparent weaker quenching of the $\text{CH}_3\text{NH}_3\text{PbI}_3$ excited state by the HTM in the TiO_2 sample compared to the Al_2O_3 -based layer might be rationalized by a different morphology obtained on the different oxides mesoporous films. In Al_2O_3 films, a better pore filling by the *spiro*-MeOTAD could offer a better contact between the perovskite and the HTM and consequently yield a stronger reductive quenching of the photoexcited state. In the second part of this chapter, we were able to evidence the electron injection pathway and confirm the hole injection pathway. Using ultrafast spectroscopy in the near infrared, we monitored transient absorption by photogenerated charges in the perovskite. Results showed that the decay of the charge population is delayed upon infiltration of *spiro*-MeOTAD, which is consistent with previous evidences of primary hole injection from the photoexcited perovskite into the HTM. Moreover, evidence for electron injection from $\text{CH}_3\text{NH}_3\text{PbI}_3$ into the TiO_2 film was presented. The latter process appears to lie in a similar timescale as the hole injection. Additionally, transient absorbance decay of oxidized *spiro*-MeOTAD was monitored in the near infrared. Experimental data showed

that charge recombination with oxidized HTM species, which occurs in the microsecond timescale, is delayed on TiO_2 films with respect to Al_2O_3 , thus indicating that the mechanism involves recombination of charges separated by a longer distance. Observation of charge separation and charge recombination reactions is closely related to the preparation method of the samples. Optical signals can be largely influenced by the presence of a capping layer of perovskite that is not conformally deposited on the mesoporous oxide film. Conformal coating of the TiO_2 surface by $\text{CH}_3\text{NH}_3\text{PbI}_3$ facilitates charge separation by ensuring direct electron injection into the oxide. These findings highlight for the first time the advantage of employing two heterojunctions with titanium dioxide and the HTM while using perovskite as a solid-state light absorber.

The perovskite adventure is now only at its beginnings. In a few years, we have been the witnesses of the spectacular evolution from a perovskite-based liquid cell, which was dissolving in a few minutes under illumination, to power conversion efficiencies higher than 17%. These sensational achievements must be complemented with fundamental studies in order to fully master all the potential this new material has to offer.

Indeed, many questions remain to be answered: the band structure of perovskite and the corresponding optical transitions are still not clear and might be varying according to the preparation procedure. Additionally, why are the chlorine impurities tremendously affecting the carriers' mobilities? Does this have an influence on the main spectroscopic signatures?

Is reductive quenching of the perovskite from the HTM a process susceptible to affect the electron injection step? Are the photogenerated charges free or is it possible to have exciton formation and diffusion to an interface? In other words, what would be the proportion of geminate to non-geminate recombination? The lifetime of electron-hole pairs and the formation of mobile charges are information that could be obtained by terahertz spectroscopy and complemented with time-resolved microwave photoconductivity. These techniques would also help to confirm the hypothesized double-band model. Additional knowledge on the spontaneous photoluminescence processes (as opposed to the stimulated processes) could be obtained by fluorescence up-conversion techniques.

Other questions that still remain unanswered concern the presence of ionic additives. What is the effect of the additives commonly added to the hole-transporting matrix, such

as lithium salts and *tert*-butylpyridine? Nanosecond transient absorption is useful to access the lifetime of oxidized *spiro*-MeOTAD and then determine the conditions in which the back recombination is the most delayed. Femtosecond transient absorption could determine if the hole injection into the HTM or electron injection into the TiO₂ is hindered or facilitated in presence of these additives.

Nonetheless, it has to be borne in mind that the role of these additives in the crystalline matrix of perovskite can be much more complex than in molecular systems based on dyes. Ionic additives are susceptible to engender substitution in the perovskite lattice and thus change both its optical and electronic properties.

Furthermore, the involvement of charge transfer states, where charges separated at an interface, but still coulombically correlated would be a hypothesis to consider: in this case, an electron in TiO₂ correlated with a hole in the perovskite or alternatively, an electron in the perovskite correlated with a hole in the *spiro*-MeOTAD. The extent of this correlation would be dependent on the respective dielectric constants and here, the presence of ionic additives should further play a major role. As an example, femtosecond transient absorption monitoring the oxidized state of *spiro*-MeOTAD, complemented by terahertz spectroscopy to follow mobile charges in the perovskite would give an insight on a hypothetical charge transfer state.

The research pathways opened by the application of this incredible material in solar energy conversion devices are numerous, and many of these questions can be addressed by combining various types of time-resolved spectroscopic techniques, to access excited states absorption as well as carriers' mobilities.

Acknowledgments

I would like to express all my gratitude to Prof. Jacques Moser, for his constant support during these four years, for the scientific discussions as well as life discussions, and for giving me the opportunity to pursue experiments my way and learn from my mistakes. And especially for bringing back my faith in science the days when nothing was working. I would like to thank my thesis co-advisor Prof. Michael Grätzel for giving me the opportunity to work in such a stimulating environment.

A special thanks goes to all the past and present members of the GR-MO. In particular, Joël, for introducing me to the secrets of transient absorption during my master, and for all the animated-Friday-afternoon discussions about science, even if we wanted to kill each other most of the time. Angela, for teaching me the delicate art of NOPA alignment (*yes, a Gaussian pulse can always be more Gaussian, try again!*) and all the secrets of the femtocave. Jan for his legendary patience and help with any kind of technical problem inside a laser cavity. Natalie for Matlab, technical issues and life discussions. And in particular, Jelissa for sharing the office during four long years, support with the hard moments in the lab and mutual encouragement (keeping the lab clean with Monica), conferences together and simply everything in this PhD life. Andrius, for helping me to see the light of the TOPAS even in the darker moments of the femtocave. Andrea, who had the difficult task of being the first master student, and Adrian, for listening to all my security advises on PbI₂.

From LPI, I would like to thank Dr. Zakeeruddin for dyes and Pascal Comte for TiO₂ and Al₂O₃ pastes. A special thank to Dr. Pierre Infelta for unforgettable thermodynamical moments and help with tedious mathematical models. Dr. Thomas Moehl and Dr. Robin Humphry-Baker for stimulating scientific discussions (Robin also for challenging me to ski on the hardest slopes of Verbier). Everybody from mechanical workshop for their help when I was desperately looking for that lost imperial screw, and the electronic workshop for reducing my ignorance on diodes, resistances, and earth issues. Fred for all the time he spent helping us with Labview, Yoann for helping me with computer problems and PAP

for being the best office neighbor ever. Madeleine, Heidi and Carmen for dealing with all my administrative issues.

And all the other former and actual LPI members for good times and good discussions, for coffee breaks, ski days, snowshoes, sauna and chalet sessions, floating down the Aare river with inflatable crocodiles, runs in Lisboa and much more: Adriana, Amalie, David, Fab, Hauke, Jérémy, Jean-David, Kevin, Leo, Luzi, Matt, Marcel, Maurin, Nic, Phil. Florian for his presence, 24-hour emergency support on Igor, as well as for all the scientific (or not) debates we always have.

To end, I would like to thank all my old times friends, who understood and accepted my hermit working-mode and brought me back to reality when I needed. Un ringraziamento speciale va alla mia famiglia, a mia madre e a mia sorella per il sostegno costante e la pazienza durante il periodo della redazione, e a mio padre, per avermi infuso la curiosità scientifica, e per la rilettura attenta del manoscritto.

Curriculum Vitae

Arianna Marchioro

Date of birth: April 10, 1986

Nationality: Italian

Languages:

French and Italian (native)

English (fluent)

Education

- 05/2010 – **PhD Thesis in Photonics**
05/2014
Group of Photochemical Dynamics and Laboratory of Photonics and Interfaces, EPFL, Lausanne, Switzerland
Thesis title: Interfacial charge transfer dynamics in solid-state hybrid organic-inorganic solar cells
Director and co-director: Prof. J.-E. Moser and Prof. M. Grätzel
- 09/2008 – **Master of Science in Molecular and Biological Chemistry**
02/2010
EPFL, Lausanne, Switzerland
Imperial College, London, UK (6 months exchange program)
- 09/2005 – **Bachelor of Science in Chemistry**
07/2008
EPFL, Lausanne, Switzerland

Work experience & research projects

- 09/2010 – **Teaching Assistant at EPFL**
02/2014
 - Assistant for thermodynamic classes (2nd year bachelor students)
 - Supervision of 2 master's projects (2 days/week for 6 months)
 - Supervision of 2 students during their master's thesis (6 months)
- 09/2009 – **Master's Thesis at Imperial College, London**
02/2010
Synthesis and characterization of organometallic complexes interacting with quadruplex DNA
Supervisors: Prof. R. Vilar and Prof. P. Dyson
- 07/2008 – **Internship at CERN, Geneva**
10/2008
FTIR study of magnetron-sputtered carbon coatings for accelerator beam-pipe

Awards & Honors

- 2010 *BASF Monthey* prize: best master's thesis in Molecular and Biological Chemistry
- 2009 *Syngenta Monthey* prize: best master student in Molecular and Biological Chemistry
- 2008 *Louis Pelet* prize: best bachelor student in Chemistry

List of scientific publications

Main research work

- Marchioro, A., Teuscher, J., Friederich, D., Kunst, M., van de Krol, R., Moehl T., Grätzel, M., Moser, J.-E.

Unraveling the mechanism of photoinduced charge transfer processes in lead iodide perovskite solar cells

Nature Photonics, 8, 250-255, doi:10.1038/nphoton.2013.374, (2014).

- Marchioro, A., Brauer, J.C., Teuscher, J., Grätzel, M., Moser, J.-E.

Photoinduced processes in lead iodide perovskite solid-state solar cells

Proceedings of SPIE, 8811, art. no. 881108, (2013).

- Marchioro, A., Dualeh, A., Punzi, A., Grätzel, M., Moser, J.-E.

Effect of posttreatment of titania mesoscopic films by TiCl₄ in solid-state dye-sensitized solar cells: A time-resolved spectroscopy study

J. Phys. Chem. C, 116 (51), 26721–26727 (2012).

- Kim, H.-S., Lee, C.-R., Im, J.-H., Lee, K.-B., Moehl, T., Marchioro, A., Moon, S.-J., Humphry-Baker, R., Yum, J.-H., Moser, J.E., Grätzel, M., Park, N.-G.

Lead iodide perovskite sensitized all-solid-state submicron thin film mesoscopic solar cell with efficiency exceeding 9%

Sci. Rep. 2, 591; DOI:10.1038/srep00591 (2012).

Additional Research Projects

- Teuscher, J., Marchioro, A., Andrès, J., Roch, L., Xu, M., Zakeeruddin, S.M., Wang, P., Grätzel, M., Moser, J.-E.

Kinetics of the Regeneration by Iodide of Dye-Sensitizers Adsorbed on Mesoporous Titania

J. Phys. Chem. C, doi: 10.1021/jp501481c, (2014).

- Yum, J.-H., Baranoff, E., Kessler, F., Moehl, T., Ahmad, S., Bessho, T., Marchioro, A., Ghadiri, E., Moser, J.-E., Yi, C., Nazeeruddin, M.K., Grätzel, M.

A cobalt complex redox shuttle for dye-sensitized solar cells with high open-circuit potentials

Nat. Commun. 3:631 doi: 10.1038/ncomms1655 (2012).

- Bauer, C., Teuscher, J., Brauer, J.C., Punzi, A., Marchioro, A., Ghadiri, E., De Jonghe, J., Wielopolski, M., Banerji, N., Moser, J.-E.

Dynamics and mechanisms of interfacial photoinduced electron transfer processes of third generation photovoltaics and photocatalysis

Chimia, 65 (9), 704–709 (2011).

- Sauvage, F., Chhor, S., Marchioro, A., Moser, J.-E., Grätzel, M.

Butyronitrile-based electrolyte for dye-sensitized solar cells

J. Am. Chem. Soc., 133 (33), 13103–13109 (2011).

- Melas-Kyriazi, J., Ding, I.-K., Marchioro, A., Punzi, A., Hardin, B.E., Burkhard, G.F., Tétreault, N., Grätzel, M., Moser, J.-E., McGehee, M.D.

The effect of hole transport material pore filling on photovoltaic performance in solid-state dye-sensitized solar cells

Adv. Energy Mater. 1 (3), 407–414 (2011).

- Punzi, A., Brauer, J.C., Marchioro, A., Ghadiri, E., De Jonghe, J., Moser, J.-E.

Photoinduced interfacial electron transfer and lateral charge transport in molecular donor-acceptor photovoltaic systems

Chimia, 65 (5), pp. 353-355 (2011).

Conferences and Workshops

Oral presentations

- August 2013: SPIE Optics + Photonics 2013, San Diego, **USA**

Title: *Photoinduced processes in $CH_3NH_3PbI_3$ solid-state solar cells*

- June 2013: NanoGe QuantumDot, Granada, **Spain**

Title: *Photoinduced processes in $CH_3NH_3PbI_3$ sensitized solar cells*

Poster presentations

- NanoGe HOPV, **Spain**, 2011, **Sweden**, 2012 & **Switzerland**, 2014
- Swiss Chemical Society meetings, **Switzerland**, 2010, 2011, 2012
- Swiss Physical Society meeting, **Switzerland**, 2012
- NCCR MUST meetings, **Switzerland**, 2011, 2012, 2013
- EPFL Photonics Day, **Switzerland**, 2010, 2011, 2012, 2013

Summer school and others

- Organic and Dye Based Photovoltaics, Jyväskylä, **Finland**, 2011
- Nanoelectrochemistry, Villars, **Switzerland**, 2010
- Winter La+b interdisciplinary workshop, Lugano, **Switzerland**, 2013

Scientific society membership

- Member of the Swiss Chemical Society